UNIVERSITY OF CALIFORNIA

Santa Barbara

Molecular Beam Epitaxy of Perovskite BaSnO$_3$ and Antiperovskite Sr$_3$SnO Thin Films

A Dissertation submitted in partial satisfaction

of the requirements for the degree of

Doctor of Philosophy

in

Materials

By

Wangzhou Wu

Committee in Charge:

Professor Susanne Stemmer, Chair

Professor Umesh Mishra

Professor James Speck

Professor Stephen Wilson

March 2023

The Dissertation of

Wangzhou Wu is approved:

_____

Umesh Mishra

_____

Stephen Wilson

_____

James Speck

_____

Susanne Stemmer, Chair

December 2022

Molecular Beam Epitaxy of Perovskite BaSnO$_3$ and Antiperovskite Sr$_3$SnO Thin Films

Acknowledgments

Jeong, David Kealhofer, Honggyu Kim, Yuntian Li, Patrick Marshall, Tyler Pardue, Salva Salmani Rezaie, Billy Strickland, Omor Shoron, and Timo Schumann. I especially thank Patrick Marshall who brought me into the research world and guided me all the time in my PhD career even after his graduation. I also appreciate Nick Combs, Robert Kealhofer, and Alex Lygo a lot for their help in the proof check of this thesis.

The success of the MBE lab at UCSB would never be achieved without the technical support from the engineers, Kurt Olsson, and John English, who look after the lab so well. Therefore, I would express my deep gratitude to them. Their input to make sure the best shape of the MBE machines is invaluable and research without their support is impossible to come true.

As is said, two things remain irretrievable, time and a first impression. My first impression of MBE was introduced by Prof. Bharat Jalan in his lectures at the University of Minnesota. He managed to describe MBE so interestingly that I was convinced to start a PhD career involving MBE. He then introduced me to Prof. Stemmer who gave me the opportunity for this goal. For that, I am always grateful.

Finally, and importantly, I'd like to say the long-lost "thank you" to my parents. All your unconditional love will forever be appreciated and remembered. I would also like to express my gratitude to all my friends who brought joy and happiness into my life.

Curriculum Vitae

Wangzhou Wu

EDUCATION

Ph.D. in Materials, *University of California, Santa Barbara* December 2022

Master of Science in Materials, *University of California, Santa Barbara* September 2020

Bachelor of Materials Science and Engineering, *University of Minnesota, Twin Cities* June 2017

Bachelor of Polymer Science and Engineering, *Sichuan University, Chengdu* June 2017

PROFESSIONAL APPOINTMENTS

Graduate Student Researcher, *University of California, Santa Barbara* 2017-2022

Teaching Assistant, *University of California, Santa Barbara* 2018-2019

Undergraduate Student Researcher, *University of Minnesota, Twin Cities* 2015-2017

PUBLICATIONS

1. **Wangzhou Wu**, Nicholas G. Combs, and Susanne Stemmer. "Revealing the intrinsic transport properties of antiperovskite Sr_3SnO thin films", *Appl. Phys. Lett.* **121**, 233101 (2022).

2. **Wangzhou Wu**, Nicholas G. Combs, and Susanne Stemmer. "Molecular beam epitaxy of phase-pure antiperovskite Sr_3SnO thin films", *Appl. Phys. Lett.* **119**, 161903 (2021).

3. **Wangzhou Wu**, Nicholas G. Combs, Thomas E. Mates, and Susanne Stemmer. "Carbon impurity concentrations in $BaSnO_3$ films grown by molecular beam epitaxy using a tin oxide source", *Journal of Vacuum Science & Technology A* **38**, 043405 (2020).

4. Junao Cheng, Hao Yang, Nicholas G Combs, **Wangzhou Wu**, Honggyu Kim, Hareesh Chandrasekar, Caiyu Wang, Siddharth Rajan, Susanne Stemmer, Wu Lu. "Electron transport of perovskite oxide $BaSnO_3$ on (110) $DyScO_3$ substrate with channel-recess for ferroelectric field effect transistors", *Appl. Phys. Lett.* **118**, 042105 (2021).

5. Nicholas G. Combs, **Wangzhou Wu**, and Susanne Stemmer. "Stoichiometry control in molecular beam epitaxy of $BaSnO_3$", *Phys. Rev. Materials* **4**, 014604 (2020).

6. Junao Cheng, Hao Yang, Caiyu Wang, Nick Combs, Chris Freeze, Omor Shoron, **Wangzhou Wu**, Nidhin Kurian Kalarickal, Hareesh Chandrasekar, Susanne Stemmer, Siddharth Rajan, Wu Lu. "Nanoscale etching of perovskite oxides for field effect transistor applications", *Journal of Vacuum Science & Technology B* **38**, 012201 (2020).

7. Kaveh Ahadi, Luca Galletti, Yuntian Li, Salva Salmani-Rezaie, **Wangzhou Wu**, Susanne Stemmer. "Enhancing superconductivity in $SrTiO_3$ films with strain", *Sci. Adv.* **5**, eaaw0120 (2019).

8. Jong Seok Jeong, **Wangzhou Wu**, Mehmet Topsakal, Guichuan Yu, Takao Sasagawa, Martin Greven, K Andre Mkhoyan. "Decomposition of $La_{2-x}Sr_xCuO_4$ into several La_2O_3 phases at elevated temperatures in ultrahigh vacuum inside a transmission electron microscope", *Phys. Rev. Materials* **2**, 054801 (2018).

Abstract

Molecular Beam Epitaxy of Perovskite BaSnO₃ and Antiperovskite Sr₃SnO Thin Films

By Wangzhou Wu

This thesis aims to explore and understand the structural and electrical properties of the antiperovskite Sr_3SnO and the perovskite $BaSnO_3$. Despite both being stannates, their properties are very different. Highly Sr-deficient $Sr_{3-x}SnO$ has been proposed as a possible topological superconductor because of its band structure is theoretically predicted to be topologically non-trivial, and a superconducting transition in bulk $Sr_{3-x}SnO$ ($x \sim 0.5$) polycrystalline ceramics is experimentally observed at ~ 4 K. In contrast, $BaSnO_3$ is not topological, but it is a candidate as a next-generation transparent conducting oxide and wide band-gap semiconductor for power electronics. Bulk $BaSnO_3$ crystals are reported to have room temperature mobilities above 300 $cm^2V^{-1}s^{-1}$.

The challenges in the research of Sr_3SnO and $BaSnO_3$ are also different. To date, the superconductivity in Sr_3SnO has only been observed in highly Sr-deficient bulk polycrystalline ceramics containing secondary phases. The impurity phases make the study of the intrinsic properties of Sr_3SnO difficult. Most importantly, the roles of these phases in the origin of superconductivity are poorly understood. Molecular beam epitaxy (MBE) of Sr_3SnO films has been reported, but phase purity is not assured. As for $BaSnO_3$, high-quality thin films are desired because they can be epitaxially integrated with various other perovskites to make advanced devices. Different MBE methods to grow $BaSnO_3$ thin films have been developed. Still, the highest room-temperature carrier mobility values in films are between 150 to 180

cm^{2}V^{-1}s^{-1}, well below the value observed in bulk crystals. Prior to the work discussed in this thesis, the upper limit of the carrier mobility inside BaSnO$_3$ films was mainly attributed to threading dislocations.

In this work, oxide MBE is demonstrated to be capable of growing phase-pure Sr$_3$SnO thin films. Exploration within the phase-pure growth window achieved a film with a hole mobility of 400 cm^{2}V^{-1}s^{-1} (highest in literature) and carrier density of 3.7×10^{18} cm^{-3} (lowest in literature) at 10 K. However, none of the phase-pure films were superconductive, raising questions as to whether the hole carrier density was high enough given that the superconductive bulk Sr$_{3-x}$SnO polycrystalline ceramics have carrier densities above 10^{21} cm^{-3}. This motivated research using indium as a dopant to increase the hole carrier density. It was found that the hole carrier density could be precisely tuned by varying the indium source temperature. Unfortunately, even a film with a hole carrier density above 10^{21} cm^{-3} was still not superconductive. Therefore, the superconductivity observed in bulk Sr$_{3-x}$SnO polycrystalline ceramics is possibly extrinsic.

The same oxide MBE system was used to grow BaSnO$_3$ thin films. Lattice-matched substrates were used to reduce the threading dislocations inside the BaSnO$_3$ films. However, this reduction did not improve carrier mobility, indicating that other defects may play important roles. Therefore, point defects were investigated as the potential mobility limiting defect. Carbon concentrations in BaSnO$_3$ films were measured using secondary ion mass spectroscopy. The result showed a mid-to-low 10^{18} atoms/cm^3 carbon density. The origin of the carbon was found to be the SnO$_2$ source material and associated with surface adsorbents. In addition, an analysis of the growth rate, x-ray diffraction patterns, and lattice constant indicates that Sn-rich and O-poor growth conditions were present during all the growths. The

excess Sn ions were accommodated into the Ba sites to form Sn_{Ba} antisite defects. Both point defects may pose an upper limit to thin film mobility.

Table of Contents

List of Figures

Chapter 1 Introduction to perovskite and antiperovskite oxides

This thesis will discuss the molecular beam epitaxy, characterization, and electrical properties of $BaSnO_3$ perovskite and Sr_3SnO antiperovskite thin films. This chapter serves as a background introduction and motivation for the work in this thesis. In section 1.1, I will first give an overview of the properties of ABO_3 perovskite oxides and then $BaSnO_3$, followed by the recent progress in the materials synthesis of $BaSnO_3$. Motivations and the accompanying challenges of growing high-quality $BaSnO_3$ thin films are further discussed. In section 1.2, I will discuss the previous $BaSnO_3$ growth and characterization work done by Santosh Raghavan, Timo Schumann, Omor Shoron, Chris Freeze, Nick Combs, and Honggyu Kim here at UCSB, on which my work is based. Section 1.3 will discuss A_3BO antiperovskite oxides and Sr_3SnO using the same logic as section 1.1.

Figures 1-1 and 1-2 in this chapter are reprinted from APL Mater. **4**, 016106 (2016), with the permission of AIP Publishing. The license number is 5406200779503. Figure 1-3 is reprinted from Phys. Rev. Mater. **4**, 014604 (2020), with copyright (2020) by the American Physical Society. Figure 1-5 is reprinted from Phys. Rev. B. **104**, 045411 (2021), with copyright (2021) by the American Physical Society. The license number is RNP/22/OCT/058841. Figure 1-6 (a) is reprinted from Nat. Commun. **7**, 13617 (2016). Figure 1-6 (b) is reprinted from Sci. Rep. **9**, 1831 (2019). The license link for Figure 1-6 is https://creativecommons.org/licenses/by/4.0/. Full reference citations are provided in this thesis's bibliography, and the citation numbers are marked under the Figures' caption.

1.1 ABO_3 perovskite oxides and $BaSnO_3$

The perovskite oxide family (chemical formula ABO_3, where A and B can be a variety of metal cations) has continuously attracted attention because the members contain an extensive range of materials properties. All three common electronic states, metals, insulators,

and semiconductors, have been observed in the perovskite family. There are also rich physics and engineering opportunities in these materials. For example, $SrTiO_3$ is found to have ferroelectricity and superconductivity [1-4], and $BaSnO_3$ has been considered as a great candidate as a next-generation transparent conducting oxide [5-11]. The differences in properties of the perovskite family members are associated with different combinations of A and B cations, despite the perovskites all sharing the same general crystal structure.

$BaSnO_3$ has recently gained attention because of its property as a transparent conducting oxide. $BaSnO_3$ has a direct band gap of 3.36 eV, and a smaller indirect gap of 3.1 eV [12]. The values of the band gaps make $BaSnO_3$ transparent. The conduction band of $BaSnO_3$ is mainly determined by the Sn 5s orbital that has a high dispersion [13]. This leads to a relatively low effective mass experimentally measured to be 0.19 ± 0.01 in films [14]. Dopants, such as La, can sit on the Ba site, fill the conduction band minimum with electrons, and make $BaSnO_3$ conductive. It has been reported that $BaSnO_3$ single crystals can have carrier mobilities above 300 $cm^2V^{-1}s^{-1}$ with carrier densities around 10^{20} cm^{-3} at room temperature [5,6]. The mobility of $BaSnO_3$ single crystals surpasses that of the most well-known transparent conducting oxide, indium-doped tin oxide, whose room temperature mobility is only slightly above 100 $cm^2V^{-1}s^{-1}$ [15-19]. Therefore, $BaSnO_3$ has been heavily discussed for its potential to be a novel transparent conducting oxide. [5-11].

Extensive efforts have also been made to replicate the excellent performance of $BaSnO_3$ single crystals in thin films, which can allow for epitaxial integration with other perovskite oxides [20-24]. Molecular beam epitaxy (MBE) of $BaSnO_3$ thin films using SnO_2 as the source material for Sn and ozone for oxidant has achieved the highest mobility values up to 180 $cm^2V^{-1}s^{-1}$ [24]. Previous work at UCSB (see section 1.2) can achieve comparable

3

mobilities up to 170 $cm^2V^{-1}s^{-1}$ by using SnO_2 and oxygen plasma [25]. Both values are still well below 300 $cm^2V^{-1}s^{-1}$. Therefore, exploring the mobility-limiting factors is critical for further improvement of $BaSnO_3$ thin film performance.

The most prominent defects that exist in $BaSnO_3$ thin films are threading dislocations caused by the strain-relaxation process during thin film growth. The fundamental reason is the large lattice mismatch between $BaSnO_3$ and most commercially available perovskite substrates. For example, $SrTiO_3$ has a lattice mismatch of about 5.1% with $BaSnO_3$, and that of $DyScO_3$ is about 4.2%. The large mismatch makes the critical thickness of $BaSnO_3$ only a few nanometers, after which the films start to relax by introducing misfit dislocations that can further extend to threading dislocations. Threading dislocations can serve as a scattering source for electronic carriers.

Threading dislocations are, however, not likely to be the only scattering source. When the lattice mismatch is below a certain level, it has been seen that the mobility does not significantly increase with the reduction of lattice mismatch [24,25]. Moreover, the work here at UCSB has seen a significant difference in the mobility by varying stoichiometry. This indicates that there are possibly point defects capping the upper limit of mobility in $BaSnO_3$ thin films. However, the study of point defects in $BaSnO_3$ is minimal because the focus has been mainly on the threading dislocations.

The work of $BaSnO_3$ in this thesis begins by validating the hypothesis that the mobility is limited by defects other than threading dislocations by growing $BaSnO_3$ on lattice-matched substrates (Chapter 5). The results show that despite the elimination of threading dislocations, the mobilities of the $BaSnO_3$ thin films is not improved substantially. Therefore, exploration of point defects (Chapter 6) follows, where secondary-ion mass spectrometry (SIMS) finds a

high carbon impurity concentration in the $BaSnO_3$ films. Another study based on varying the growth conditions and analyzing the lattice constant of $BaSnO_3$ thin films sheds light on the defects on the Ba sites.

1.2 Previous work on BaSnO₃ at UCSB [25]

Previous work on $BaSnO_3$ at UCSB starting in 2016 was built on the background that the carrier mobility of La-doped $BaSnO_3$ thin films grown using the traditional source materials (elemental Sr, Sn, La, and oxygen plasma) could not exceed $100 \text{ cm}^2\text{V}^{-1}\text{s}^{-1}$ [20-24]. The reason was that oxygen plasma was not active enough to fully oxidize the evaporated Sn. Likely, most Sn was only partially oxidized into SnO, which may substantially desorb from the substrate due to its high volatility. An experimental evidence was that Sn was not incorporated at all when the substrate temperature was higher than 600 ℃.

To solve this problem, SnO_2 powder was used as a new source material where the Sn was pre-oxidized. It has been reported that the flux from heating SnO_2 source is mainly a mixture of SnO and O_2 [26-29]. Moreover, this method allowed for the adoption of substrate temperatures higher than 800 ℃ and therefore achieved high ad-atom mobility to ensure high structural quality. Details of the MBE growth method of $BaSnO_3$ will be introduced in Chapter 2.

Figure 1-1 shows the *x*-ray diffraction (XRD) and transmission electron microscopy (TEM) data for $BaSnO_3$ films grown using the SnO_2 powder source. The $BaSnO_3$ film grown on (110) $PrScO_3$ substrate has a thickness of 32 nm. The $2\theta\text{-}\omega$ scan of the film is shown in Figure 1-1 (a), with the presence of Laue fringes indicating a high-quality interface and surface. Figure 1-1 (b) is the reciprocal space map of the region near the 103 $BaSnO_3$ peak along with

the 332 $PrScO_3$ peak. The difference in the in-plane lattice parameters indicates that the $BaSnO_3$ film is not fully strained. This is expected because the lattice mismatch between $BaSnO_3$ film and $PrScO_3$ substrate is about 2.18%. Due to the lattice mismatch, misfit dislocations are seen in the high-angle annular dark-field scanning TEM and the diffraction contrast dark-field TEM images (Figure 1-1 (c) and (d), respectively) at the $BaSnO_3$/substrate interface. Figure 1-1 (c) shows a Burgers circuit near a misfit dislocation at the $BaSnO_3$/$SrTiO_3$ interface, identifying the Burgers vector as a[100]. The periodic spacing between these misfit dislocations is about 8 nm at the $BaSnO_3$/$SrTiO_3$ interface, and between 20 and 30 nm at $BaSnO_3$/$PrScO_3$ interface, as seen in Figure 1-1 (d).

Figure 1-2 (a) compares the carrier mobility (measured by the Van der Pauw method) of the La-doped $BaSnO_3$ films grown on $SrTiO_3$ and $PrScO_3$ substrates in this previous work with the other literature reported values before 2016. The main result is that by replacing the elemental Sn source with SnO_2, the transport property of La-doped $BaSnO_3$ films is significantly improved.

To date, using the same method as in this previous work, the highest mobility we can achieve is 170 $cm^2V^{-1}s^{-1}$. The highest mobility value reported in the literature is 180 $cm^2V^{-1}s^{-1}$ [24]. These two values are statistically the same because the measurement error in Hall mobility [30] and film nonuniformity is more significant than a few 10's of $cm^2V^{-1}s^{-1}$ difference in mobility between different films. This can be seen in Figure 1-3, which shows that the fabricated Hall bar structures on different regions of the same sample have a variation of Hall mobility on the order of 10's of $cm^2V^{-1}s^{-1}$ [31].

Figure 1-2 (b) shows the temperature dependence of the carrier density and sheet resistance of the $BaSnO_3$ films. No carrier freeze-out is observed, indicating charge trapping

is of a minor extent at these very high carrier densities. Metallic behavior is seen in the films, which is expected in degenerately doped semiconductors. Figure 1-2 (c) shows the carrier mobility in the temperature range between 300 and 4 K. The mobility starts to saturate below 100 K as the mobility becomes limited by disorder which is not temperature dependent. Therefore, the low-temperature mobility reflects the level of defects inside the material. As is seen, the low-temperature mobility for the $BaSnO_3$ film grown on $PrScO_3$ substrate is about 300 $cm^2V^{-1}s^{-1}$, almost twice the mobility for the film grown on $SrTiO_3$ substrate. This indicates that the defects introduced by the large lattice mismatch ($> 2.18\%$) limit the transport in $BaSnO_3$ films. The defect is likely to be the threading dislocations extending from the misfit dislocations all the way to the sample surface, as seen in Figure 1-4.

In summary, this previous work points out that threading dislocations can limit carrier mobility when the lattice mismatch is larger than 2.18%. This, however, does not conclude that threading dislocations are the only scattering source. Therefore, it motivates the study of growing $BaSnO_3$ on lattice-matched substrates (Chapter 5). The result in Chapter 5 shows that eliminating threading dislocations does not further improve the transport, indicating that other defects are capping the upper limit of mobility. This result further motivates the study of point defects in $BaSnO_3$ films (Chapter 6).

1.3 A_3BO antiperovskite oxides and Sr_3SnO

Antiperovskite oxides, A_3BO, are compounds where A cations of the perovskite structure are replaced by oxygen ions and vice versa. The B ion takes a formal 4- valence state to keep charge neutrality, which is unusual for a metal element. This structural and electronic configuration has been predicated on being a cradle for topological band structures. Therefore, a significant number of experimental studies have been performed to explore the existence of

Dirac fermions in antiperovskite oxides [32-50]. Sr_3SnO, for example, is predicted to be a topological crystalline insulator in which superconductivity and topological transport behaviors have been experimentally observed [43-46, 49, 50].

The discovery of Sr_3SnO was due to an accident intended to synthesize Sr_3Sn alloy [51]. The result showed that the combination of Sr and Sn with a stoichiometric ratio of 3:1 could only be stable by incorporating oxygen, forming an antiperovskite Sr_3SnO structure [51]. The space group of Sr_3SnO is the same as the cubic perovskite ($Pm\bar{3}m$), but the lattice constant of Sr_3SnO (5.16 Å) [52] is larger than most of the perovskite materials due to the exchange of positions between Sr cations and oxygen ions.

A feature of Sr_3SnO is that the outer-shell electrons of the Sr atom are almost entirely transferred to the more electronegative Sn atom, making Sn take a formal 4- valence state. Such an electronic configuration makes Sr_3SnO a topological crystalline insulator that hosts gapped Dirac nodes in the band structure (Figure 1-5). As is shown, a gapped Dirac node resides along the Γ-X direction with a very narrow band gap of about 10 meV [53]. In three dimensions, due to the cubic symmetry of the material, there are six equivalent Dirac nodes along the six Γ-X directions. Moreover, $Sr_{3-x}SnO$ (x~0.5) is the first reported superconducting antiperovskite oxide with a transition temperature around 5 K (Figure 1-6 (a)), making it a candidate for an intrinsic topological superconductor [43-45].

Despite the progress in theory and experiment, understanding of the intrinsic properties of Sr_3SnO is still poor. This is mainly because of the creation of impurity phases when the stoichiometry is deliberately changed to create Sr vacancies which provide holes as the carriers in Sr_3SnO. For those superconductive $Sr_{3-x}SnO$ polycrystalline ceramics, approximately 10% of the Sr site is vacant such that the density of holes is above 10^{21} cm^{-3} [43-45]. The impurities

can be SrO, Sn, a variety of Sr-Sn alloys, and hydroxides (see Figure 1-6 (b) for XRD). The effects of the impurity phases on the properties of $Sr_{3-x}SnO$ are barely understood.

Recent studies on the MBE growth of Sr_3SnO thin films show clean XRD with no impurity peaks. However, XRD alone is insufficient to ascertain the phase purity since impurity peaks can hide if the phases are poorly crystallized, randomly oriented, or present in small quantities. Therefore, supplementary characterization methods, such as electron microscopy, are needed to ensure the phase purity. Nevertheless, this is not easy due to the extreme air sensitivity of Sr_3SnO.

This background of Sr_3SnO research motivates the work in this thesis. In Chapter 2, I will introduce the methodologies that overcome the air-sensitivity issue in the structural characterizations and electrical measurements of Sr_3SnO. With these tools, Chapter 3 shows that phase pure Sr_3SnO can be achieved by MBE, followed by a discussion on the structural data and intrinsic transport properties. It is found that the film closest to being stoichiometric can have a carrier density as low as 4×10^{18} cm^{-3}. Chapter 4 introduces a carrier density tuning method by using indium as a dopant to provide holes above 10^{21} cm^{-3}, in which magnitude the $Sr_{3-x}SnO$ polycrystalline ceramics are found to be superconductive. This method avoids the deliberate change in the stoichiometry to introduce more carriers and therefore steers clear of impurity phases. The In-doped Sr_3SnO film with carrier density higher than 10^{21} cm^{-3} is, unfortunately, not superconducting. An effect of the dopant on the temperature dependence of sheet resistance is discussed in section 4.3.
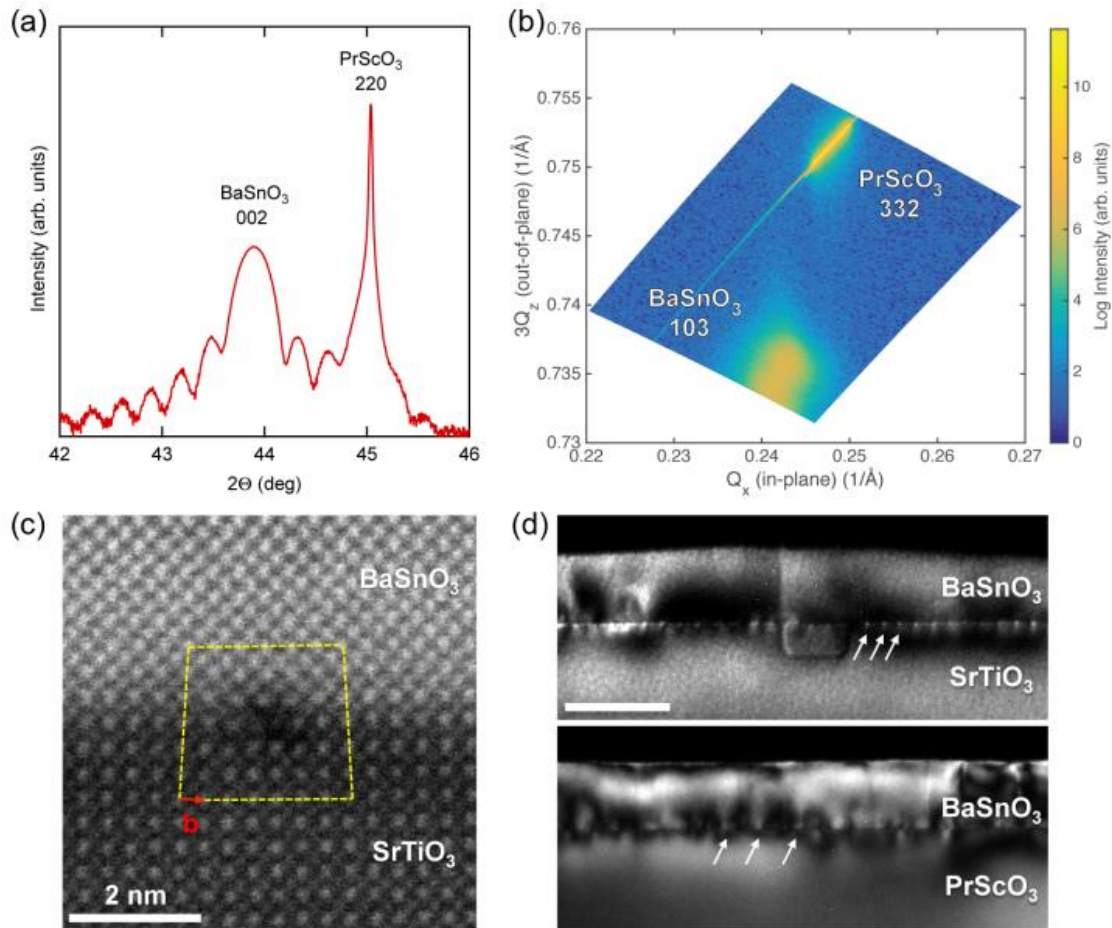
Figure 1-1: (a) XRD 2θ-ω scan around the 002 BaSnO$_3$ reflection. (b) Reciprocal space map near the 103 BaSnO$_3$ reflection for a 32 nm BaSnO$_3$ film on (110) PrScO$_3$. (c) HAADF-STEM image of a BaSnO$_3$/SrTiO$_3$ heterostructure. The Burgers circuit (yellow circle) identifies a misfit dislocation with a Burgers vector a[100]. (d) Cross section dark-field TEM images of BaSnO$_3$ on SrTiO$_3$ and PrScO$_3$ substrates. The white arrows identify periodic misfit dislocations. The figure is reprinted from [25] with the permission of AIP publishing.

10
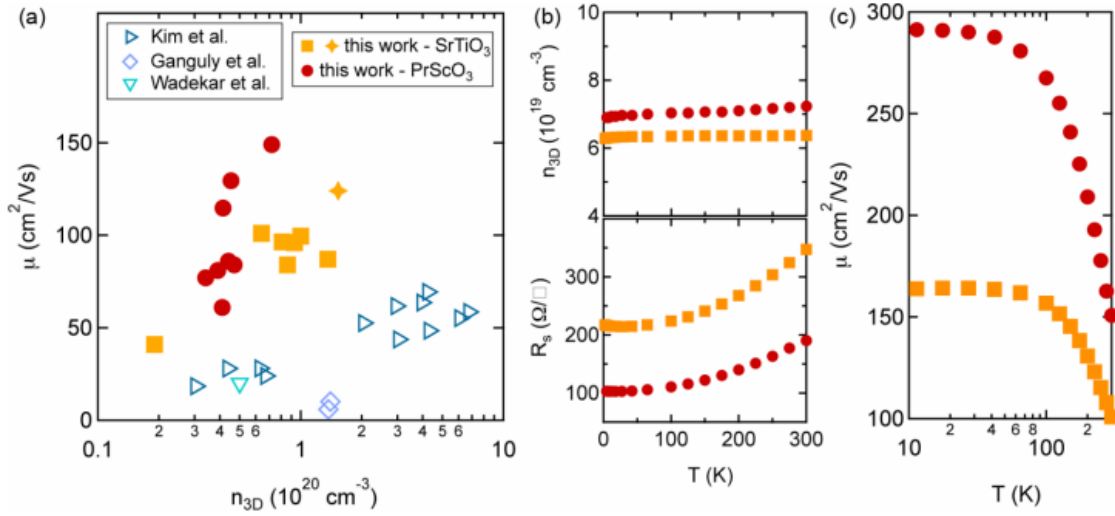
Figure 1-2: (a) Room temperature mobility as a function of carrier density for $BaSnO_3$ films grown at UCSB and from reports in literature [20, 22, 23]. A film on $SrTiO_3$ (starred) is 64 nm, while the rest of the films are 32 nm thick. (b) Carrier density, sheet resistance, and (c) mobility μ in the temperature range of 300 to 4 K. The $BaSnO_3$ films are on $SrTiO_3$ (orange squares) and $PrScO_3$ (red dots) substrates, respectively. The figure is reprinted from [25] with the permission of AIP publishing.
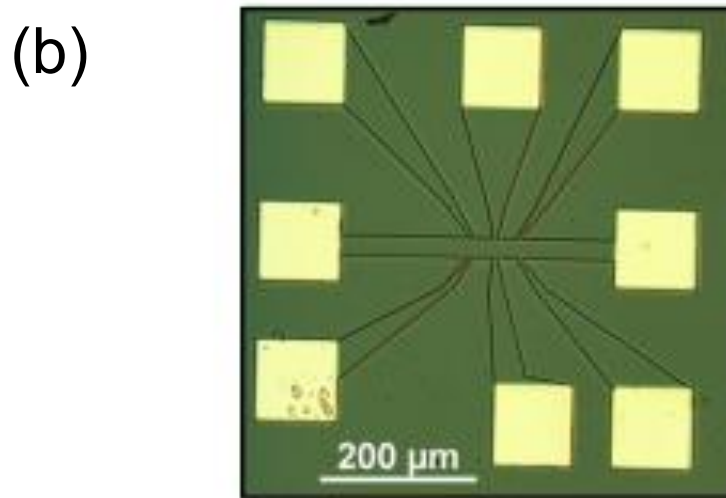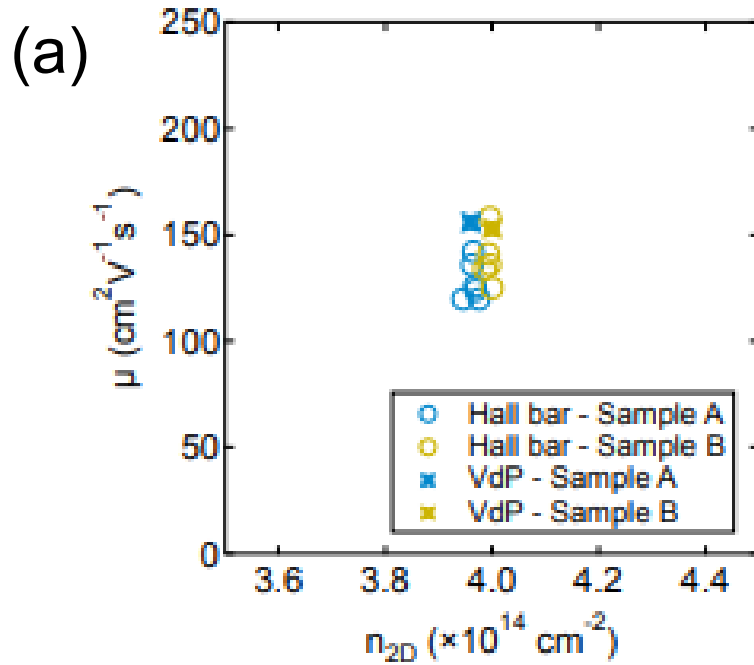
Figure 1-3: (a) Hall mobilities as a function of 2D carrier densities for two different BaSnO$_3$ films. Different data points are extracted from Hall bars fabricated on different regions of the films. The stars mark the mobility measured by the Van der Pauw method. (b) Optical micrograph of a BaSnO$_3$ Hall bar. The Figure is reprinted from [31], with copyright (2020) by the American Physical Society.
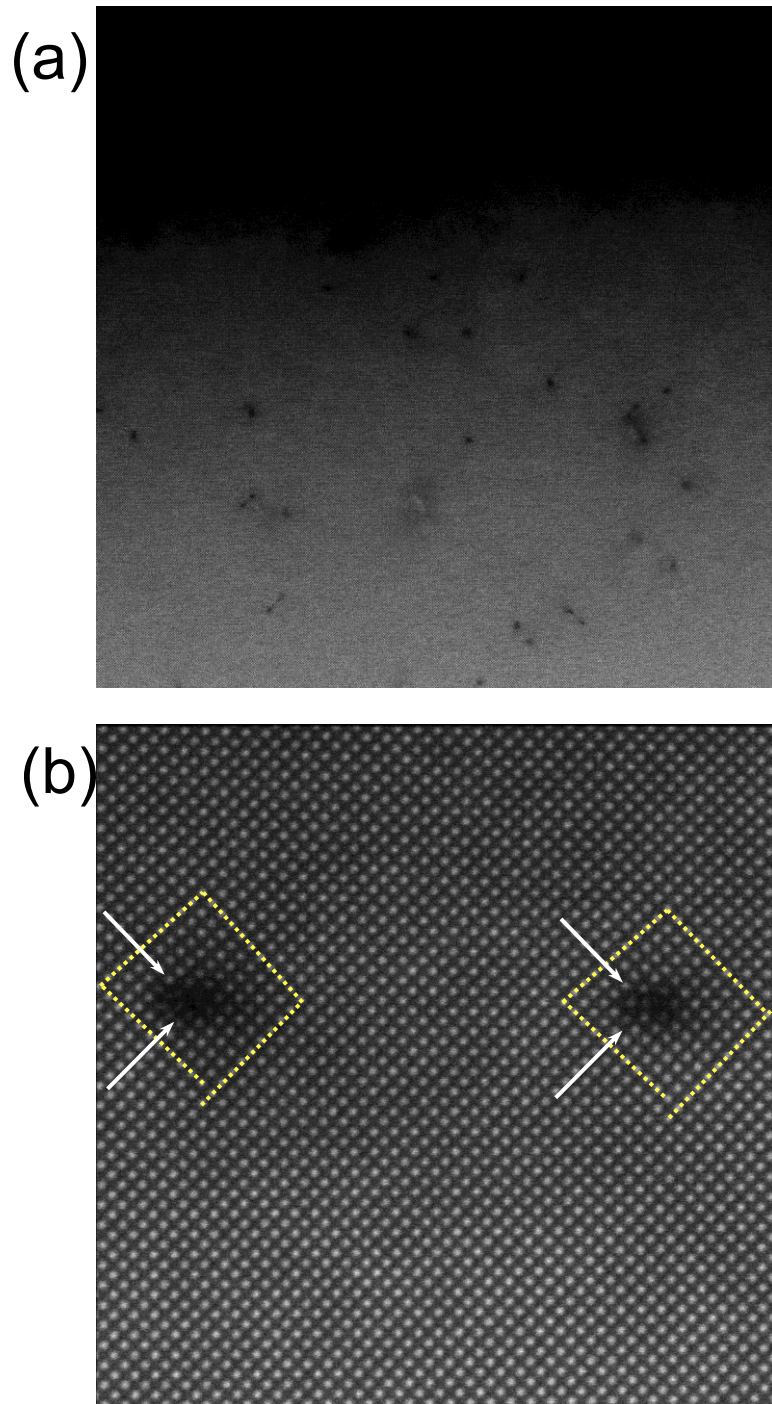
Figure 1-4: (a) Low- and (b) high- magnification plan-view HAADF-STEM images of 50 nm $BaSnO_3$ grown on $DyScO_3$ (001). White arrows mark dislocations. TEM courtesy of Honggyu Kim.
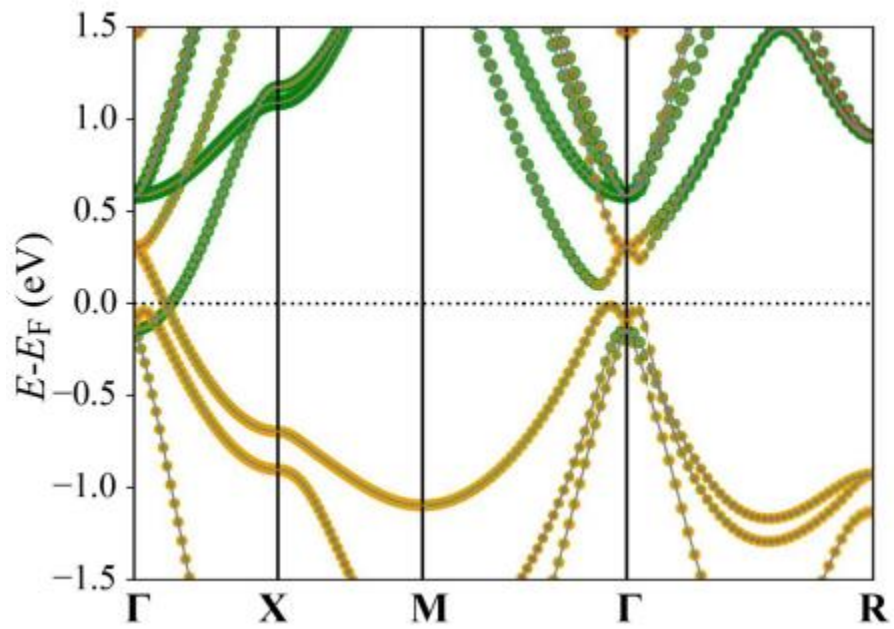
Figure 1-5: Band structure of Sr_3SnO calculated with taking spin-orbit coupling into consideration. The figure is reprinted from [53], with copyright (2021) by the American Physical Society.
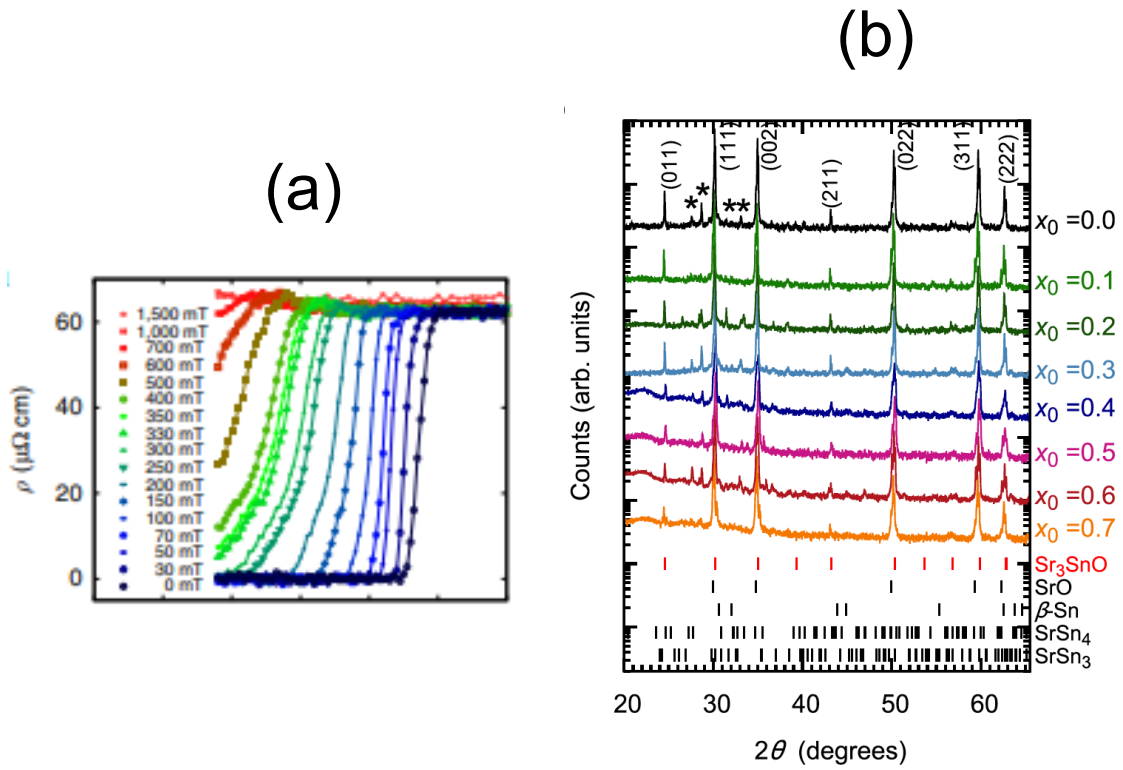
Figure 1-6: (a) Superconducting transition of $Sr_{3-x}SnO$ polycrystalline ceramics under different magnetic fields, reprinted from [43]. (b) XRD scan of $Sr_{3-x}SnO$ samples with various Sr vacancies, reprinted from [45]. The license link for reprint is https://creativecommons.org/licenses/by/4.0/.

Chapter 2 Materials synthesis, characterization, and measurement methodologies

This chapter discusses the experimental methodologies used in this thesis. Section 2.1 presents the molecular beam epitaxy (MBE) method by which all the investigated Sr_3SnO and $BaSnO_3$ films in this work were grown. Section 2.2 introduces the methods to characterize the structural and electrical properties of Sr_3SnO. This includes methods to overcome the experimental challenges caused by the air sensitivity of Sr_3SnO. Section 2.3 discusses the growth and measurement methods for $BaSnO_3$ films on small (3×3 mm) $SrZrO_3$ substrates. It is shown that uniform growth and accurate electrical measurements are difficult to achieve on films grown on these small substrates. In this thesis, a newly designed 3×3 mm MBE faceplate (i.e. sample holder) is introduced for uniform $BaSnO_3$ film growth, and Hall bar structures are used to measure the transport properties accurately. Section 2.4 briefly discusses secondary-ion mass spectrometry (SIMS) technique that measures the carbon concentration in the $BaSnO_3$ films.

2.1 MBE and the growth of Sr_3SnO and $BaSnO_3$ films

MBE is a powerful materials growth technique that serves as a frontier to explore high-quality single crystal thin films with ultra-high structural perfection. It is unparalleled among various vacuum deposition methods due to its precise control of composition, purity, and quality [54, 55]. The base pressure of MBE can be as low as 10^{-11} Torr, which makes the mean free path of a particle inside the chamber a few hundred kilometers [54, 55]. This allows for low degrees of contamination and high-purity growths. Additionally, the source materials are thermally sublimated from effusion cells, and the energies of the atomic fluxes are on the order of 0.1 eV [56], which is a few magnitudes lower than that of other physical deposition methods, such as sputtering and pulsed laser deposition. This allows for the minimization of energetic

defects. Finally, MBE is typically equipped with an *in-situ* monitoring technique that can give instantaneous information about the surface morphology of the film during the growth. Operators can use this information to understand the growth mechanism and adjust the parameters to achieve desired growth properties.

Figure 2-1 presents the basic configuration of an oxide MBE growth chamber (buffer chamber and load lock chamber not shown). The entire chamber is shrouded by liquid nitrogen to lower the base pressure, which is monitored by an ion gauge. The source materials are evaporated from effusion cells that point towards the substrate holder. Shutters are placed at the outlet of the effusion cells to turn the fluxes on or off. A heater is located behind the substrate holder to provide heat to the substrate, increasing the adatom mobility during the growth. Another ion gauge called the beam flux monitor (BFM) is located behind the substrate heater. The BFM can be rotated (by a motor) to face the effusion cells and measure the beam equivalent pressure (BEP) of the flux from each cell. The *in-situ* monitoring technique, as mentioned above, is reflection high-energy electron diffraction (RHEED). This technique directs a high-energy electron beam towards the film surface at a low incident angle and the resulting diffraction pattern is observed on a phosphor screen. The electron beam only penetrates a few atomic layers, and thus the pattern is a representation of the reciprocal lattice of the surface [57]. For example, a perfect surface lattice would show spots along the Laue circle. A residual gas analyzer can detect the mass spectrum of the chemical species in the main chamber. In addition, the substrate holder can be rotated to face the buffer chamber to allow for sample transfer using a mechanical arm. The buffer chamber isolates the main chamber from direct contact with the load lock chamber, to further reduce main chamber contamination.

The Sr$_3$SnO films in this work were grown by an oxide MBE (GEN 930, Vecco Instruments). Elemental Sr (4N, Sigma Aldrich) and SnO$_2$ (4N, Kurt J. Lesker) were co-evaporated from effusion cells as source materials during the growth. High-purity In (7N, United Mineral Corp) was co-supplied when a dopant was needed (discussed in Chapter 4). The main flux from the SnO$_2$ cell is SnO and O$_2$, where the pre-oxidized Sn facilitates high-quality stannate growth, as mentioned in Chapter 1. The substrate was chosen to be LaAlO$_3$ (a = 3.79 Å). The lattice mismatch between Sr$_3$SnO (5.12 Å) and the substrate is about 4% when the growth proceeds as the unit cell of Sr$_3$SnO having a 45° in-plane rotation relative to the substrate (5.12 Å /$\sqrt{2}$ = 3.62 Å, see Figure 2-2 (a) for the in-plane epitaxial relationship). Therefore, the Sr$_3$SnO films are expected to be relaxed. This 45° in-plane rotation is confirmed by an *x*-ray diffraction (XRD) ϕ scan (Figure 2-2 (b)), where the 202 peaks of Sr$_3$SnO and LaAlO$_3$ are offset by 45°. A 350 nm layer of Mo was deposited on the backside of the substrate to improve the heat transfer from the substrate heater. The substrate was cleaned in acetone and isopropanol before loading into the load lock chamber, where it was then baked at 200 ºC. After transferring into the main chamber, the substrate was heated to the growth temperature of 650 ºC and kept for 10 mins to ensure the substrate was homogeneously heated. The growth was then started by opening the shutters of Sr and SnO$_2$ cells. The temperatures of the cells were pre-determined (using the BFM measurement before growth) to precisely control the atomic fluxes and therefore the films' stoichiometry. In the case of Sr$_3$SnO, Sr flux was kept constant, and SnO$_x$ flux was varied to achieve different BEP ratios. RHEED was used for real-time characterization.

The BaSnO$_3$ films in this work were grown in the same MBE system. The source materials were Ba (4N, Sigma Aldrich) and SnO$_2$ (4N, Kurt J. Lesker). In most films, oxygen

plasma was co-supplied to help the oxidization. Oxygen was not supplied in a few film growths for the study of point defects and will be discussed in detail in Chapter 6. La was used to degenerately dope the $BaSnO_3$. The commercially available substrates used were $SrTiO_3$, $DyScO_3$, and $PrScO_3$. All have relatively large mismatch with the lattice of $BaSnO_3$. A study of using lattice-matched substrates (not widely commercially available) is discussed in Chapter 5. Similar to those used for Sr_3SnO growth, the substrates were backed with a 350 nm layer of Mo and cleaned before loading into the load lock chamber. The substrate temperature for $BaSnO_3$ film growth varied between 700 to 900 ℃. The substrate was annealed at the growth temperature for 10 mins under oxygen plasma (10^{-5} torr), after which the growth proceeded by opening the source shutters while keeping the plasma on. The method for varying the flux ratio is similar to that used for Sr_3SnO growth, only here, the Ba flux is kept constant while the SnO_x flux is varied. RHEED was also used for *in-situ* monitoring.

2.2 Methodologies for the structural and electrical characterization of Sr_3SnO

Ex-situ characterization of Sr_3SnO is challenging due to its extreme air sensitivity. Covering the Sr_3SnO samples with grease (or vacuum sealant) can enable XRD measurements, but the protection is not perfect. These Sr_3SnO samples have a tendency to degrade during a relatively long XRD measurement, and thus the diffraction pattern may not reflect that of a non-degraded film. Moreover, the phase purity of the samples cannot be ascertained because non-epitaxial impurity phases with a low volume fraction may not be detected in XRD.

A solid capping layer was used to replace the grease layer to solve this problem. Either TiO_2 or ZrO_2 was chosen as the protection layer (see Figure 2-3 (a) for the schematic of the structure). These were grown by using metalorganic precursors, titanium isopropoxide (TTIP), and zirconium tert-butoxide (ZTB), respectively. The precursors were delivered to the MBE

growth chamber via a gas inlet tube that was heated to ~100 °C to avoid condensation of the precursors. The precursor flow rate was measured by a capacitive manometer and controlled via a linear leak valve. The substrate temperature was 375 °C during the growth, at which point the precursors decompose into TiO_2 or ZrO_2, respectively. It was found that a ~300 nm capping layer was needed to protect the center of the Sr_3SnO films from degradation for a few hours in the air while the sides were still exposed and degraded. The structural characterization was therefore performed on the center of the films.

The longer sample lifetime afforded by the structure shown in Figure 2-3 (a) allows for cross-section imaging using a scanning electron microscope (SEM) equipped with a focused ion beam (FIB) source after the XRD measurements are performed. A schematic of the FIB/SEM is shown in Figure 2-3 (b). The FIB can be used to cut a rectangular groove, leaving one wall to be the cross-section. The electron beam is positioned at an angle to the film surface such that the cross-section can be imaged. The entire FIB/SEM process is typically performed at pressures of ~ 10^{-5} - 10^{-7} Torr and thus is not likely to degrade the exposed regions. A Pt protection layer is usually deposited on the selected surface prior to FIB cutting.

The structure in Figure 2-3 (a), however, cannot be used for electrical measurements. This is because the electrical contacts must be put on the sides for Van der Pauw measurement, but the sample sides are typically degraded. Therefore, the protection layer must fully cover the entire film (including the sides). In addition, the time of air exposure of the films, even with protection, should be minimized as much as possible because the presence of a small amount of the degradation products, such as Sn [43-46], can significantly impact the transport behavior.

The first attempted method involved In soldering to make the electrical contacts and then using Apiezon-N grease to cover the rest of the exposed surface. The contact-making process was performed in a glove bag filled with N_2 (Figure 2-4 (a)). After In contacts were made and grease was put on, the Sr_3SnO film was moved to a smaller N_2 bag and then transferred to a physical property measurement system (PPMS) for electrical measurements. The PPMS chamber pressure was kept below 10^{-3} Torr. This method resulted in a few initial successful measurements that show similar electrical behaviors as those reported in other works [43-50]. However, working in a glove bag was found to be difficult due to the small size of contacts and wires. The process was long (~20 to 30 mins), and the films were partially degraded. The glove bag was later upgraded to a glove box (Figure 2-4 (b)), in which the soldering work could be finished faster (~10 to 20 mins). Soldering in the glove box, however, was later found to degrade the films slightly, compared to a more advanced method (transport data will be discussed in Chapter 3).

A modified method further minimizes the contact-making time by avoiding the need to solder electrical contacts directly to the sample. It instead relies on mechanical attachments, as shown in Figure 2-5 (a). The connection between the PPMS puck and the attachments can be pre-soldered before placing the sample in the glove box (Figure 2-5 (b)). Thus, once a Sr_3SnO film was transferred into the glove box, the only remaining task was to position the film on the puck (shown in Figure 2-5 (b)), slide in the attachments, and tighten the screws such that the In could mechanically contact the corners of the film (see a schematic of the mechanical contacts in Figure 2-5 (c)). This process only takes about ~2 to 3 mins and therefore can significantly reduce the degradation. In addition, the Apiezon-N grease was diluted with a few

drops of toluene such that it had a sufficiently low viscosity, allowing it to cover the entire film (including the sides).

2.3 MBE growth and electrical measurement of BaSnO$_3$ on 3 × 3 mm SrZrO$_3$ substrate

Eliminating threading dislocations is critical for the study of transport of BaSnO$_3$ thin films because only then we can understand if other defects also limit the carrier mobility, as mentioned in Chapter 1. Most commercially available MBE substrates are lattice-mismatched with BaSnO$_3$ and thus can create threading dislocations by strain-relaxation. The motivation for growing BaSnO$_3$ on a relatively small SrZrO$_3$ substrate is that SrZrO$_3$ is lattice-matched with BaSnO$_3$ (~ 0.3%) [58] but the largest substrate that the vendor (MatTek) was able to provide were 3 × 3 mm squares.

A significant challenge in MBE on a 3 × 3 mm substrate is the faceplate design (i.e. MBE substrate holder). The faceplate design for 10 × 10 mm substrate is shown in Figure 2-6. However, this design cannot be scaled down and used for 3 × 3 mm substrate because the support pins are ~1 mm in length, and they would cover most of the area of the small-sized substrate. Therefore, a customized faceplate redesign was needed.

The initial design is shown in Figure 2-7. The idea is to replace the support pins with four wire springs that can clamp the substrate by its edges. The four wire springs are installed by piercing through the metal plate (see Figure 2-7 (b) for the back view). A wire grid is placed on the backside of the center hole (where the substrate sits) to prevent the substrate from falling through. MBE growths were performed using this faceplate design. However, this design is not optimal because the back grid causes non-uniform heating and the exposed part of the wire

springs on the backside of the faceplate does not allow for the use of a quartz plate to increase heat transfer.

To solve the inhomogeneous and insufficient heating problem, an improved design is shown in Figure 2-8. The center hole in this faceplate design is slightly smaller than 3×3 mm, so the slightly larger size of the substrate can prevent it from falling through. This allows for the elimination of the back grid and leads to more uniform heating. In addition, the wire springs in this new design are installed using screwed stages and therefore do not extend through the backside. A quartz plate can then be placed behind the faceplate to improve heat transfer (Figure 2-8 (b)).

The faceplate design shown in Figure 2-8 allows 3×3 mm $BaSnO_3$ thin films to be grown with similar quality to those grown on 5×5 mm substrates. However, a remaining question is how to perform electrical measurements on these 3×3 mm films, since Van der Pauw method generally utilizes electrical contacts placed on the edges, but the edges of these samples are poorly heated during growth due to the faceplate design. One solution is using a Hall bar structure (Figure 1-3 (b)) processed on the film's center, which allows for the region being measured to be of higher-quality material. In a 3×3 mm $BaSnO_3$ film grown on a $DyScO_3$ substrate, it was seen that the Van der Pauw mobility was measured to be 53 $cm^2V^{-1}s^{-1}$ while the Hall bar mobility was 124 $cm^2V^{-1}s^{-1}$.

2.4 Introduction to SIMS and SIMS measurement of carbon in $BaSnO_3$

SIMS is a technique used to determine the concentration of impurities in a solid. It utilizes a focused ion beam to sputter the surface of the solid and measures the ejected secondary ions [59]. These secondary ions are collected and filtered according to their atomic

mass. The resulting mass spectrum can be used for elemental, isotopic, or composition analysis [59]. SIMS is the most sensitive elemental analysis tool that can measure the concentration of impurities at the level of parts per million. In addition, high energy can be applied to the ion beam such that it can etch into the specimen and provide a depth profile along the etching path [59]. Because the ionization probabilities of species sputtered from dissimilar solids are very different, a standard sample with a known concentration profile of the target species is necessary for quantitative analysis. The conversion from SIMS signal intensity to a quantitative concentration distribution is achieved by using a relative sensitivity factor (RSF), defined by:

$$C_i(t) = RSF \times \frac{I_i(t)}{I_R(t)} \quad , \quad \quad \quad \quad (2\text{-}1)$$

where $C_i(t)$ and $I_i(t)$ refers to the concentration and intensity of the element of interest, and $I_R(t)$ is the intensity of a reference element (any other element in the material). The standard sample (with known $C_i(t)$, and measured $I_i(t)$ and $I_R(t)$) is first used to derive the RSF, and the RSF is then used to calibrate the element of interest in unknown samples.

This thesis uses SIMS to determine the carbon concentration depth profile for $BaSnO_3$ thin films. A ~40 nm amorphous Si layer was pre-deposited on the $BaSnO_3$ films using Ar plasma sputtering to allow for reaching a steady state etching condition before the primary ion beam reaches the $BaSnO_3$ layer. The amorphous Si guarantees no preferential etching along grain boundaries. Prior to the measurement, the samples were cleaned in acetone, isopropanol, and de-ionized water, and then loaded into the entry/exit chamber for an 80 ℃ overnight bake. The base pressure of the SIMS chamber was ~10^{-10} Torr. A 15 kV Cs^+ primary ion beam (Cameca IMS 7f) was used to sputter and etch the samples. During the measurement, a 5 kV electron flood was co-supplied to charge-neutralize the films. The beam raster area was $100 \times$

$100\ \mu m^2$, and the $^{12}C^-$ secondary ions were received from the center of the $33\ \mu m^2$ etched crater. The etch rate was about 2.5 nm/s. The average RSF of the carbon element (using Sn as the reference species) for two standard $BaSnO_3$ thin films implanted with ^{13}C (CuttingEdge Ions, LLC, Anaheim) was first determined and then used to calibrate the ^{12}C depth profile in other $BaSnO_3$ thin films.
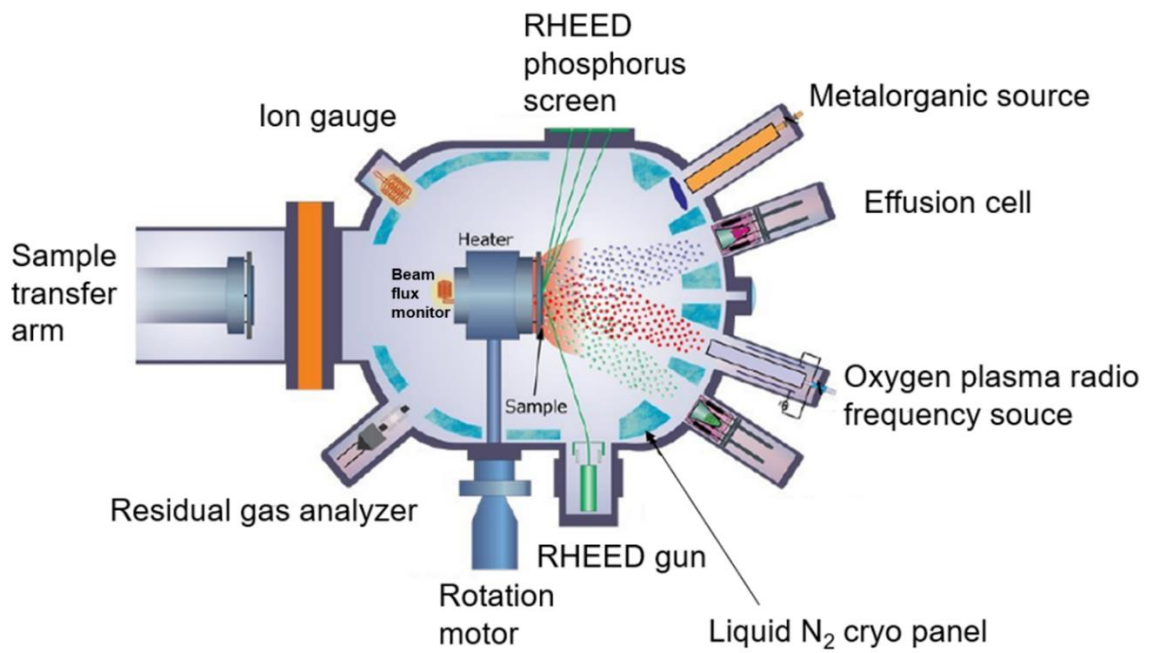
Figure 2-1: A schematic of a MBE growth chamber.
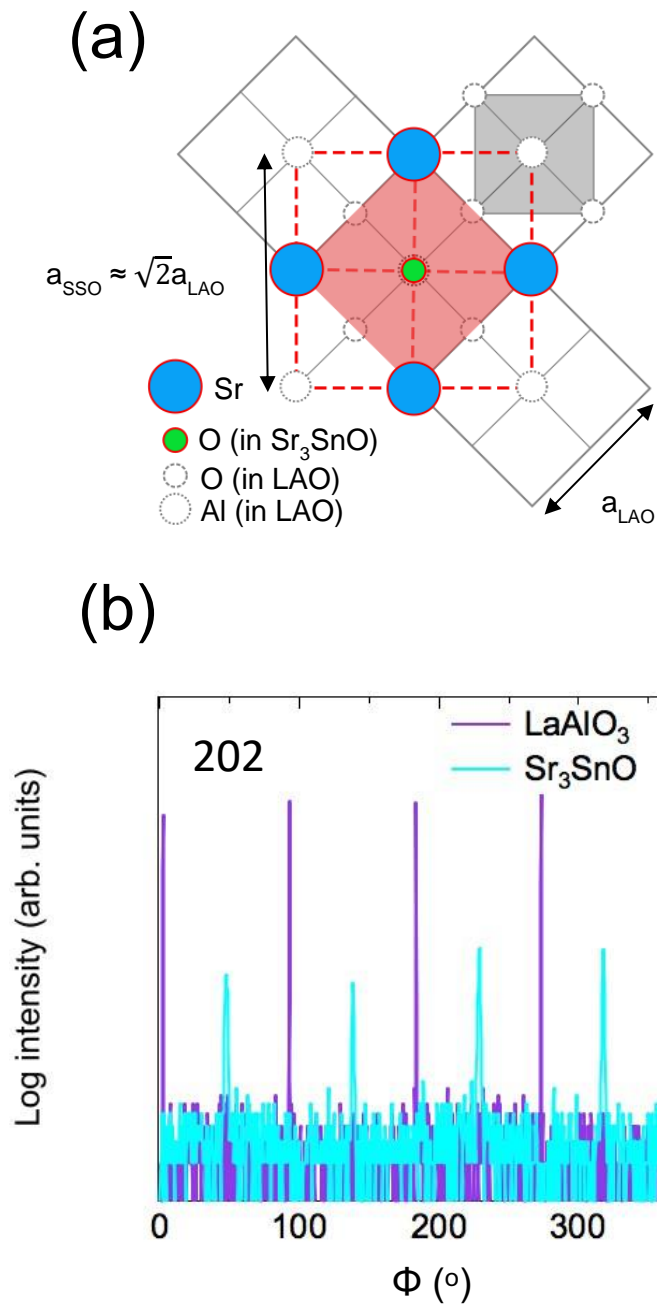
Figure 2-2: (a) The epitaxial relationship of Sr_3SnO grown on $LaAlO_3$ (001) substrate with a 45° in-plane rotation. Courtesy of Nick Combs. (b) XRD ϕ scan of 202 reflections of the Sr_3SnO thin film and the $LaAlO_3$ substrate.

(a)

ZrO$_2$ or TiO$_2$

(001) Sr$_3$SnO

(001) LaAlO$_3$

(b)

FIB etching

SEM
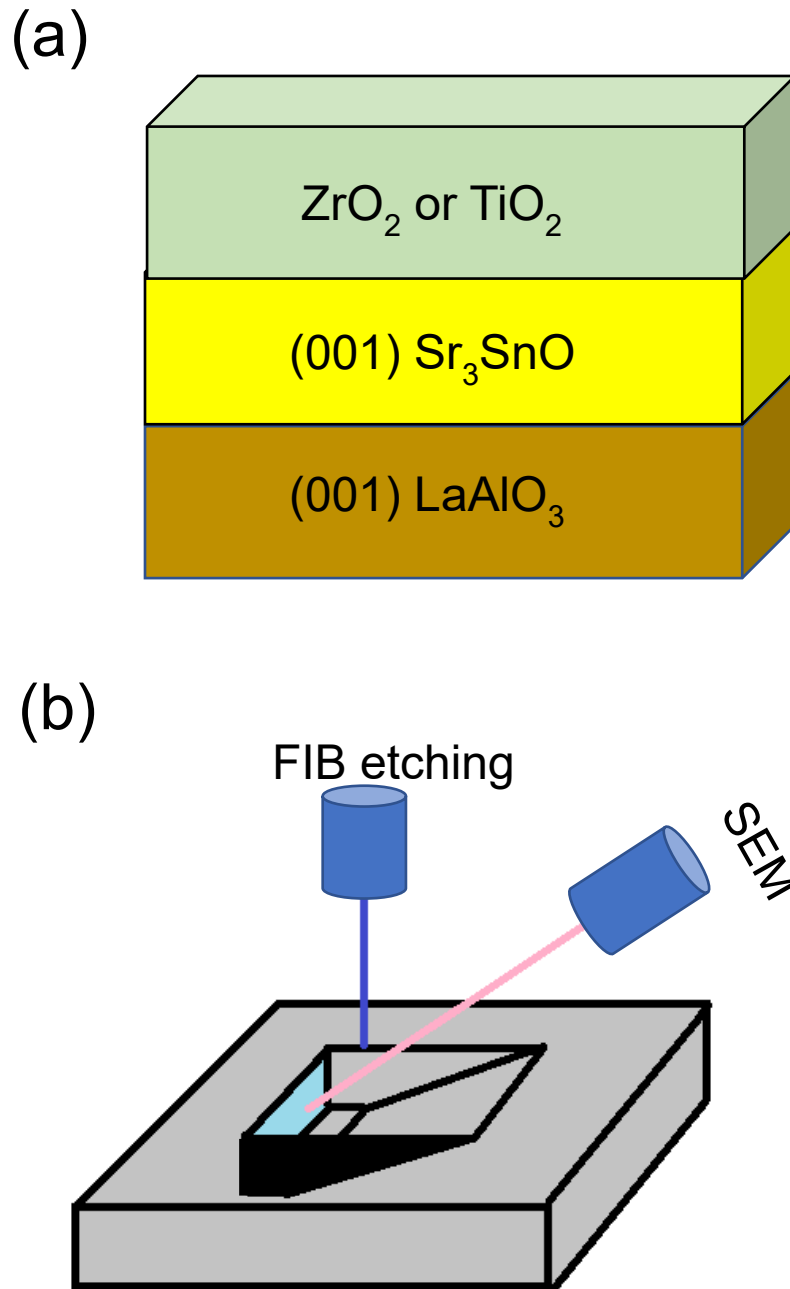
Figure 2-3: (a) The heterostructure of Sr$_3$SnO and oxide capping layer. The sketch does not reflect the real dimensions. (b) A schematic diagram of the FIB/SEM configuration.
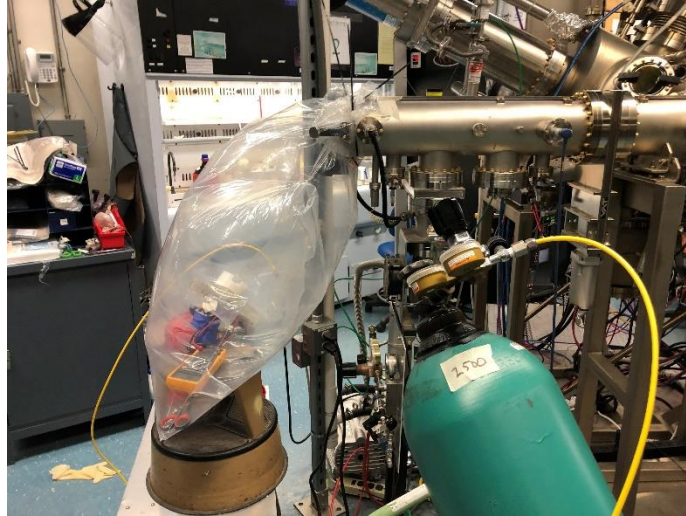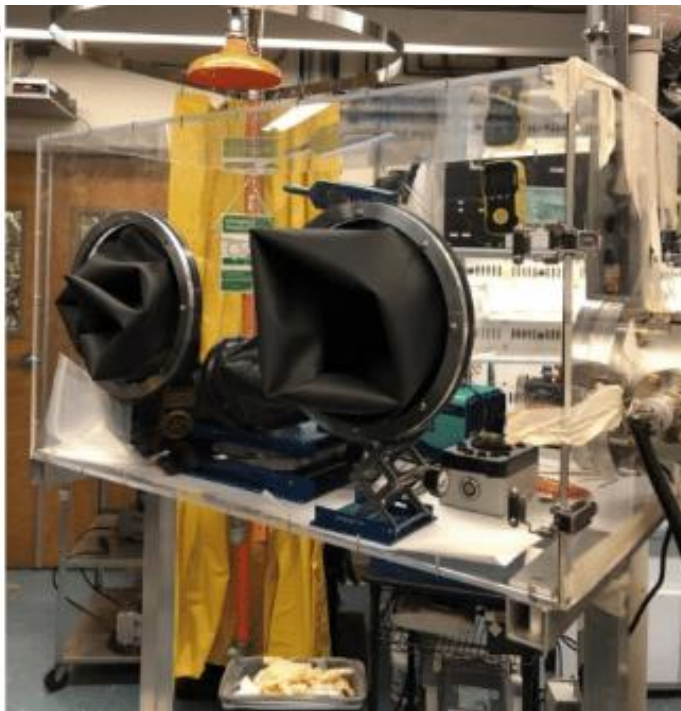
Figure 2-4: (a) Glove bag and (b) box attached to the entry/exit chamber of an oxide MBE (GEN 930, Vecco). Photos taken at the MBE laboratory at UCSB.
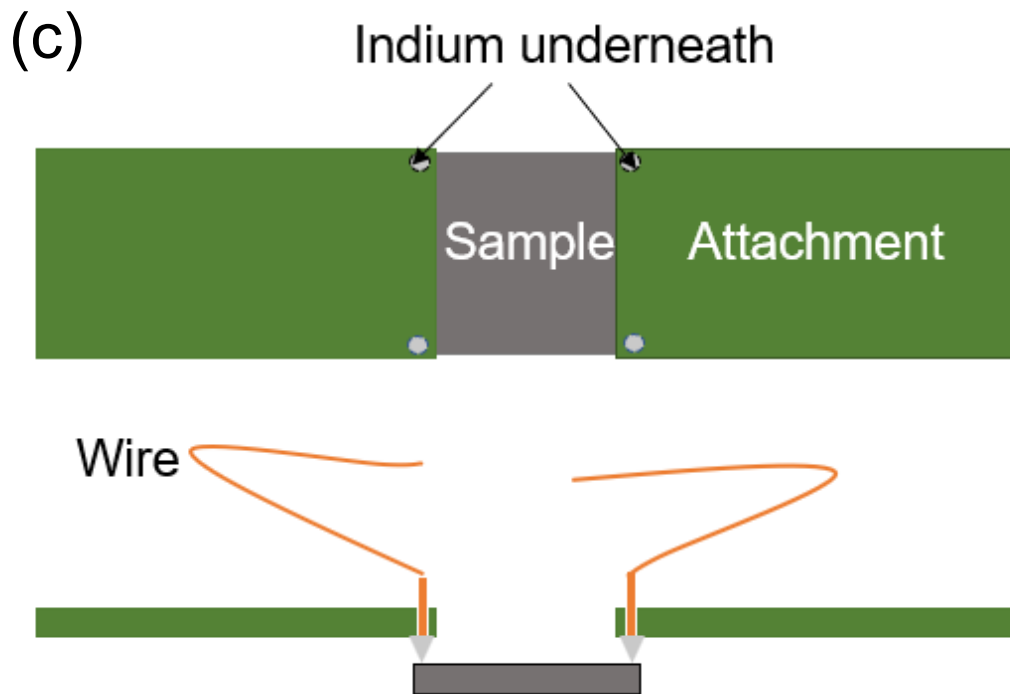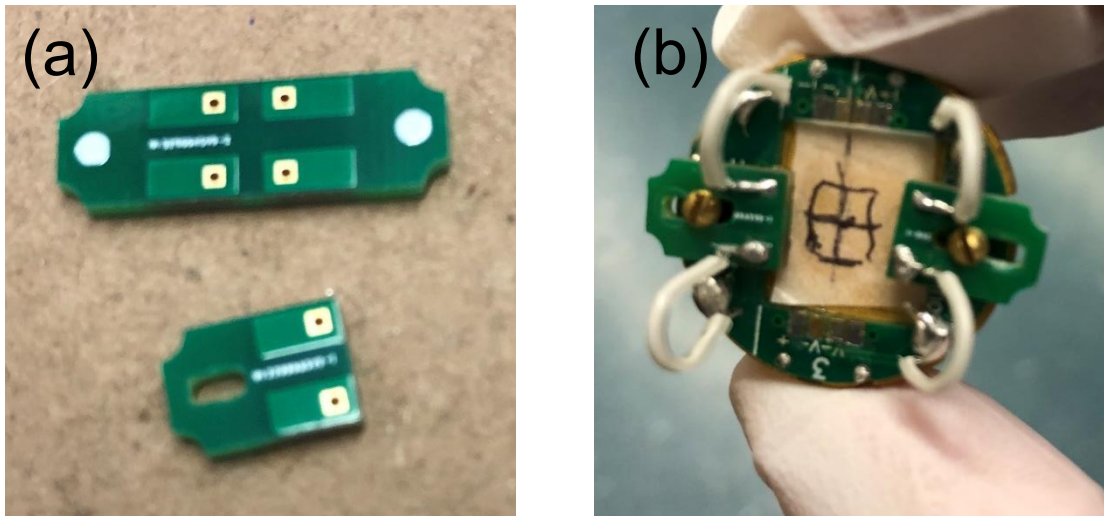
Figure 2-5: (a) Attachments that can be used to make electrical contacts. (b) PPMS puck with two pre-soldered attachments. The position for the placement of the film is drawn at the center of the puck. (c) A schematic diagram of the electrical contacts made by the attachments.
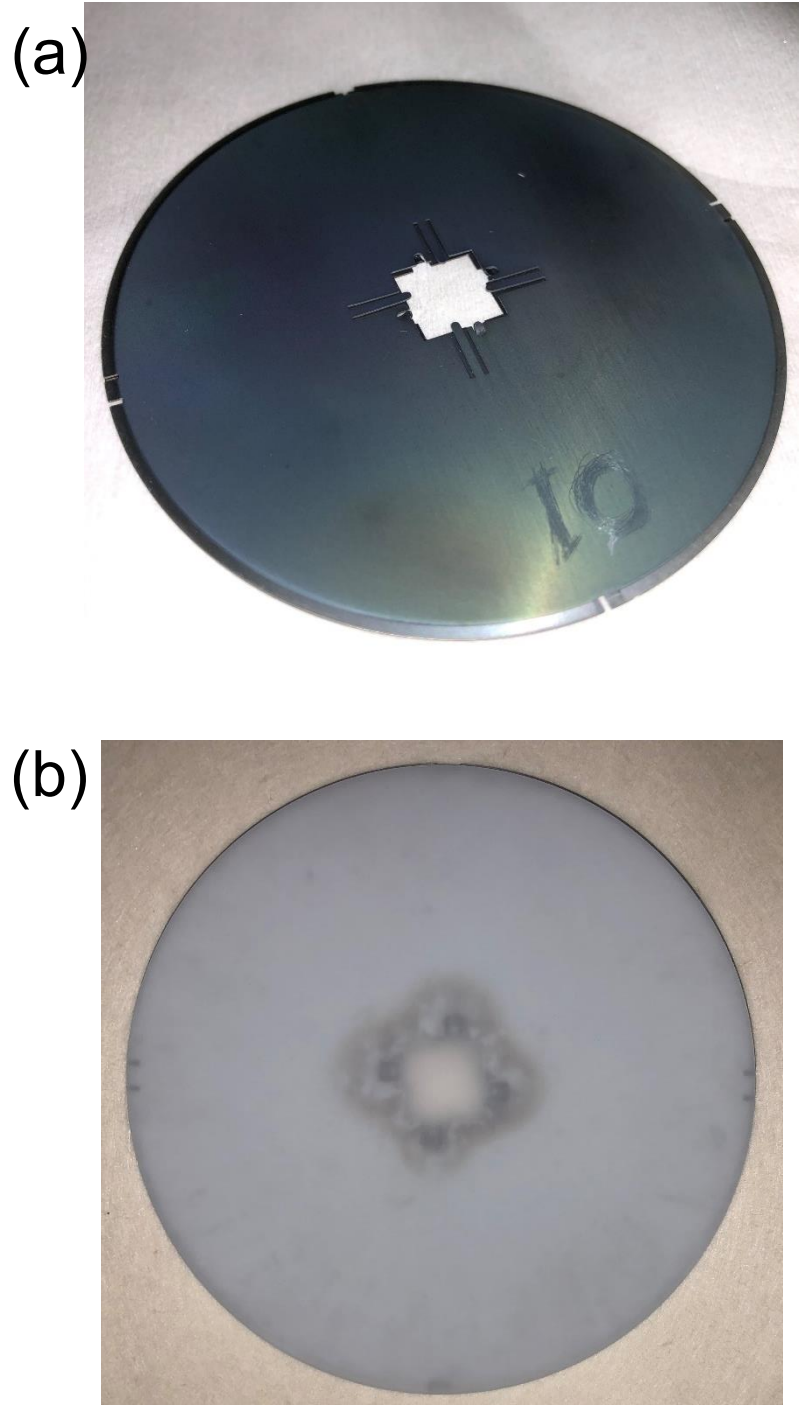
Figure 2-6: (a) Front and (b) back side of an oxide MBE faceplate with a 10×10 mm center hole for the substrate.
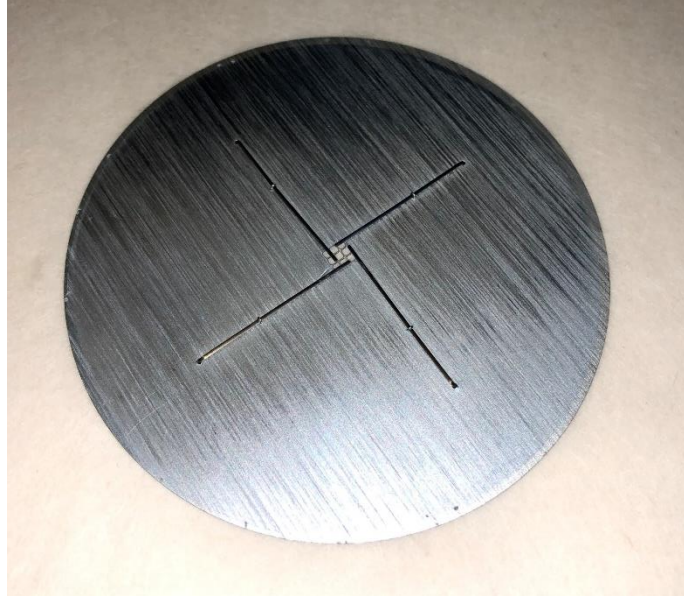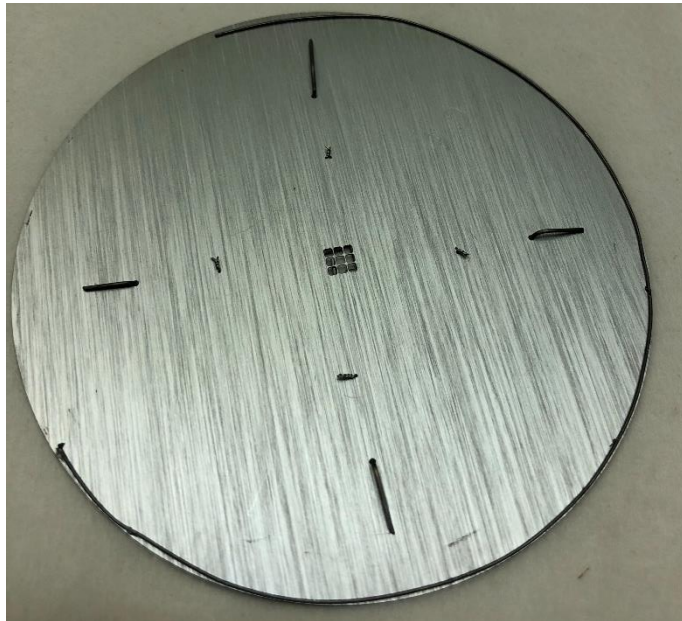
Figure 2-7: (a) Front and (b) back side of a four wires design of an oxide MBE faceplate with a 3 × 3 mm center hole for the substrate.
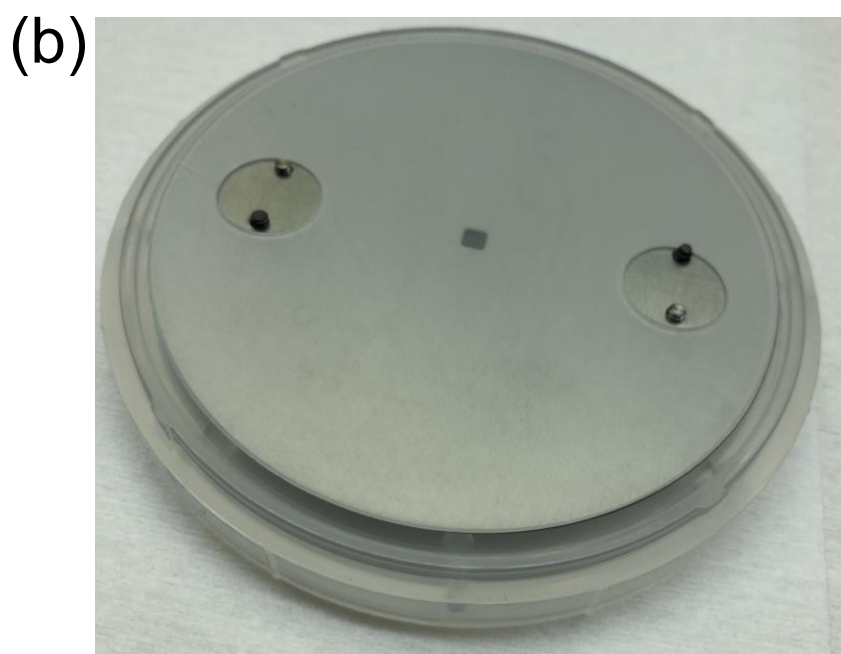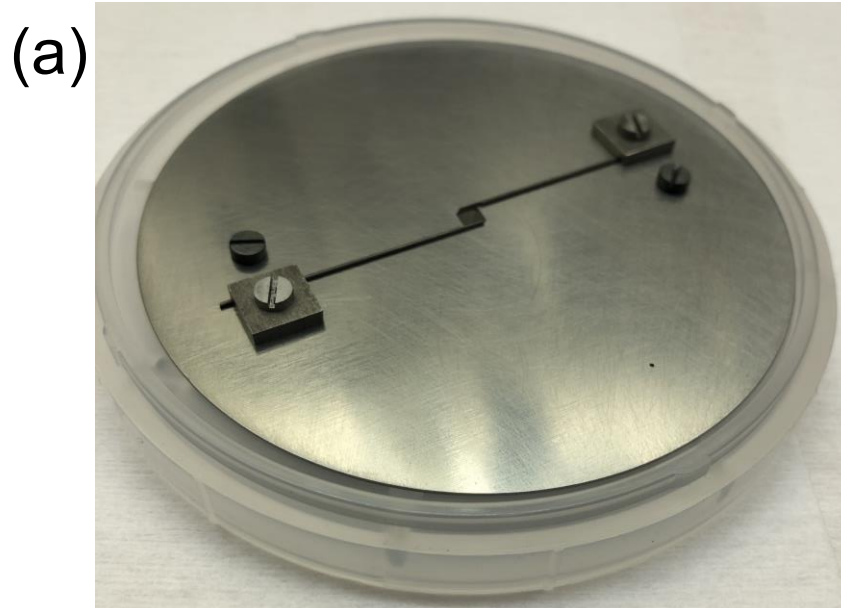
Figure 2-8: (a) Front and (b) back side of a two wires design of an oxide MBE faceplate. The center substrate hole is slightly smaller than 3 × 3 mm.

Chapter 3 Molecular beam epitaxy of phase-pure Sr₃SnO antiperovskite oxide

Highly Sr-deficient $Sr_{3-x}SnO$ has been proposed as a possible topological superconductor because it is a topological crystalline insulator, and a superconducting transition in bulk $Sr_{3-x}SnO$ ($x \sim 0.5$) polycrystalline ceramics is experimentally observed at $\sim$ 4 K. However, a variety of impurity phases, such as Sn, are also found in these superconducting $Sr_{3-x}SnO$ samples. Sr_3SnO thin film studies have also been performed, but none of them could conclusively prove the phase purity of Sr_3SnO due to its extreme air sensitivity. This background motivates this chapter's work (see Chapters 1 and 2 for detailed introduction and methodologies, respectively).

I acknowledge that Figures 3-1 to 3-8 in this chapter are reprinted from Appl. Phys. Lett. **119**, 161903 (2021), with the permission of AIP Publishing. Figures 3-9 to 3-11 are reprinted from Appl. Phys. Lett. **121**, 233101 (2022), with the permission of AIP Publishing.

3.1 Stoichiometric control and phase purity determination

As is discussed in Chapter 2, thin film growth of Sr_3SnO is achieved by oxide MBE, which can control the film stoichiometry by varying the Sr/SnO_x beam equivalent pressure (BEP) ratio. The films discussed in this section are capped with an oxide layer for structural characterizations (Figure 2-3 (a)). In this study, the Sr BEP is kept at 5.0×10^{-7} Torr, and the BEP from the SnO_2 cell is varied to grow four films with the Sr/SnO_x BEP ratios of 12.5, 8.7, 4.2, and 2.1, respectively. The corresponding growth rates of these films are 140, 200, 480, and 850 nm/hr, and are therefore SnO_x flux limited. The substrate is $LaAlO_3$ and is kept at 650 ºC during the growth.

Figure 3-1 shows these four films' reflection high-energy electron diffraction (RHEED) patterns. Spotty features are observed in all the patterns, indicating the formation of three-

dimensional islands. The spotty-ness turns more pronounced when the growth condition becomes more Sn-rich. The following discussions on the *x*-ray diffraction (XRD) patterns and images taken by scanning electron microscope (SEM) equipped with a focused ion beam (FIB) will show that only the film shown in Figure 1 (a) is phase pure.

Figure 3-2 (a) shows 2θ-ω XRD patterns of the Sr_3SnO films shown in Figure 3-1. All the on-axis peaks can be assigned either to the (001) Sr_3SnO film or the (001) $LaAlO_3$ substrate, with no other reflections detected. However, absence of other reflections is not sufficient evidence that the Sr_3SnO films are phase-pure because the peaks can be of low intensity if the impurities are poorly crystallized, randomly oriented, or present in small quantities. Moreover, another well-known issue of using on-axis XRD to characterize the purity of Sr_3SnO is that SrO is a possible secondary phase. SrO has a lattice constant close to that of Sr_3SnO [52, 60], and thus the on-axis peaks of SrO cannot be distinguished from those of Sr_3SnO. The crystal structure of SrO is face-centered cubic [60] in which the 00l (when l is odd) peaks are forbidden. Therefore, the appearance of Sr_3SnO 001 and 003 peaks can indicate the existence of the Sr_3SnO phase but is insufficient to ascertain the absence of SrO impurity. The intensity of the Sr_3SnO 001 peaks (Figure 3-2 (b)) is higher in films grown with lower Sr/SnO_x BEP ratios because of the higher growth rates (and therefore, thicker films) resulting from the larger SnO_x fluxes.

To address the issues, cross-sectional SEM images are used to probe for secondary phases (See methodology in Chapter 2). As is shown in Figure 3-3 (a), the film grown with a Sr/SnO_x BEP ratio of 12.5 does not include any additional phases. Therefore, combined with the appearance of 001 and 003 peaks in XRD, this film appears to be phase-pure.

In the films grown with more Sn-rich conditions (Figure 3-3 (b)-(d)), a secondary phase shows up as a columnar and dark region. The volume fractions of the dark areas are 25%, 30%, to 45% in the films grown with Sr/SnO$_x$ BEP ratios of 8.7, 4.2 to 2.1, respectively. The increasing impurity volume fraction with increased SnO$_x$ flux indicates that the impurity phase is Sn-rich (such as a Sr-Sn alloy). Of importance, the Sn-rich impurity phase was not detected in XRD even in a film as thick as 850 nm. This result is significant because on-axis XRD is commonly used in Sr$_3$SnO thin film growth studies as evidence to assure phase purity [47, 48]. Still, here it is concluded that XRD alone is insufficient. Only at extremely Sn-rich growth conditions (Figure 3-4) where the columnar region has distinctively changed morphology can the impurity phase be detected in XRD (Figure 3-5).

3.2 Transport results

This section examines the electrical properties of two Sr$_3$SnO films grown with Sr/SnO$_x$ BEP ratios of 12.5 and 4.2, respectively. As introduced in Chapter 2, the Sr$_3$SnO films used for electrical measurement are not capped. They were grown straight after the growth of their capped counterparts (discussed in section 3.1) to ensure reproducibility. In the work of this section, the electrical contacts were made by soldering in a glove bag (Figure 2-4 (a)).

Figure 3-6 shows the sheet resistance, R_s, as a function of temperature for the Sr$_3$SnO films grown by Sr/SnO$_x$ BEP ratio of 12.5 and 4.2. Both films show metallicity followed by localization behavior (an upturn starting around 20 K) at low temperatures. This is consistent with other Sr$_3$SnO thin film results [47-50]. P-type transport behaviors are observed in both films (see Figure 3-7 for Hall effect), which can be attributed to Sr vacancies [43-50]. The carrier concentrations are 9.6×10^{18} cm^{-3} and 1.5×10^{19} cm^{-3}, respectively, with no carrier frozen at low temperatures. These carrier concentrations are well below those needed to induce

superconductivity in bulk $Sr_{3-x}SnO$ polycrystalline ceramics, which require a hole carrier density of at least 10^{21} cm^{-3} [43-46]. Moreover, even though the Sr/SnO$_x$ BEP ratio of 4.2 provides 200% more SnO$_x$ flux, the carrier density of the resulting Sr_3SnO film is only 50% higher than that of the phase-pure film. This is, as observed in Figure 3-3, because the excess Sn is not entirely incorporated into the Sr_3SnO phase to contribute more Sr vacancies but instead forms Sn-rich secondary phases. Surprisingly, the temperature dependences of these two Sr_3SnO films are qualitatively similar. It indicates that the impurity phases have very little influence on the transport, probably because the phase is not percolated to create a conductive path. The only difference is the higher R_s in the phase-pure film, but it is simply because of its lower carrier density. I note that by using more advanced measurement methods (see Chapter 2 for an introduction, Chapter 4 for data discussion), only the carrier mobility is improved but the temperature dependence of R_s still has the same qualitative behavior.

Figure 3-8 shows the magnetoconductance of the phase-pure Sr_3SnO film at low temperatures (2 K, 10 K, 50 K, and 150 K), with a perpendicular magnetic field applied from -14 to 14 T. The conductance is obtained by the inversion of resistance. The magnetoconductance at 150 K is proportional to B^2, which indicates the domination of classical orbital effects originating from the Lorentz force. The 50 K, 10 K, and 2 K data can be fitted to the Hikami-Larkin-Nagaoka model for weak antilocalization in the strong spin-orbit coupling limit (Figure 3-8 (b)) [61], described by:

$$\Delta G_{xx} = \alpha \frac{e^2}{h} \left[\ln \left(\frac{B_\varphi}{B} \right) - \psi \left(\frac{B_\varphi}{B} + \frac{1}{2} \right) \right] , \qquad (3\text{-}1)$$

where e is the elementary charge, h is Planck's constant, $l_\varphi = \sqrt{h/(8\pi e B_\varphi)}$ is the phase coherence length, ψ is the digamma function. The factor α takes -1 for weak localization (WL)

and ½ for weak antilocalization (WAL) [61]. The extracted values for α are 0.08, 0.30, and 0.45, and for l_φ are 44 nm, 87 nm, and 146 nm, at 50 K, 10 K, and 2 K, respectively. The observation of WAL in Sr$_3$SnO thin films is consistent with other work [49] and is also reported in other topological materials [62-70]. The fact that α approaches to 0.5 at 2 K indicates a Berry phase of π. It is important to note that the R_s upturn in Figure 3-6 is a characteristic of WL (not WAL). Therefore, the two seemingly incompatible behaviors, WL, and WAL, coexist in Sr$_3$SnO. This apparent contradiction is not uncommon in topological materials, while the physical cause is still under discussion [71-75]. One possible theory is that a system consisting of Dirac fermions can simultaneously host two processes, electron-electron interaction, and quantum interference [63]. Both processes are functions of magnetic field and temperature. The theory points out that the WL observed in the temperature dependence of R_s is caused by electron-electron interaction that decreases the conductivity to a more significant extent than the enhancement from the quantum interference, while the WAL shown in the magnetoconductivity is supported by both processes but mainly contributed by quantum interference [63].

3.3 Improved carrier mobility by reducing degradation

As introduced in chapter 2, the soldering work in an N$_2$ glove bag leads to a certain degree of degradation in the Sr$_3$SnO thin films due to the leakage of the bag and the trace amount of oxygen mixed even in the ultra-high purity N$_2$. To reduce the degradation, better dealing, and a faster way to make the electrical contacts are needed. Therefore, a glove box (Figure 2-4(b)) and a mechanical contact-making method (Figure 2-5) were applied.

Figure 3-9 shows the significant improvement (compared to soldering in the glove box) in the carrier mobility (Hall mobility measured at 10 K) of the Sr_3SnO thin films measured using the mechanical contact-making method. The highest carrier mobility at 10 K is 400 $cm^2V^{-1}s^{-1}$, which is achieved in the center of the phase-pure growth window (yellow-shaded) and is the highest record among all the Sr_3SnO films and bulk polycrystalline ceramics reported to date [43-50]. In addition, the same film has a carrier density of 4×10^{18} cm^{-3}, which is the lowest reported so far. The high mobility at a low carrier density indicates excellent materials quality. One may notice that the phase-pure growth condition discussed in section 3.2 is not sitting in the phase-pure window in Figure 3-9. This is because of the change of ion gauge and heater filament inside the MBE chamber, which commonly causes a shift in the apparent growth conditions. Moreover, Figure 3-9 also shows that the carrier mobility and density are very sensitive to the Sr/SnO_x BEP ratio. This is probably because point defects start to form when the growth condition is away from the center of the growth window. This observation is consistent with the XRD rocking curves shown in Figure 3-10. The full width at half maximums (FWHM) are 1.26, 1.07, and 0.80 for samples grown with Sr/SnO_x BEP ratios of 9.1, 7.6, and 8.2, respectively. The fact that the sample with the smallest FWHM has the highest carrier mobility indicates that point defects are likely formed at the edges of the phase-pure growth window. The point defects in Sr- or Ba- contained stannate films can be quite various and complicated. An example will be discussed in Chapter 6.

Figure 3-11 shows the temperature dependence of R_s for the phase-pure Sr_3SnO thin films shown in Figure 3-9. The R_s values are significantly lower than those in Figure 3-6, but the qualitative trend, including the metallicity and WL, is not changed. This is probably

because the degraded products in the films discussed in Figure 3-6 are insulators, such as hydroxide. It is also found that air exposure eventually makes Sr_3SnO thin films insulating.

3.4 Conclusion

This Chapter shows that MBE is an excellent technique for the stoichiometric control of Sr_3SnO thin films. The Sr vacancies in the phase pure Sr_3SnO films create p-type carriers with density values of mid-to-high 10^{18} cm^{-3}, which is a few magnitudes below that in superconductive bulk $Sr_{3-x}SnO$ crystals (10^{21} cm^{-3}). By significantly reducing the degradation of Sr_3SnO thin films within the phase pure window, a carrier mobility above 400 cm^{2}V^{-1}s^{-1} at 10 K can be achieved. Deliberate change in the stoichiometry to make more Sr vacancies only increases the number of carriers by less than a magnitude, but more prominently, it introduces Sn-rich impurity phases into the films. Therefore, a dopant becomes a better choice to increase the carrier density, which will be discussed in Chapter 4.
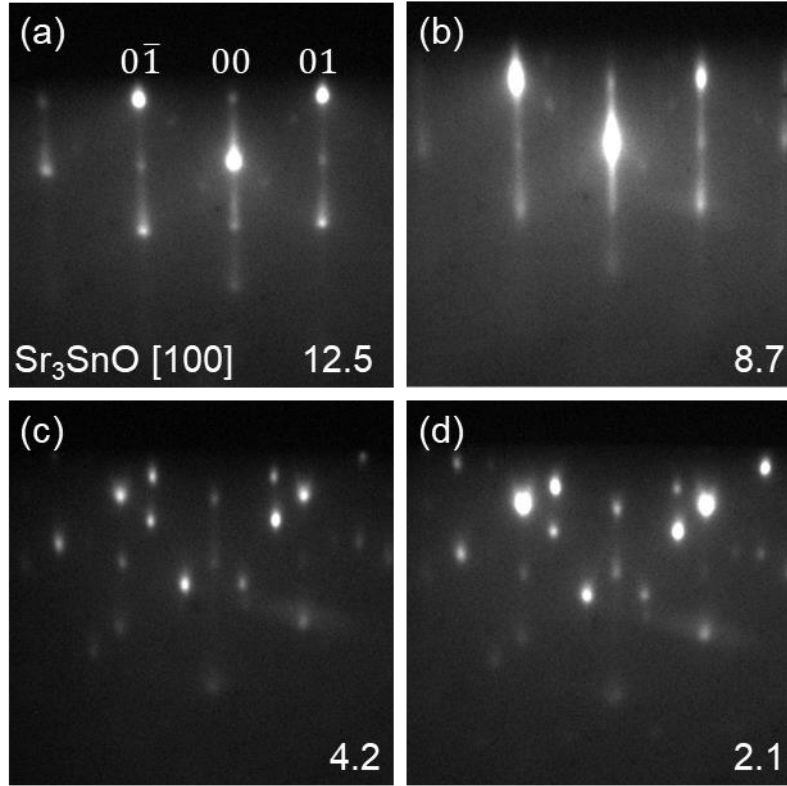
Figure 3-1: RHEED patterns of four Sr_3SnO thin films grown with Sr/SnO_x BEP ratios of 12.5, 8.7, 4.2, and 2.1, respectively. The reflection direction is Sr_3SnO [100]. The figure is reprinted from Appl. Phys. Lett. **119**, 161903 (2021), with the permission of AIP Publishing.
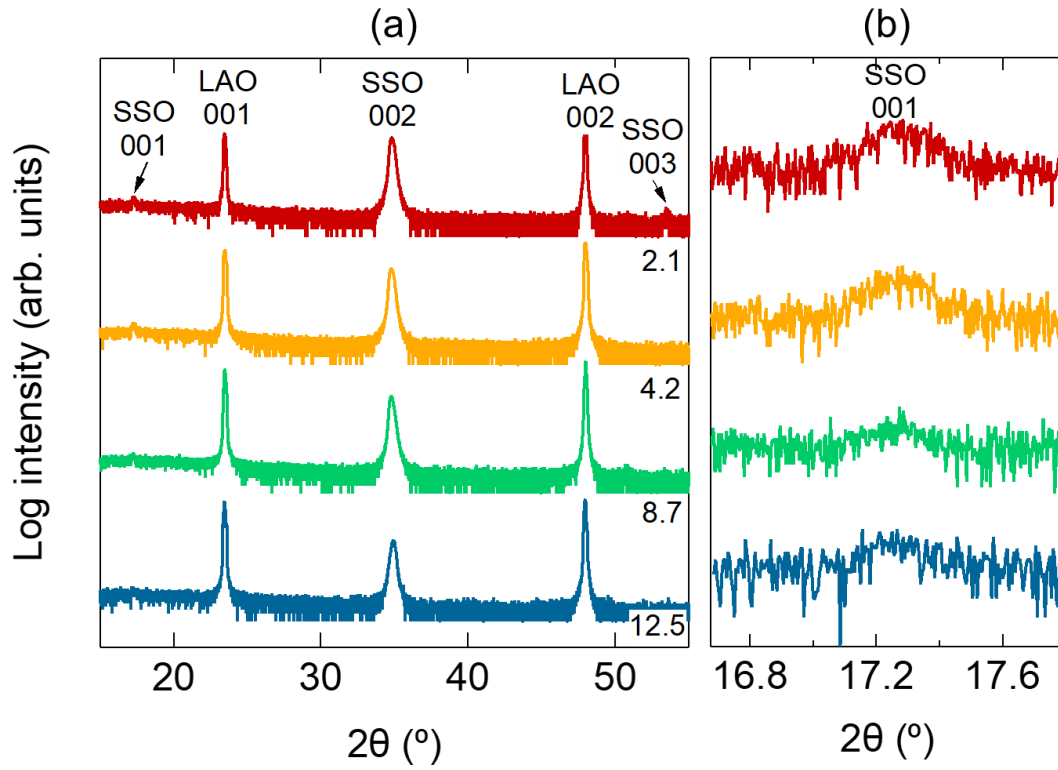
Figure 3-2: (a) Wide angle $2\theta\text{-}\omega$ XRD scans for four Sr_3SnO thin films grown with Sr/SnO_x

BEP ratios of 12.5, 8.7, 4.2, and 2.1, respectively. (b)High-resolution XRD $2\theta\text{-}\omega$ scan around

the 001 Sr_3SnO reflection. The figure is reprinted from Appl. Phys. Lett. **119**, 161903 (2021),

with the permission of AIP Publishing.
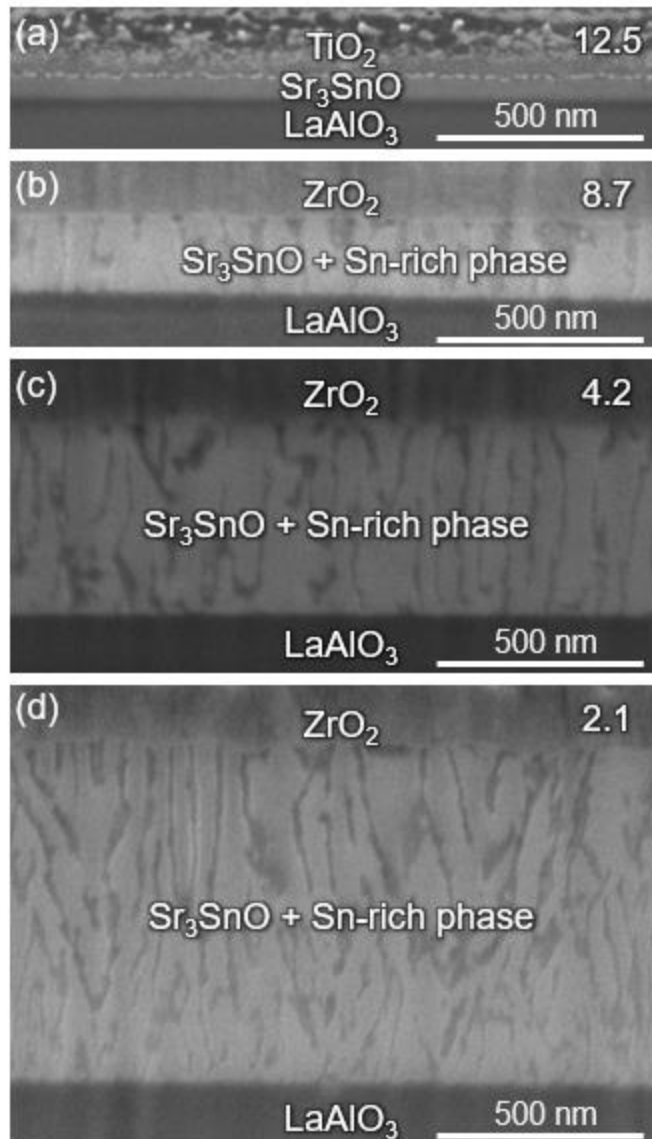
Figure 3-3: Cross-sectional SEM images of Sr_3SnO films grown with Sr/SnO_x BEP ratios of (a) 12.5, (b) 8.7, (c) 4.2, and (d) 2.1. The films are capped by either (a) TiO_2 or (b) to (d) ZrO_2 to prevent degradation in the air. The figure is reprinted from Appl. Phys. Lett. **119**, 161903 (2021), with the permission of AIP Publishing.
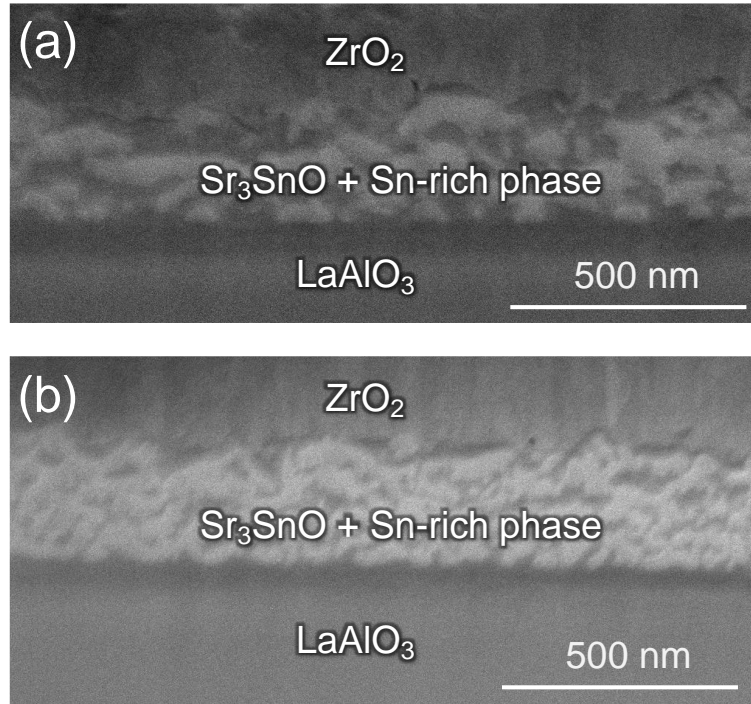
Figure 3-4: Cross-sectional SEM images of Sr_3SnO films growth with the SnO_x/Sr BEP ratios of (a) 2.0 and (b) 1.5. The films are capped by ZrO_2 to prevent degradation in the air. The figure is reprinted from Appl. Phys. Lett. **119**, 161903 (2021), with the permission of AIP Publishing.
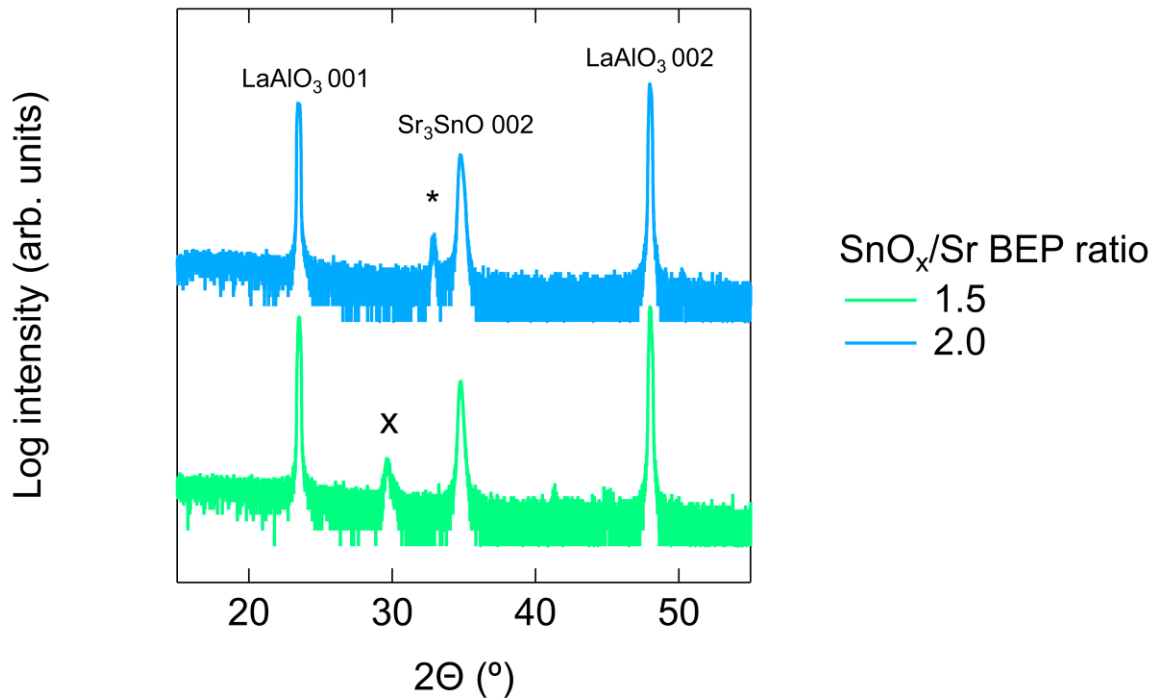
Figure 3-5: Wide-angle XRD 2θ-ω scan of Sr_3SnO films grown the SnO_x/Sr BEP ratio of 1.5 and 2.0, respectively. reflections labeled by asterisk and *x* are due to Sn-rich impurity phases. The figure is reprinted from Appl. Phys. Lett. **119**, 161903 (2021), with the permission of AIP Publishing.
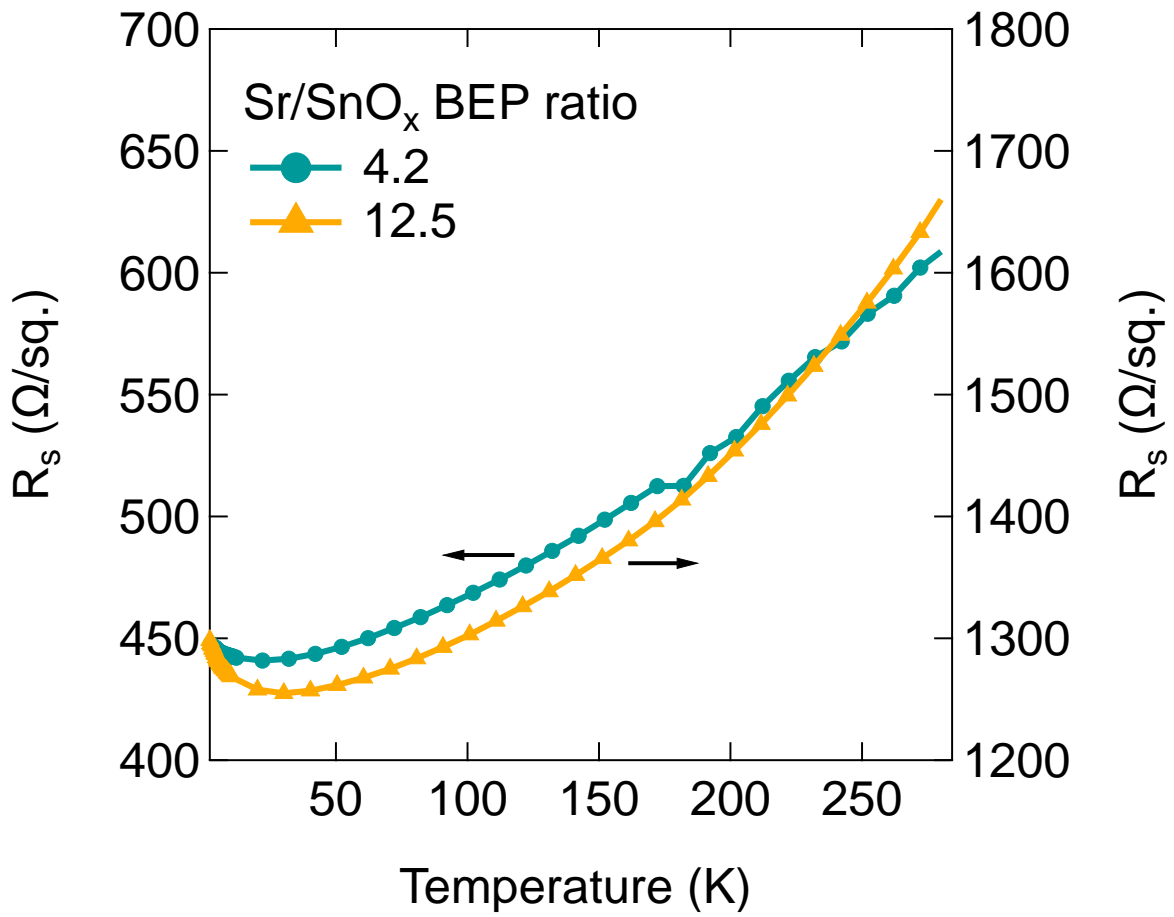
Figure 3-6: Sheet resistance as a function of temperature between 2 K and 280 K for two Sr$_3$SnO films grown with the Sr/SnO$_x$ BEP ratios of 12.5 and 4.2, respectively. The figure is reprinted from Appl. Phys. Lett. **119**, 161903 (2021), with the permission of AIP Publishing.
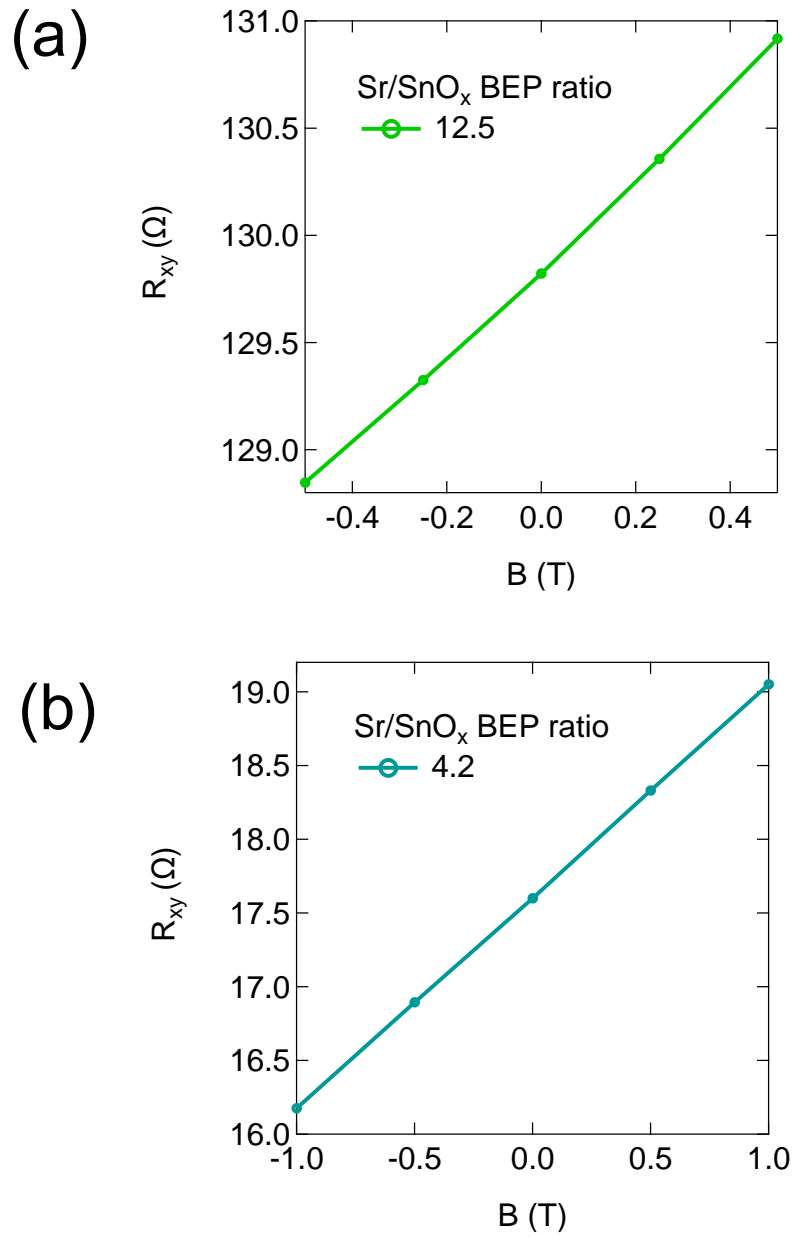
Figure 3-7: Hall effect for two Sr_3SnO films grown with the Sr/SnO_x BEP ratios of 12.5 and 4.2, respectively. The lines show the linear fits of R_{xy} as a function of magnetic field. The figure is reprinted from Appl. Phys. Lett. **119**, 161903 (2021), with the permission of AIP Publishing.
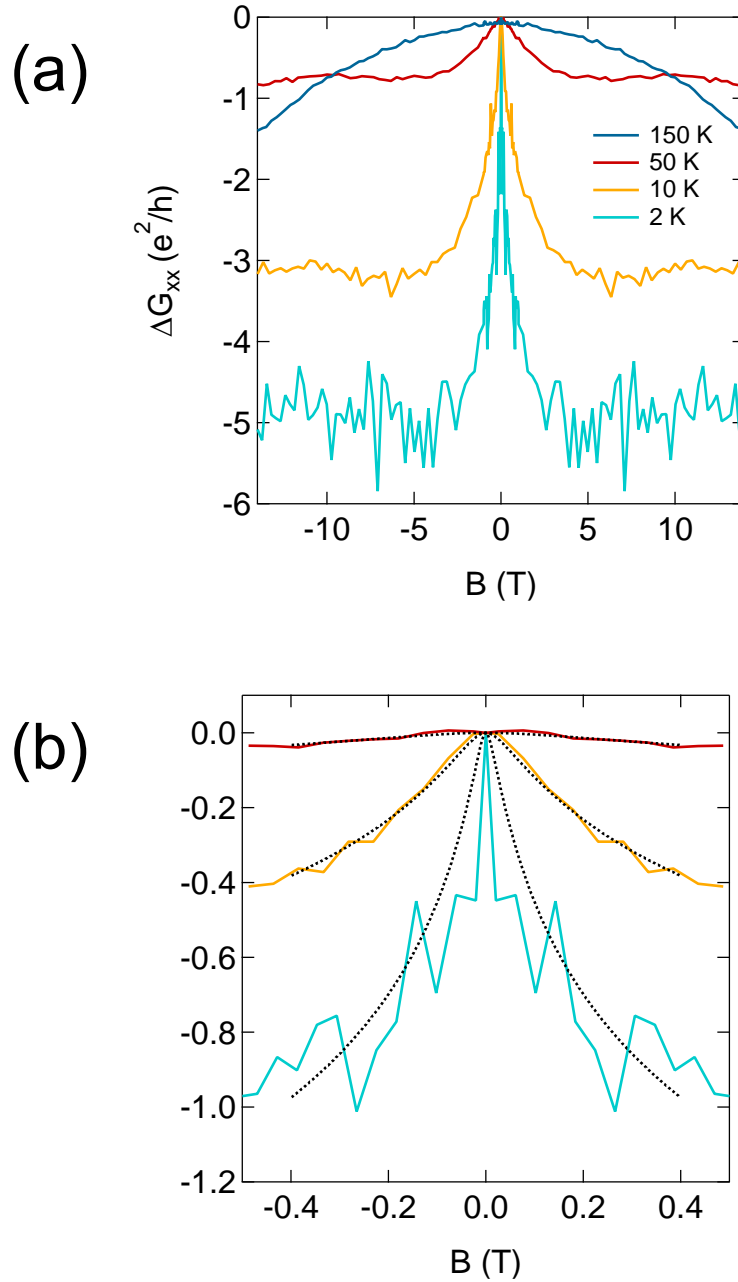
Figure 3-8: (a) Magnetoconductance of a phase-pure Sr$_3$SnO film in the field range of -14 T to 14 T at different temperatures. (b) Hikami-Larkin-Nagaoka fit for weak antilocalization between -0.4 to 0.4 T. The extracted phase coherence lengths are 44 nm, 87 nm, and 146 nm, at 50 K, 10 K, and 2 K, respectively. The data is symmetrized. The figure is reprinted from Appl. Phys. Lett. **119**, 161903 (2021), with the permission of AIP Publishing.
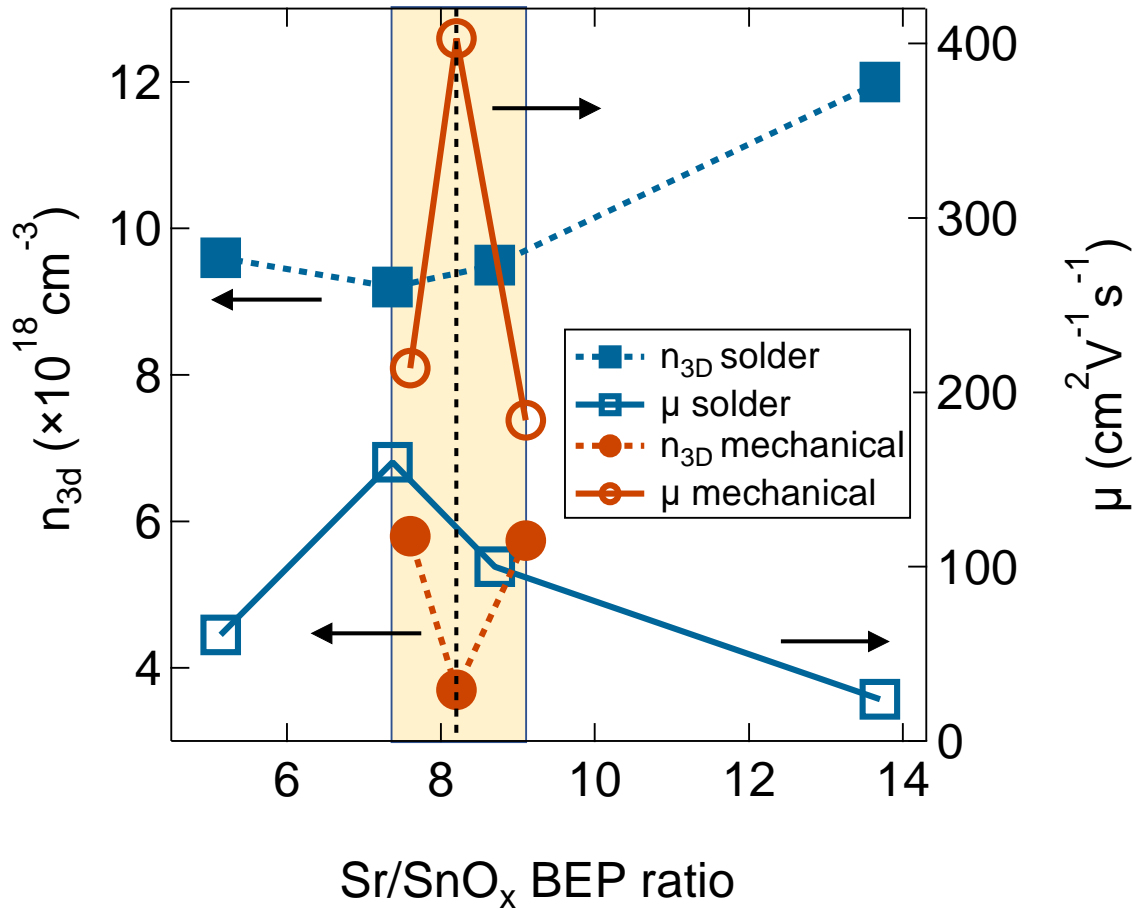
Figure 3-9: Carrier density and mobility as a function of Sr/SnO$_x$ BEP ratios for two series of Sr$_3$SnO films. The two series of films differ in electrical contacts making method, of which one has contacts made by soldering and the other by mechanical pressing. The yellow-shaded region indicates the phase pure growth window. Figure reprinted from Appl. Phys. Lett. **121**, 233101 (2022), with the permission of AIP Publishing.
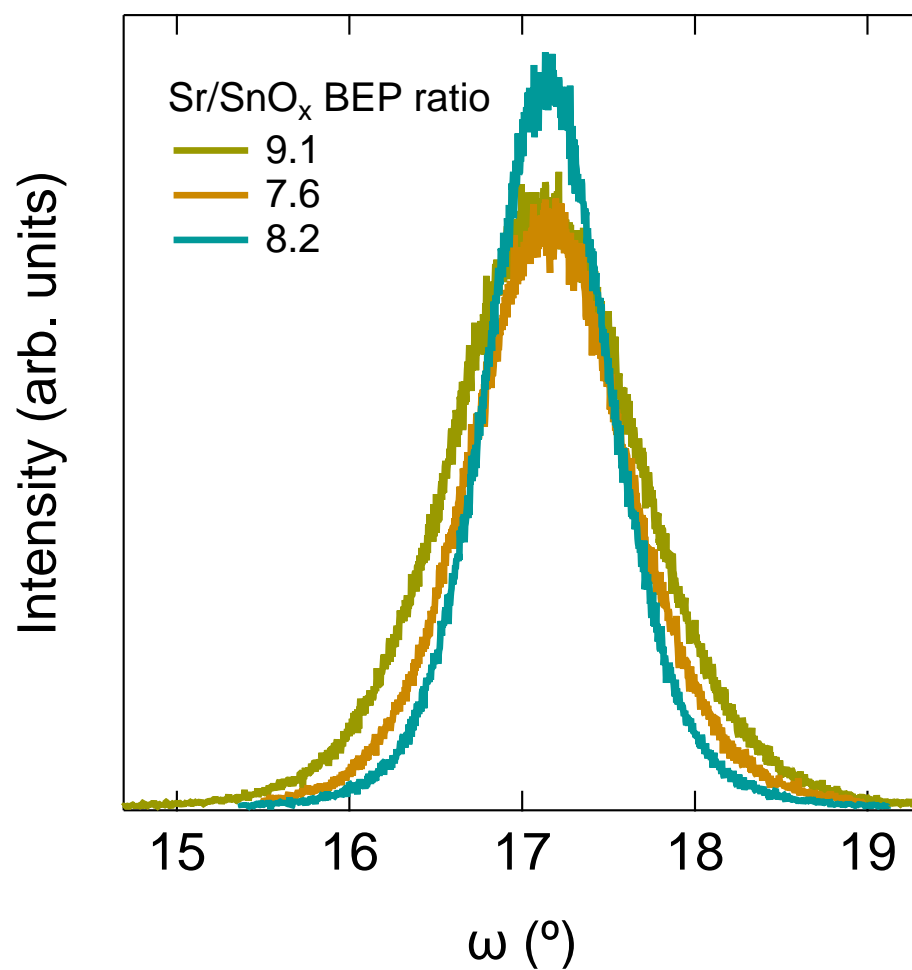
Figure 3-10: XRD ω scans of Sr_3SnO films grown with Sr/SnO_x BEP ratios of 7.6, 8.2, and 9.1. Figure reprinted from Appl. Phys. Lett. **121**, 233101 (2022), with the permission of AIP Publishing.
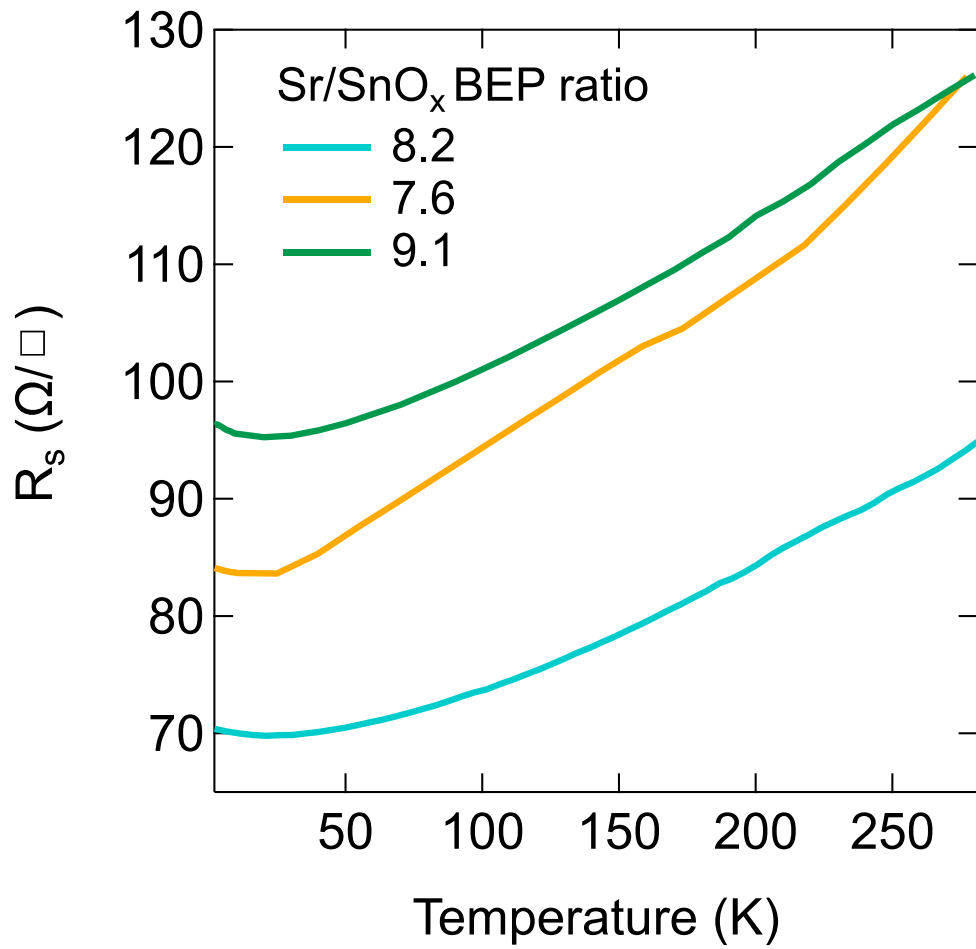
Figure 3-11: Sheet resistance as a function of temperature between 280 and 2 K for Sr_3SnO films grown with Sr/SnO_x BEP ratios of 8.2, 7.6, and 9.2, respectively. The data is measured by using the mechanical method to make electrical contacts. Figure reprinted from Appl. Phys. Lett. **121**, 233101 (2022), with the permission of AIP Publishing.

Chapter 4 Tuning carrier density in phase-pure Sr$_3$SnO antiperovskite thin films

The main result from Chapter 3 is that the stoichiometric control of Sr_3SnO antiperovskite thin films can be achieved in molecular beam epitaxy (MBE) by varying the flux ratios of the source materials. The resulting best film has a respectable carrier mobility of $400 \text{ cm}^2\text{V}^{-1}\text{s}^{-1}$ at 10 K but is not superconducting. One possible reason is that the hole doping densities in phase-pure thin films are below 10^{19} cm^{-3}, two to three magnitudes lower than in the superconductive $Sr_{3-x}SnO$ bulk polycrystalline ceramics [43-46]. Therefore, before claiming that the superconductivity in bulk $Sr_{3-x}SnO$ crystals is extrinsic (i.e. from impurities), the transport behavior of a phase-pure Sr_3SnO thin film with higher hole carrier density should be explored. This cannot be achieved by using more Sn-rich growth conditions to introduce more Sr vacancies (which serve as p-type dopants) because it inevitably causes the formation of Sn-rich secondary phases, making the intrinsicality of the results questionable as discussed in Chapter 3. Therefore, an alternative method of introducing p-type carriers into a phase-pure Sr_3SnO thin film is necessary.

A p-type dopant in Sr_3SnO should have similar structure and size as the replaced atom. The dopant needs one less valence electron to make its best chance to serve as a p-type acceptor. Therefore, the position of the dopant in the periodic table should be one column left to the metal elements in Sr_3SnO, and better to be on the same row for comparable structure and sizes. The elements sitting left to Sr are alkali metals that are very unstable as source materials inside MBE, and therefore get excluded from this study. The group-V element on the same row as Sn is In, commonly used in MBE. Ultra-high purity In is commercially available, and the flux chart is well-known. Therefore, in this study, In is chosen to be the possible p-type dopant in Sr_3SnO thin films by substituting the Sn^{4-} on the B-site.

In this Chapter, I show that indium (In) can indeed increase the hole carrier density in a Sr_3SnO thin film to be above 10^{21} cm^{-3}. The film is however not superconducting. An interesting change in the temperature dependence of sheet resistance, R_s, caused by the increase of hole carriers is discussed in section 4.2. An observation of superconductivity in partially degraded Sr_3SnO thin films is shown in section 4.3.

The figures in this chapter are reprinted from Appl. Phys. Lett. **121**, 233101 (2022), with the permission of AIP Publishing.

4.1 Carrier density and mobility tuned by In dopant

After In was chosen as the dopant material, an effusion cell with high-purity In (7N, United Mineral Corp) was loaded to the oxide MBE (Veeco, GEN 930) used for Sr_3SnO thin film growth (see Chapter 2 for a detailed introduction). The Sr/SnO$_x$ flux ratio used for this study was 8.2, and the films were grown to be 400 nm.

Figure 4-1 (a) shows the carrier density as a function of the In effusion cell temperature. The carriers in all In-doped Sr_3SnO films are p-type (see Hall effect in Figure 4-2), indicating that In^{5-} dopants indeed replace the Sn^{4-} ions on the B-site. No other carriers are found, given that no nonlinearity is seen in Hall effect (to 9 T, not shown here). The p-type carrier density increases exponentially with the In effusion cell temperature (therefore, it linearly increases with the In beam flux), indicating that In atoms are incorporated and activated as acceptors. Figure 4-1 (a) also shows that the In cell temperature can be used to finely control carrier density in Sr_3SnO films. Figure 4-1 (b) illustrates that carrier mobility at 10 K decreases with the increase of carrier density (mobility values are extracted from Hall effect (Figure 4-2) and sheet resistance (Figure 4-3)). At low temperatures, phonon scattering is significantly

prohibited due to the reduced number of phonons, so the scattering is dominated by defects. Therefore, the decrease in the carrier mobility shown in Figure 4-1 (b) is most probably due to the scattering from the ionized In dopants. Importantly, the highest carrier density of the Sr_3SnO film is up to 1.5×10^{21} cm^{-3}, on the same order of magnitude as that of the polycrystalline Sr_3SnO bulk crystals reported to have superconductivity [43-46]. However, none of the films in this study is found to be superconductive, suggesting that Sr_3SnO is probably not an intrinsic superconductor.

4.2 Effect of carrier density on the temperature dependence of sheet resistance

Despite the disappointment of not finding superconductivity in the doped Sr_3SnO films, two interesting behaviors of the temperature dependence of the sheet resistance are observed. As shown in Figure 4-3, with increasing hole carrier density, the localization behavior at low temperatures becomes less pronounced and the temperature dependence at higher temperatures becomes more linear.

This can be seen in the more quantitative analysis in Figure 4-4, where dR_s/dT is taken and fitted into the power law ($\rho \propto T^n$). The fact that the negative dR_s/dT below 20 K disappears in the films grown with In temperature above 800 °C indicates that the more carriers screen the localization correction (also expected, as discussed elsewhere [76]). The temperature dependence of the resistance at an intermediate temperature range (about 80 K to 200 K) changes across the films in Figure 4-4 and becomes almost linear in the film with the highest carrier density.

Figure 4-5 shows that the extracted power n in the intermediate temperature range reduces from 1.8 to 1.0 with the increase of carrier density from 4.5×10^{18} to 1.5×10^{21} cm^{-3}.

One possible explanation is that at higher carrier densities, Sr_3SnO becomes more similar to a Bloch-Grüneisen metal. The temperature dependence of a Bloch-Grüneisen metal is linear at temperatures higher than the Debye temperature (θ_D), when the number of phonons scales linearly with increased temperature [77]. However, the theoretically calculated θ_D for Sr_3SnO is 276 K [78], higher than the temperature range where the linearity is observed. This is possibly because θ_D is reduced in Sr_3SnO thin films, similar to the cases in metals with reduced dimensions [79-81]. The other possible explanation of the trend is through the band structure of Sr_3SnO. As reported [82], there are multiple band maxima at the Γ point. When more carriers lower the Fermi level of Sr_3SnO, it likely gets close to these band maxima, and then changes the power law dependence. Similar phenomena have been seen in Sr_2RuO_4 (n reduces from 3 to 1.5) and cuprate (n becomes 1) when their Fermi level reaches the vicinity of Van Hove singularity [83, 84].

4.3 Observation of superconductivity in partially degraded Sr_3SnO films

Before the application of the mechanical attachment (shown in Figure 2-5), soldering inside N_2 glove box was used to make the electrical contacts on the Sr_3SnO films. The soldering work took longer than the mechanical attachment method, and therefore can degrade the films more. The degradation products are Sn and hydroxides [43-46]. We observed that fully degraded films (exposed directly to atmosphere) are tarnished and the formation of the hydroxides is associated with a volume expansion. The resulting products are not conductive. However, soldering inside the glove box typically only leads to partial degradation of the Sr_3SnO films. Of interest is that superconductivity was observed in a few partially degraded films. An example is shown in Figure 4-6. The superconducting transition temperature is ~3.5 K and the critical field is ~100 Oe at 1.75 K, resembling the properties of Sn films grown by

MBE (see supplementary materials of reference [85]). Since Sn is one of the resulting products from degradation, this adds more suspicion to the nature of the observed superconductivity in the polycrystalline Sr_3SnO samples.

4.4 Conclusion

This chapter shows that indium can be used as a p-type dopant in Sr_3SnO antiperovskite. Decent carrier density control can be achieved by varying the indium source temperature. While maintaining the phase purity of Sr_3SnO, the highest carrier density of 1.5×10^{21} cm^{-3} is accomplished. The films at high carrier density are not superconducting, suggesting that reported superconductivity in polycrystalline Sr_3SnO is extrinsic. Almost linear temperature dependence of resistance is observed in the film with the highest carrier density, whose origin requires future investigations.
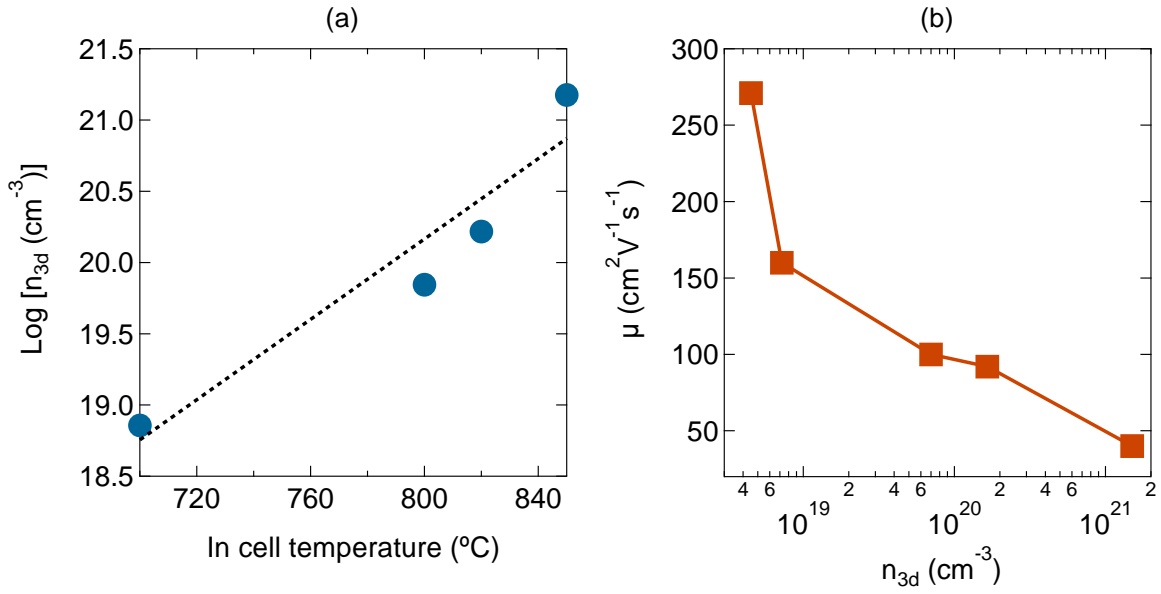
Figure 4-1: (a) Carrier density at 10 K of Sr_3SnO films (with the stoichiometric Sr/SnO_x BEP ratio of 8.2) as a function of indium dopant cell temperature during the MBE growth. The dashed line shows a linear fit. (b) Reduction of carrier mobilities with increase of carrier density at 10 K. The electrical contacts of all the films were made by the mechanical method. Figure reprinted from Appl. Phys. Lett. **121**, 233101 (2022), with the permission of AIP Publishing.
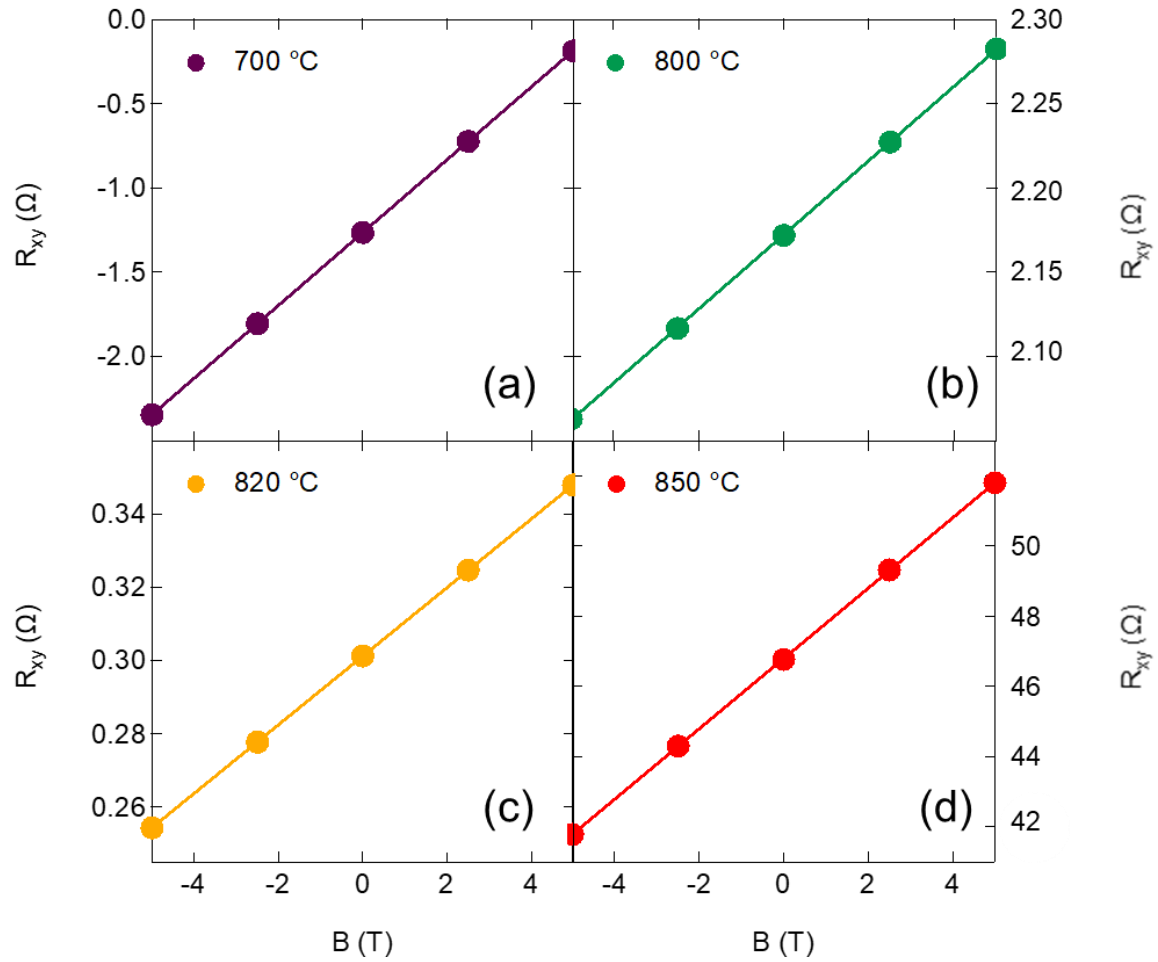
Figure 4-2: Hall effects of four Sr$_3$SnO films grown with the same Sr/SnO$_x$ BEP ratio of 8.2, but with (a) 700 ℃ In, (b) 800 ℃ In, (c) 820 ℃ In, and (d) 850 ℃ In. The measurement temperature is 10 K. The electrical contacts of all the films were made by the mechanical method. Figure reprinted from Appl. Phys. Lett. **121**, 233101 (2022), with the permission of AIP Publishing.
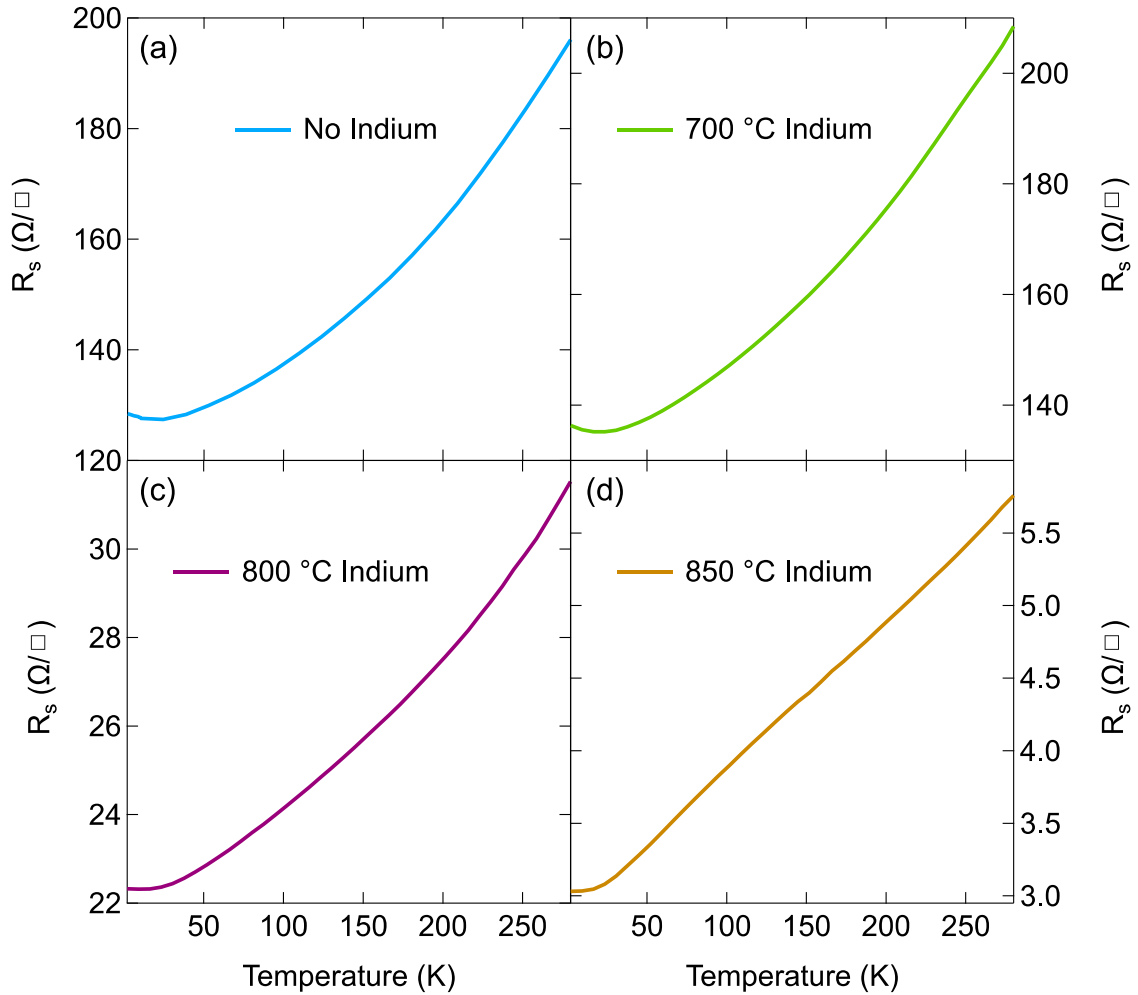
Figure 4-3: Sheet resistance measured between 280 and 2 K of four In doped Sr$_3$SnO films grown with the same Sr/SnO$_x$ BEP ratio of 8.2 but with different In temperatures as (a) no In, (b) 700 °C, (c) 800 °C, and (d) 850 °C. The electrical contacts of all the films were made by the mechanical method. Figure reprinted from Appl. Phys. Lett. **121**, 233101 (2022), with the permission of AIP Publishing.
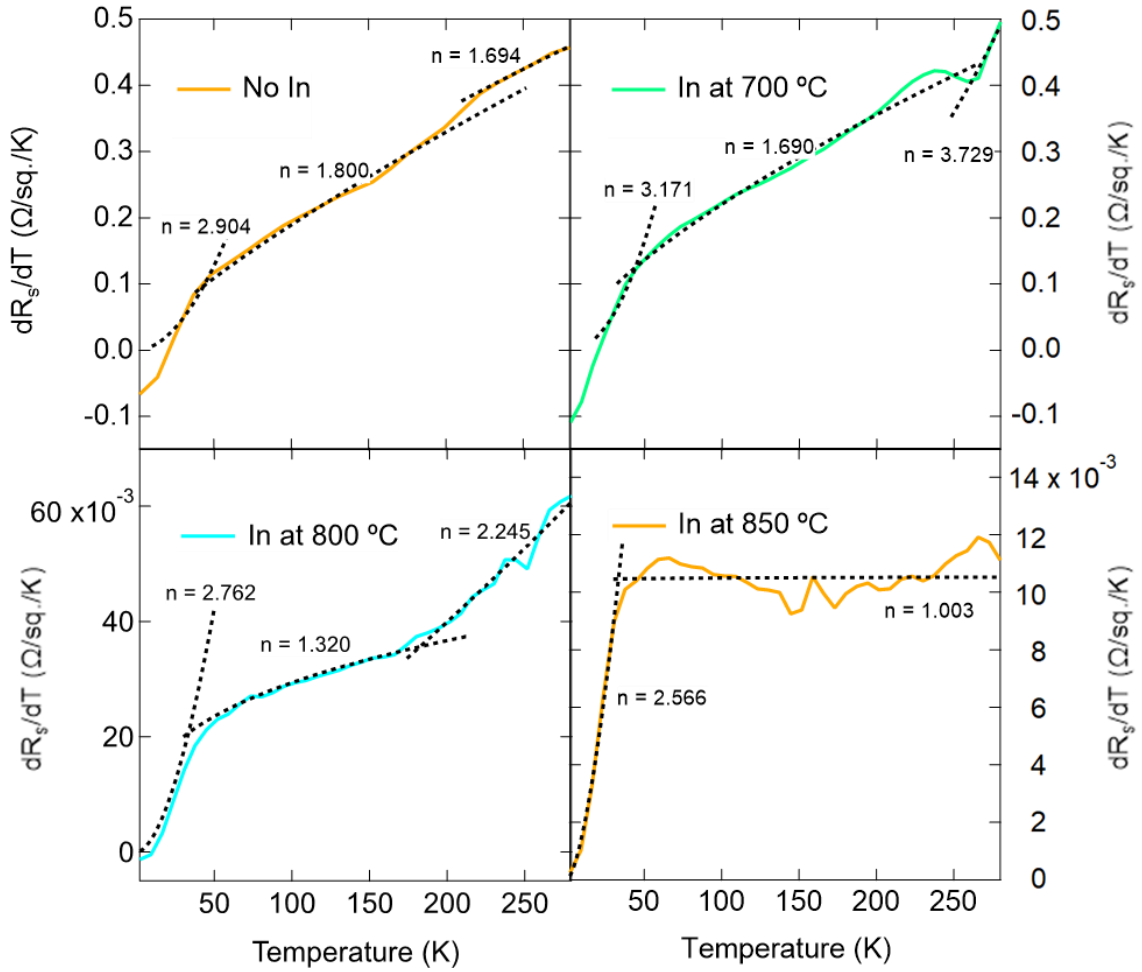
Figure 4-4: Temperature derivative of sheet resistance between 280 and 2 K of four In doped Sr₃SnO films grown with the same Sr/SnOₓ BEP ratio of 8.2 but different In temperatures as (a) no In, (b) 700 ℃, (c) 800 ℃, (d) 850 ℃ In. Dashed lines show the power law fit ($\rho \propto T^n$), and *n* is labelled in different regimes. The electrical contacts of all the films were made by the mechanical method. Figure reprinted from Appl. Phys. Lett. **121**, 233101 (2022), with the permission of AIP Publishing.
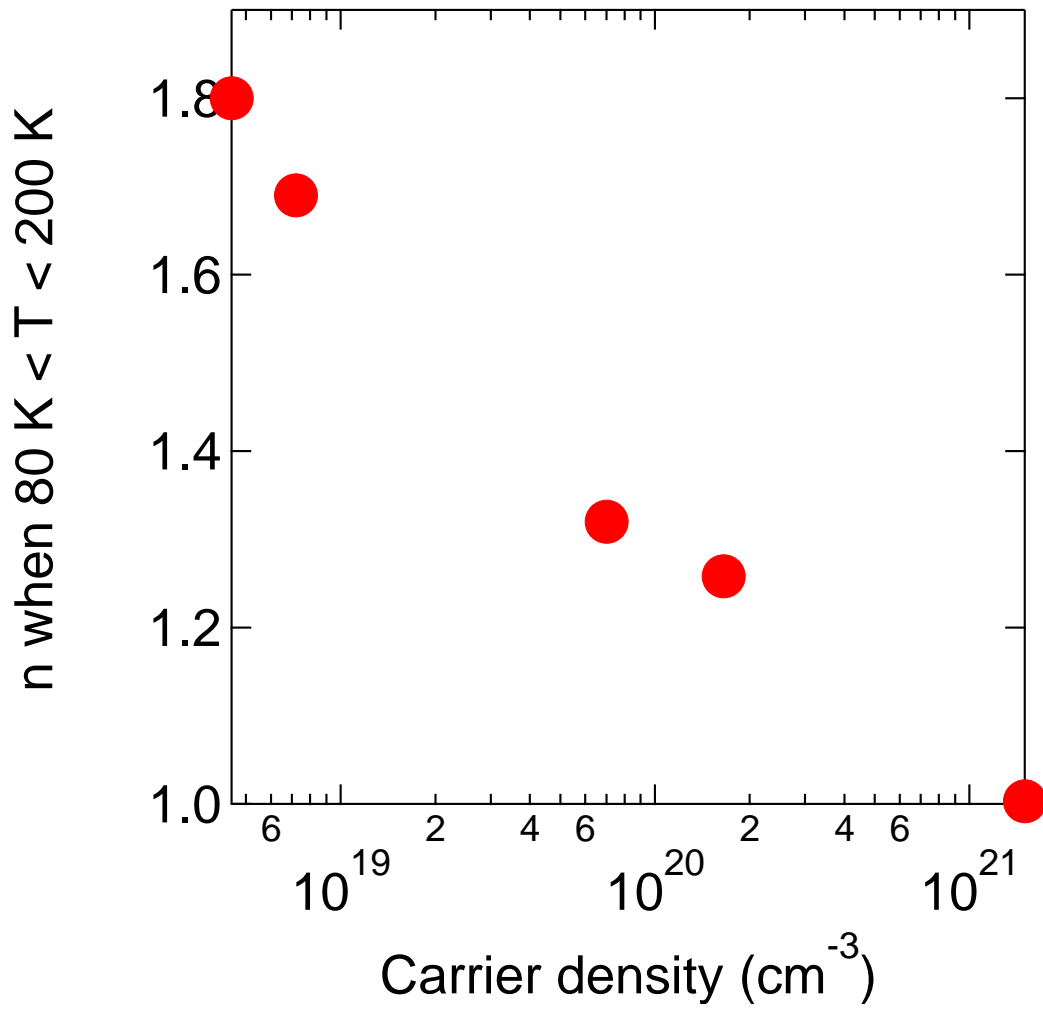
Figure 4-5: Extracted n in the intermediate temperature range from the power law fitting ($\rho \propto T^n$) as a function of carrier density. Figure reprinted from Appl. Phys. Lett. **121**, 233101 (2022), with the permission of AIP Publishing.
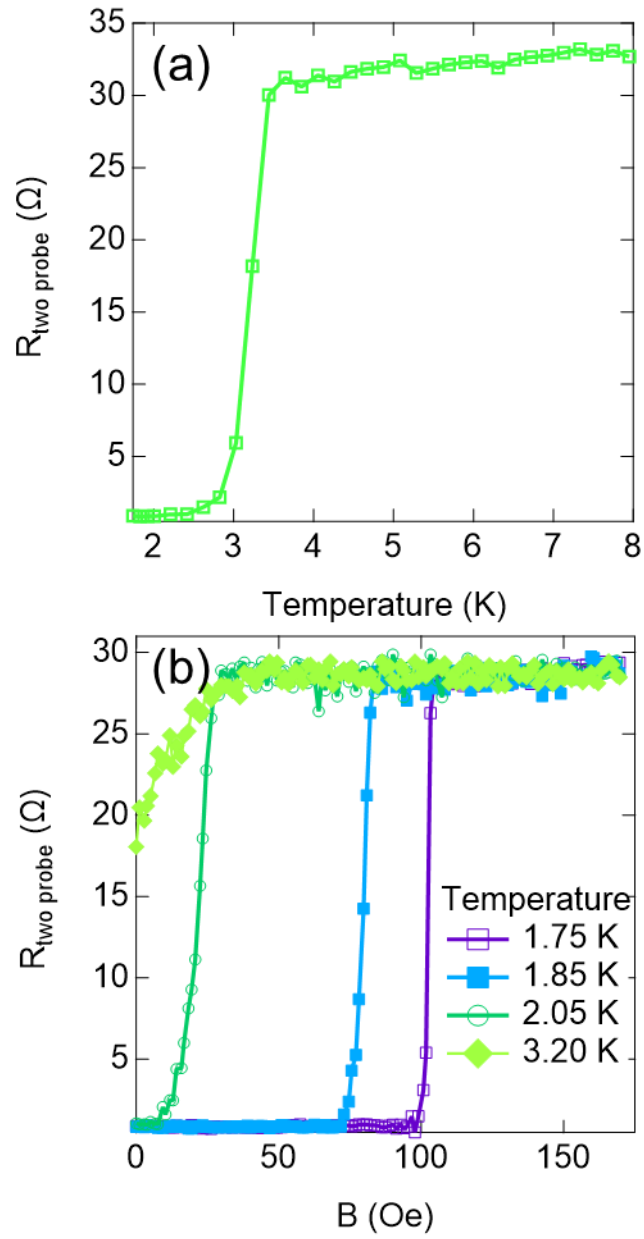
Figure 4-6: Observation of superconductivity in (a) temperature, and (b) magnetic field scan in a partially degraded Sr_3SnO film.

Chapter 5 Molecular beam epitaxy of BaSnO₃ on lattice-matched substrates

As is discussed in Chapter 1, BaSnO$_3$ (100) thin films have much lower carrier mobility values (up to ~180 cm^{2}V^{-1}s^{-1}) than single crystals (~300 cm^{2}V^{-1}s^{-1}) at room temperature. One likely defect limiting the mobility in BaSnO$_3$ thin films are threading dislocations. Threading dislocations in thin films originate from strain-relaxation of the lattice mismatch between the BaSnO$_3$ thin film and the substrate. In this Chapter, the connection between threading dislocations and reduced carrier mobility in BaSnO$_3$ thin films is investigated by growing the films on lattice-matched substrates, which should suppress the formation of these defects.

Figure 5-1 shows the lattice constants of BaSnO$_3$ and commercially available substrates commonly used for perovskite growth; most of these substrates have more than 1% mismatch with BaSnO$_3$, as SrZrO$_3$ and BaSnO$_3$ are not widely commercially available. Fortunately, a vendor was convinced to synthesize SrZrO$_3$ substrates, and the J. W. Kolis group at Clemson University managed to grow BaSnO$_3$ substrates for this project [86]. The lattice constant of both of these substrates match that of BaSnO$_3$ within 1%. The qualities of the SrZrO$_3$ (100) and BaSnO$_3$ (100) substrates are briefly discussed in section 5.1. Notably, the Bravais lattice of SrZrO$_3$ is orthorhombic, and it is the pseudo-cubic lattice that is matched with that of BaSnO$_3$. Thus, on the SrZrO$_3$ (100) substrate, the growth direction for BaSnO$_3$ is [110]. As is introduced in Chapter 1, the previous work at UCSB and in the literature all have studied BaSnO$_3$ thin films grown along [100] direction. Therefore, to ensure that the different growth direction does not influence the transport behavior, a comparison of BaSnO$_3$ thin film growths on SrTiO$_3$ (100) and (110) substrates is discussed in Section 5.2.

The methodology of the molecular beam epitaxy of BaSnO$_3$ thin films have been discussed in Chapter 2. In this Chapter, the SrZrO$_3$ (100) substrates have a size of 3×3 mm. Therefore, the growth and measurement methods for small sized samples discussed in Section

2.3 are applied. The growth conditions in terms of substrate temperature (850 °C) and SnO_x/Ba

beam equivalent pressure ratio (~25) were pre-calibrated using a $DyScO_3$ (110) substrate. All

the growths were performed under 1×10^{-5} torr oxygen plasma. The resulting $BaSnO_3$ growths

on $SrZrO_3$ (100) and $BaSnO_3$ (100) substrates are discussed in Sections 5.3 and 5.4,

respectively.

5.1 Evaluation of the $SrZrO_3$ (100) and $BaSnO_3$ (100) substrate

Figure 5-2 shows x-ray diffraction (XRD) ω scan for a $SrZrO_3$ (100) substrate near the

$SrZrO_3$ 100 peak. As can be seen, the reflection is very broad and splits into many sub-peaks.

This indicates poor crystallinity and large mosaicity in the substrate. This could affect the

crystalline quality of the $BaSnO_3$ film because the epitaxy depends on the substrate lattice as

the template.

The reflection high-energy electron diffraction (RHEED) pattern of the $SrZrO_3$ (100)

substrate shown in Figure 5-3 (a) confirms the poor crystallinity, as the reflection pattern is

highly diffusive. However, the pattern is not spotty, indicating that the surface is not rough (i.e.

does not have three-dimensional islands). Figure 5-3 (b) shows an atomic force microscope

(AFM) image of the $SrZrO_3$ (100) substrate. The surface is relatively smooth with no apparent

defects. The average roughness is below 1 nm.

Figure 5-4 shows the XRD ω scan for a $BaSnO_3$ (100) substrate near its 100 reflection.

Compared to Figure 5-2, this reflection is less broad and not split, with only minor shoulders

near the peak, indicating that the $BaSnO_3$ (100) substrate has a higher crystallinity and less

mosaicity than the $SrZrO_3$ substrate.

The RHEED pattern of the BaSnO$_3$ (100) substrate, shown in Figure 5-5 (a), is slightly less diffusive than that of the SrZrO$_3$ (100) substrate. However, it is still worse than that of a typical commercial substrate. For example, Figure 5-6 shows the RHEED pattern of a LaAlO$_3$ substrate. The diffraction pattern has spots aligned with Laue circle and is not diffusive. The BaSnO$_3$ (100) substrate surface (see Figure 5-5 (b) for AFM) is rougher than that of the SrZrO$_3$ (100) substrate, but the roughness is still below 3 nm.

In summary, the SrZrO$_3$ (100) and BaSnO$_3$ (100) substrates have reasonably smooth surfaces for MBE growth. Their crystalline qualities are poorer than commonly used commercial substrates, which may negatively impact the structure of the BaSnO$_3$ thin film grown on them. Therefore, it will be necessary to use transmission electron microscopy (TEM) to ensure the quality of the grown BaSnO$_3$ thin film before reaching any conclusion.

5.2 Comparison of BaSnO$_3$ growth along [100] and [110] directions

As mentioned above, the growth direction of BaSnO$_3$ on the SrZrO$_3$ (100) substrate is expected to be [110]. Therefore, understanding the effect of growing along that direction is essential. Here, the different growth directions are guided by the substrate lattices (SrTiO$_3$ (100) and (110)).

Figure 5-7 shows the RHEED patterns of BaSnO$_3$ grown along [100] and [110] directions, respectively. The BaSnO$_3$ (100) film has a streaky RHEED pattern, indicating a relatively smooth surface without three-dimensional islands. On the other hand, the RHEED for the BaSnO$_3$ (110) film is spotty, indicating the formation of islands.

Figure 5-8 compares the XRD 2θ-ω scans for the two films shown in Figure 5-7. No peak split is observed in both patterns. The only difference is that the Laue thickness fringes

of the BaSnO₃ (100) film are more pronounced than that of the BaSnO₃ (110) film, indicating that the BaSnO₃ (100) film has a smoother surface and interface. This is consistent with RHEED and AFM, shown in Figure 5-9.

Figure 5-10 shows the electron mobility as a function of carrier density for two series of BaSnO₃ films grown along [100] and [110] directions, respectively. The carrier density was tuned by using different La dopant concentrations. As is discussed in Chapter 1, each mobility value has an error bar of order 10 $cm^2V^{-1}s^{-1}$. Therefore, the similar trend of the two series shown in Figure 5-10 indicates that different growth directions do not strongly impact transport behavior, despite the [100] growth direction resulting in better structural quality.

5.3 BaSnO₃ (110) growth on SrZrO₃ (100) substrate

Figure 5-11 (a) shows the RHEED of a BaSnO₃ (110) thin film grown on SrZrO₃ (100) substrate. As expected, the [110] growth direction leads to a spotty pattern due to the formation of islands. Figure 5-11 (b) shows the AFM image of the as-grown BaSnO₃ (110) thin film. Islands appear on the surface. Such islands are commonly observed due to the Sn-rich growth condition and are probably SnO₂ (this phenomenon will be discussed in Chapter 6). Figure 5-12 compares the XRD 2θ-ω scan for the BaSnO₃ (110) thin film grown on the SrZrO₃ (100) substrate and the bare SrZrO₃ (100) substrate, which confirmed that the growth direction is [110].

Figure 5-13 shows a cross-sectional STEM image of a BaSnO₃ (110) film on SrZrO₃ (100) substrate. The interface is sharp and abrupt. No misfit dislocations are seen near the interface, nor are there extended defects, showing a significant improvement over the film

presented in Figure 1-1 (c) and (d). However, the carrier mobility in this film is only 130 cm^{2}V$^-$ ^{1}s^{-1}, which is still well below that reported in BaSnO$_3$ single crystals.

5.4 BaSnO$_3$ (100) growth on BaSnO$_3$ (100) substrate

Figure 5-14 (a) shows the RHEED pattern of a homoepitaxially grown BaSnO$_3$ (100) film. The pattern is not intense but streaky. SnO$_2$ islands are observed in the AFM image (Figure 5-14 (b)). Figure 5-15 compares the XRD 2θ-ω scan for the homoepitaxial structure and the bare BaSnO$_3$ (100) substrate, which confirms the [100] growth direction. The peak, however, tilts toward the higher 2θ angle. This is possibly caused by the non-uniform surface observed in the TEM image shown in Figure 5-16 (a).

Figure 5-16 shows a high-resolution cross-sectional STEM image of the BaSnO$_3$ homoepitaxial structure, where the arrows label the position of the interface. The interface is inclined probably due to polishing issues when the substrate surface was prepared. Defects also exist in the bulk substrate, appearing as bright features in the TEM (Figure 5-16 (a)). Despite these imperfections, the interface looks sharp and free of misfit dislocation. In addition, the high-magnification STEM image in Figure 5-16 (c) shows no extended defects in the BaSnO$_3$ film.

Two homoepitaxial growths were attempted. However, the carrier mobility values are only 50 and 120 cm^{2}V^{-1}s^{-1}, respectively. Therefore, similar to the growth on the SrZrO$_3$ (100) substrate, the carrier mobility does not show improvement despite the absence of threading dislocations.

5.5 Conclusion

Threading dislocations, widely thought to limit electron mobility in $BaSnO_3$ thin films, have been eliminated in the films shown in this Chapter by using lattice-matched substrates. Because the substrate quality is not as high as that of commonly used substrates, the resulting $BaSnO_3$ thin films grown on the lattice-matched substrates also have poorer diffraction and AFM results. However, STEM images show that the $BaSnO_3$ thin films are free of threading dislocations.

The electron mobilities in the dislocation-free films are still within the typical range of that in $BaSnO_3$ thin films containing threading dislocations. This result indicates that other defects, such as point defects, likely dominate in limiting electron mobility. In addition, the poor structural quality of the lattice-matched substrates can extend to the films. This would require working on the substrate quality improvement. Furthermore, due to the limited supply, not enough growths on these lattice-matched substrates were carried out to optimize the stoichiometry. A study of point defects in $BaSnO_3$ thin films is discussed in Chapter 6.
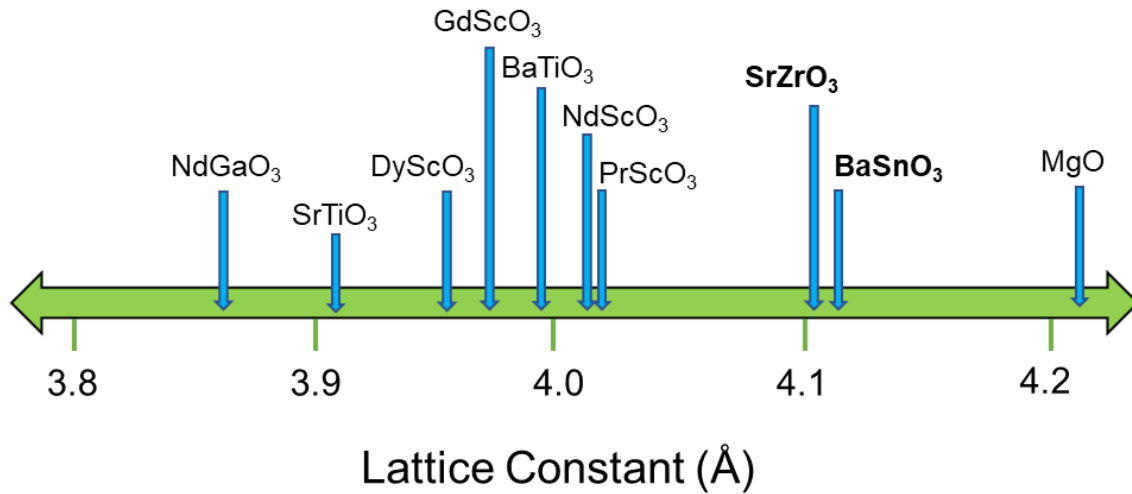
Figure 5-1: Lattice constants of commercially available substrates commonly used for perovskite oxide thin film growth. $SrZrO_3$ and $BaSnO_3$ are used in this study but not widely available.
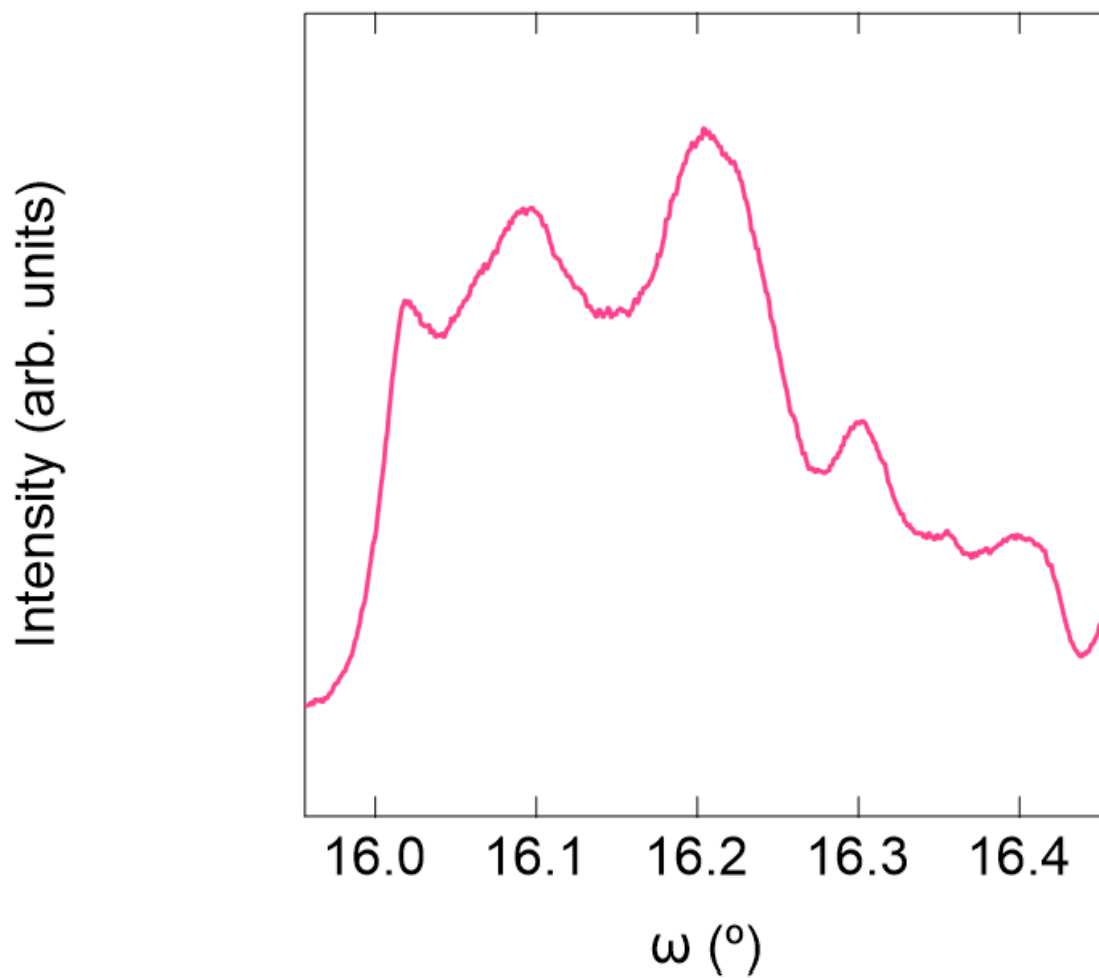
Figure 5-2: XRD ω scan for a SrZrO$_3$ (100) substrate near the SrZrO$_3$ 100 peak.
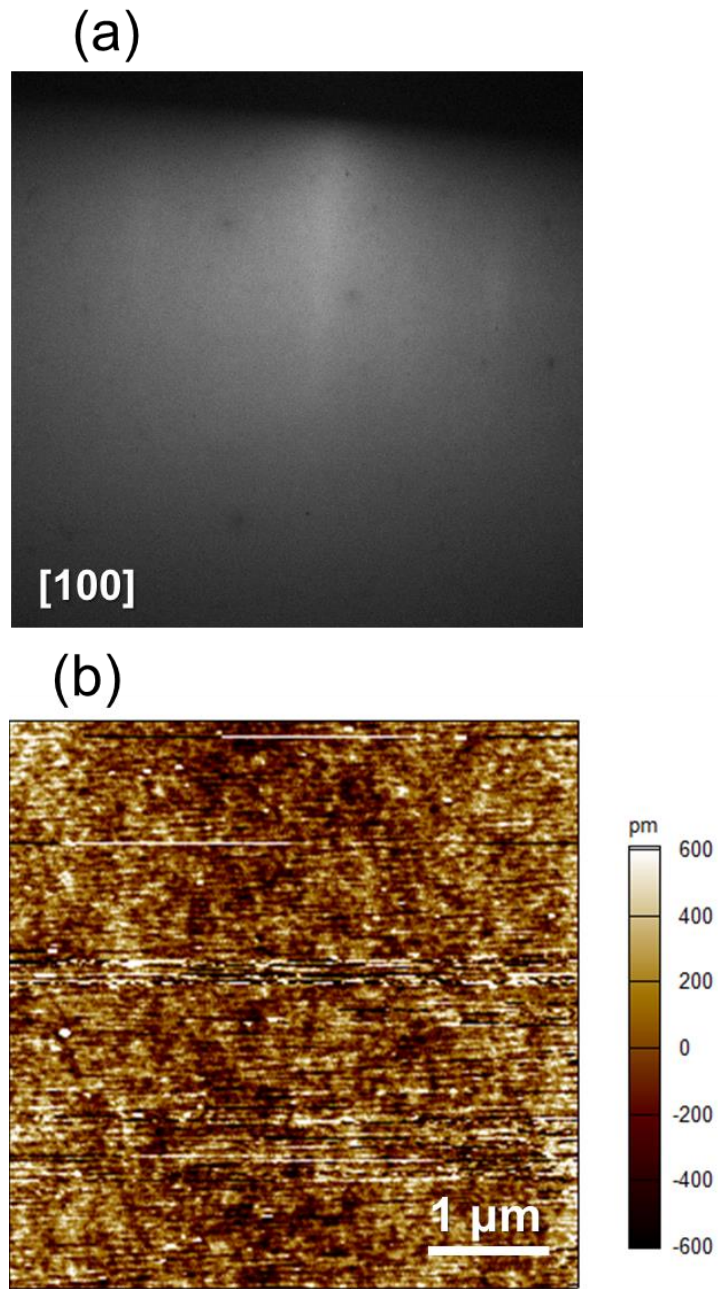
Figure 5-3: (a) RHEED and (b) AFM images of a SrZrO$_3$ substrate.
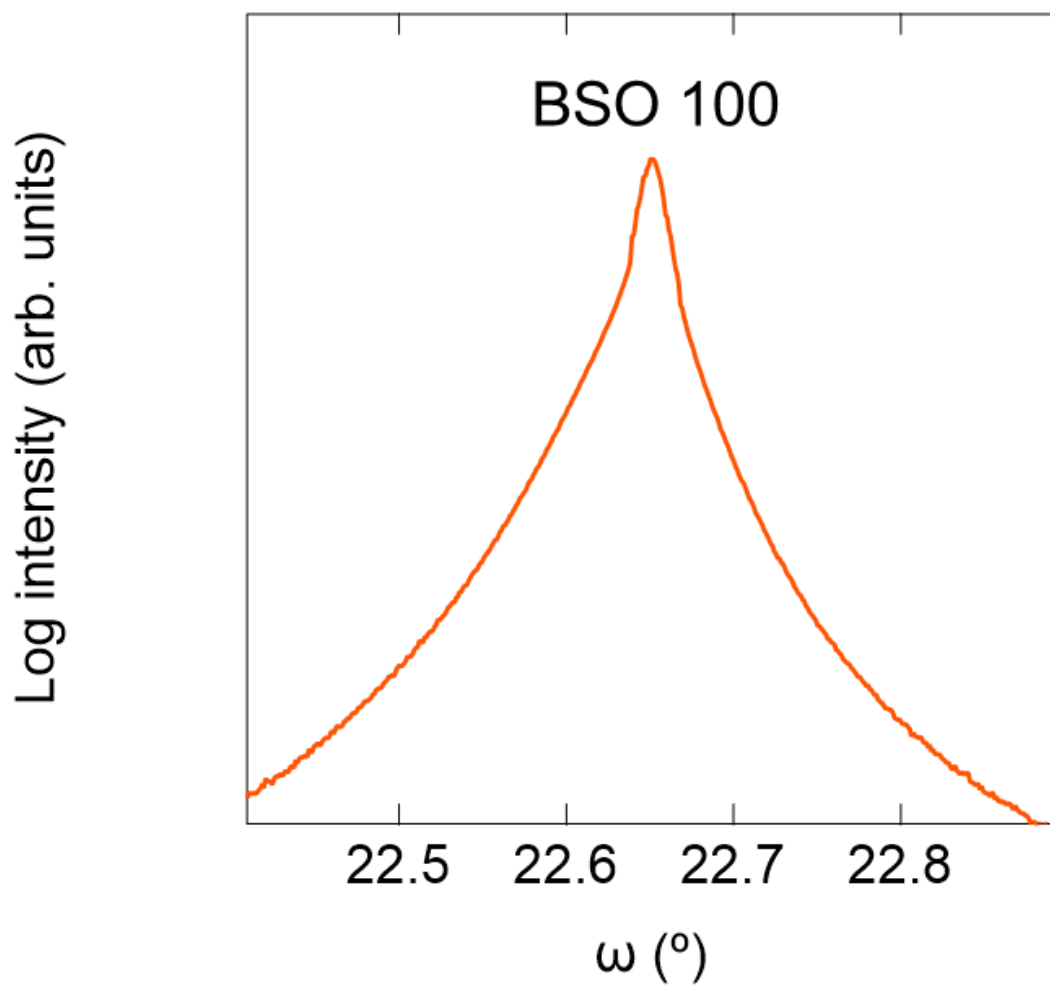
Figure 5-4: XRD ω scan for a BaSnO$_3$ (100) substrate near the BaSnO$_3$ 100 peak.
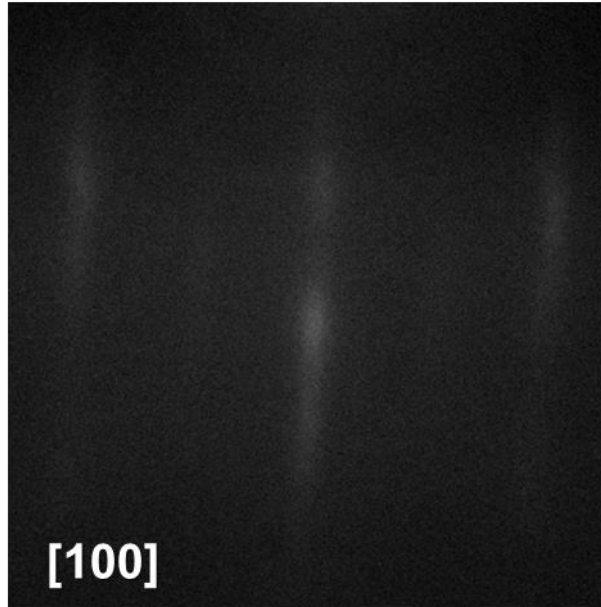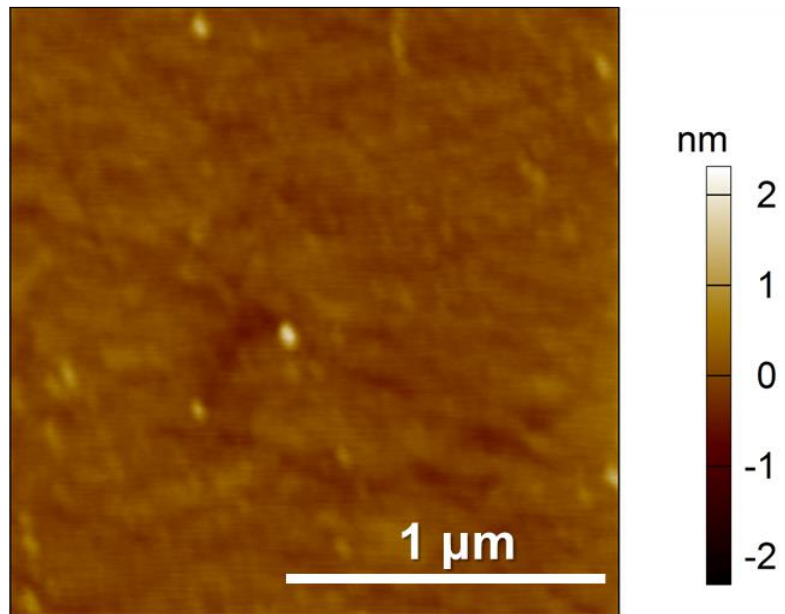
Figure 5-5: (a) RHEED and (b) AFM images of a BaSnO$_3$ substrate.
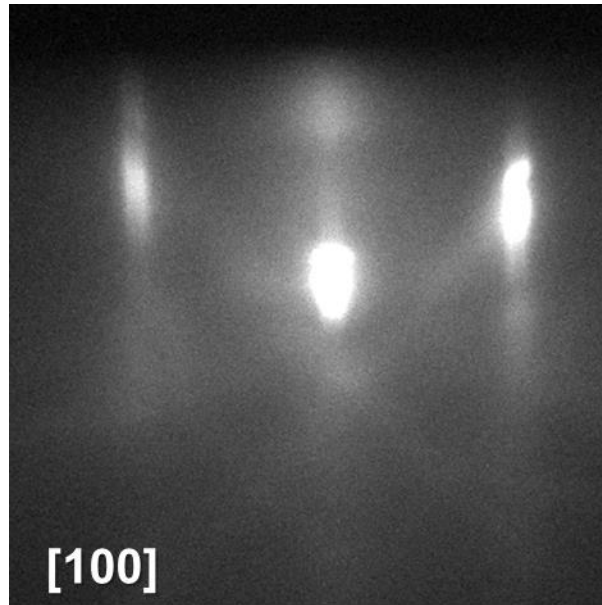
Figure 5-6: RHEED reflection of a commercially available LaAlO$_3$ substrate.
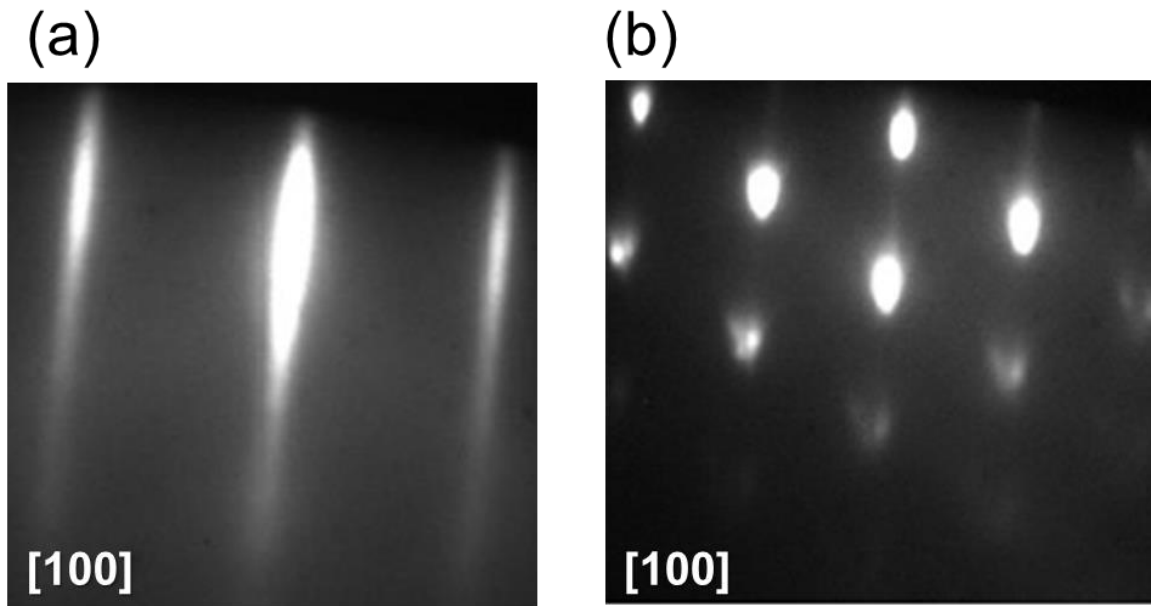
Figure 5-7: RHEED patterns for BaSnO$_3$ thin films grown on (a) SrTiO$_3$ (100) and (b) SrTiO$_3$ (110) substrate.
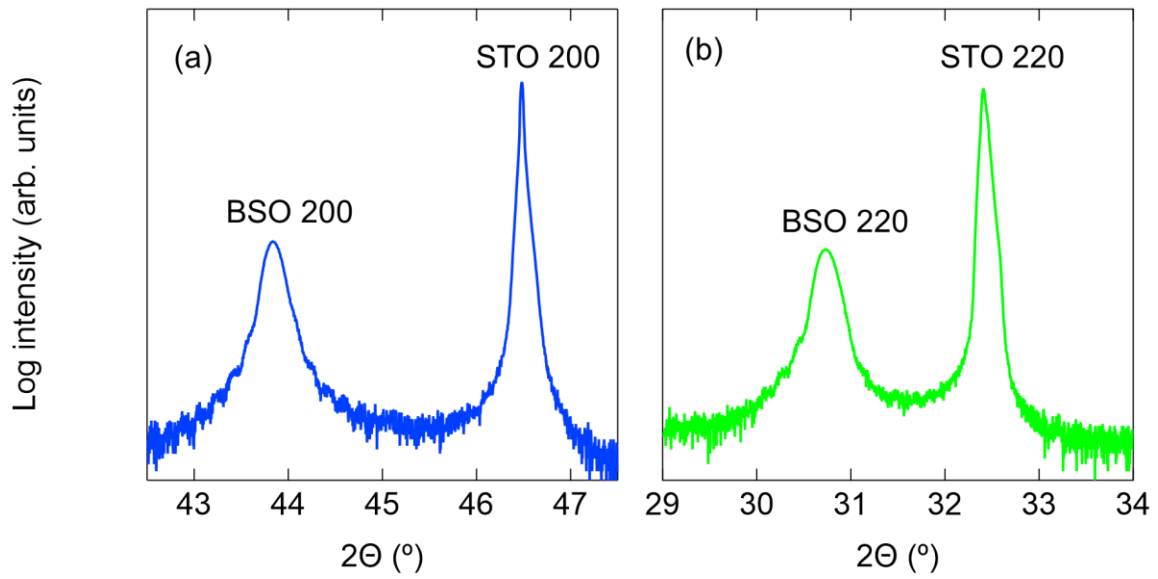
Figure 5-8: XRD $2\theta\text{-}\omega$ scans for BaSnO$_3$ thin films grown on (a) SrTiO$_3$ (100) and (b) SrTiO$_3$ (110) substrate.
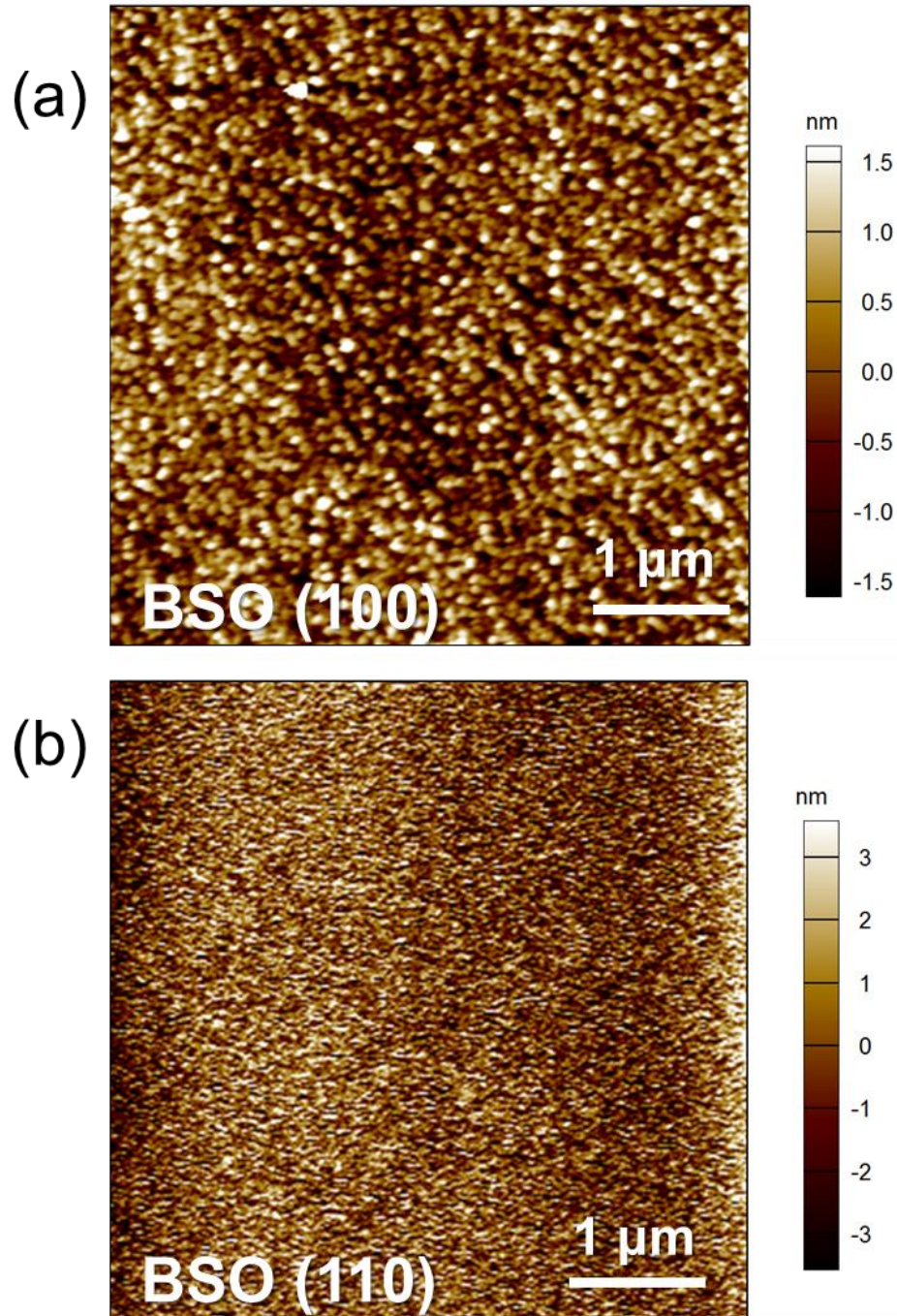
Figure 5-9: AFM images for the surfaces of the BaSnO$_3$ thin films grown on (a) SrTiO$_3$ (100) and (b) SrTiO$_3$ (110) substrate.
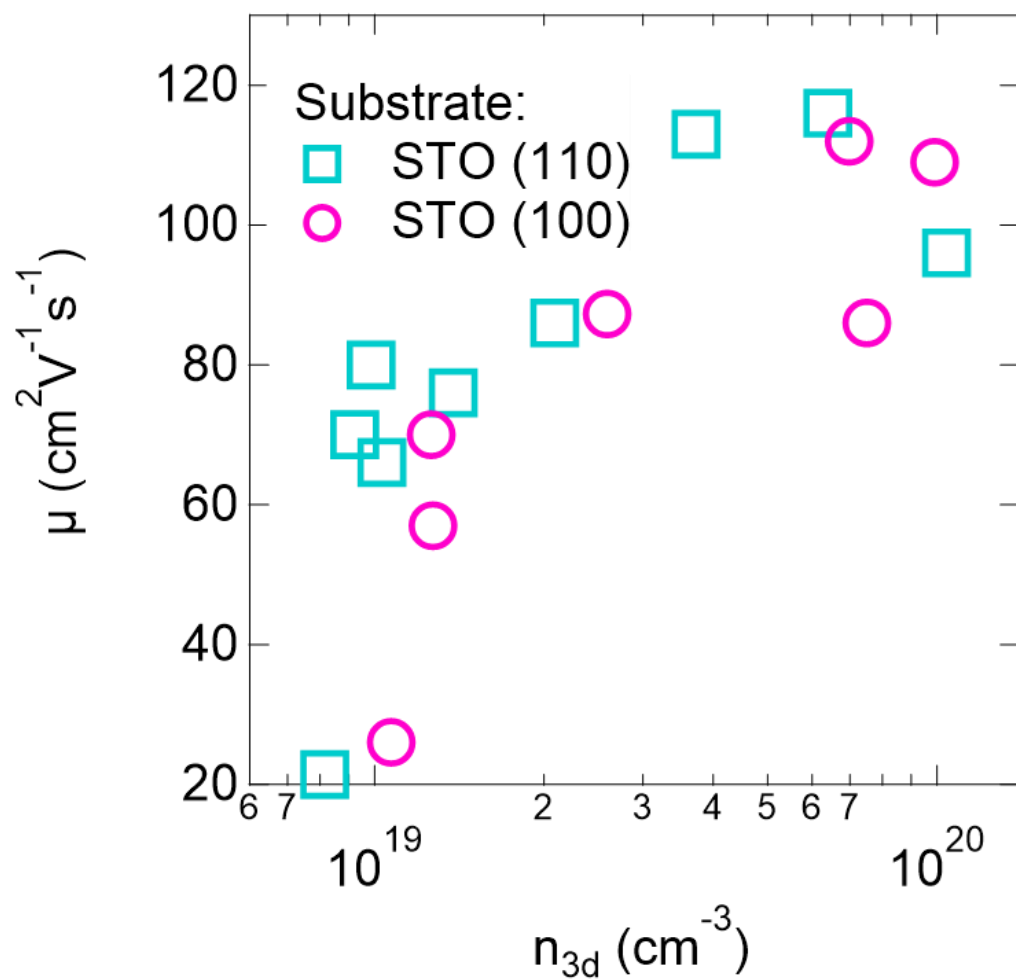
Figure 5-10: Electron mobilities as a function of carrier density for two series of BaSnO₃ films grown along [100] and [110] directions, respectively.
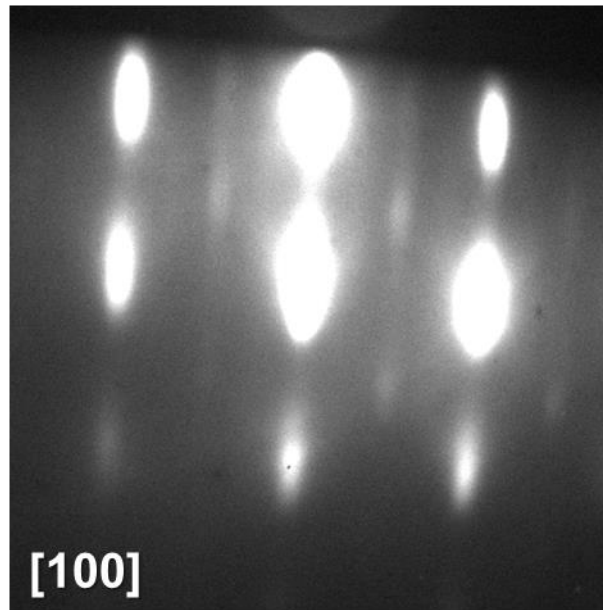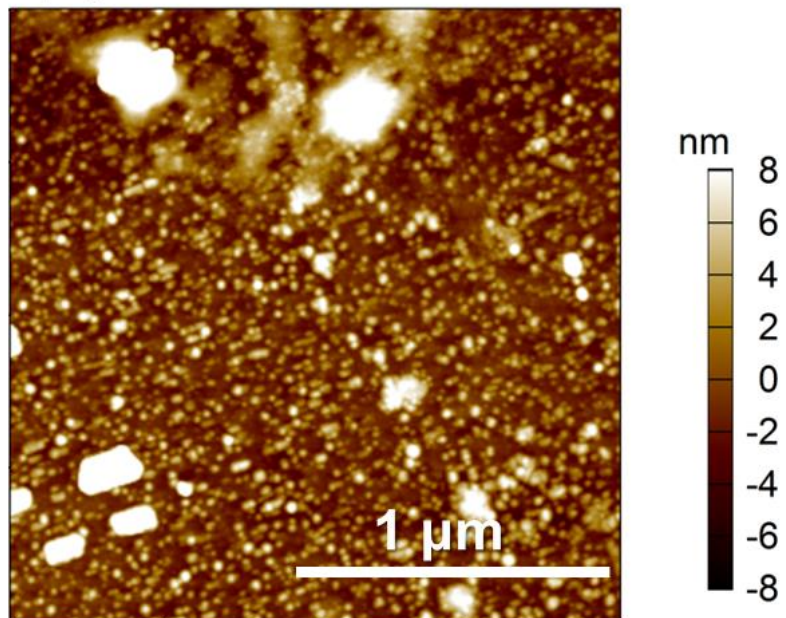
Figure 5-11: (a) RHEED and (b) AFM images of a BaSnO$_3$ thin film grown on SrZrO$_3$ substrate.
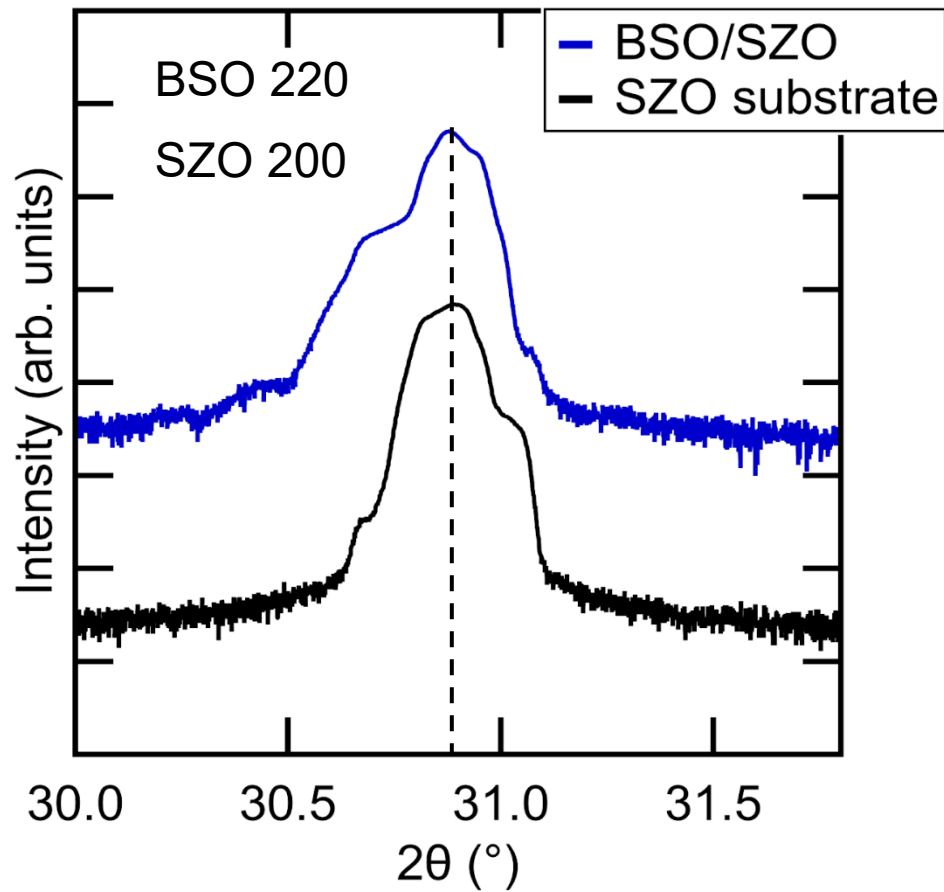
Figure 5-12: XRD 2θ-ω scans for a BaSnO$_3$ thin film grown on SrZrO$_3$ (100) substrate, and the bare SrZrO$_3$ substrate. The scans were performed near BaSnO$_3$ 220 peak. XRD courtesy of Nick. Combs.
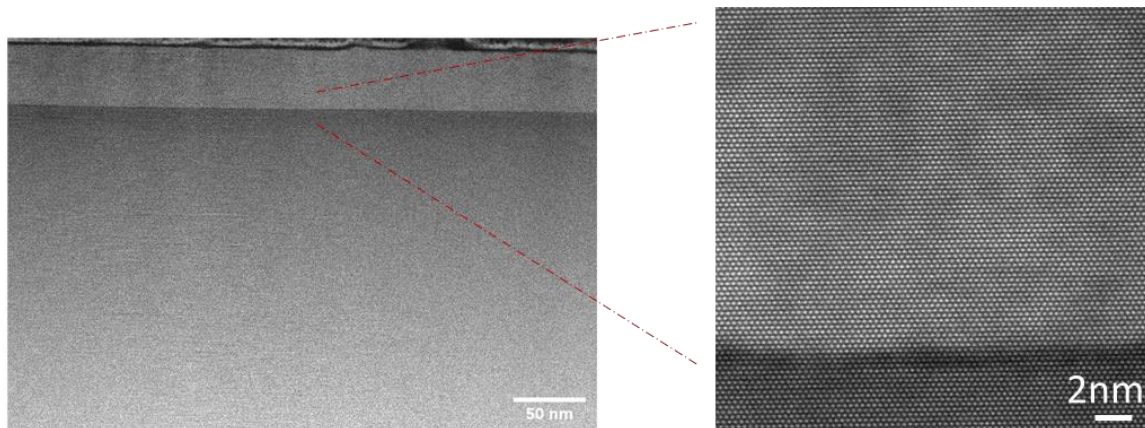
Figure 5-13: STEM images for BaSnO$_3$ thin films grown on SrZrO$_3$ (100) substrate. TEM courtesy of Honggyu Kim.

(a)

[100]

(b)

nm
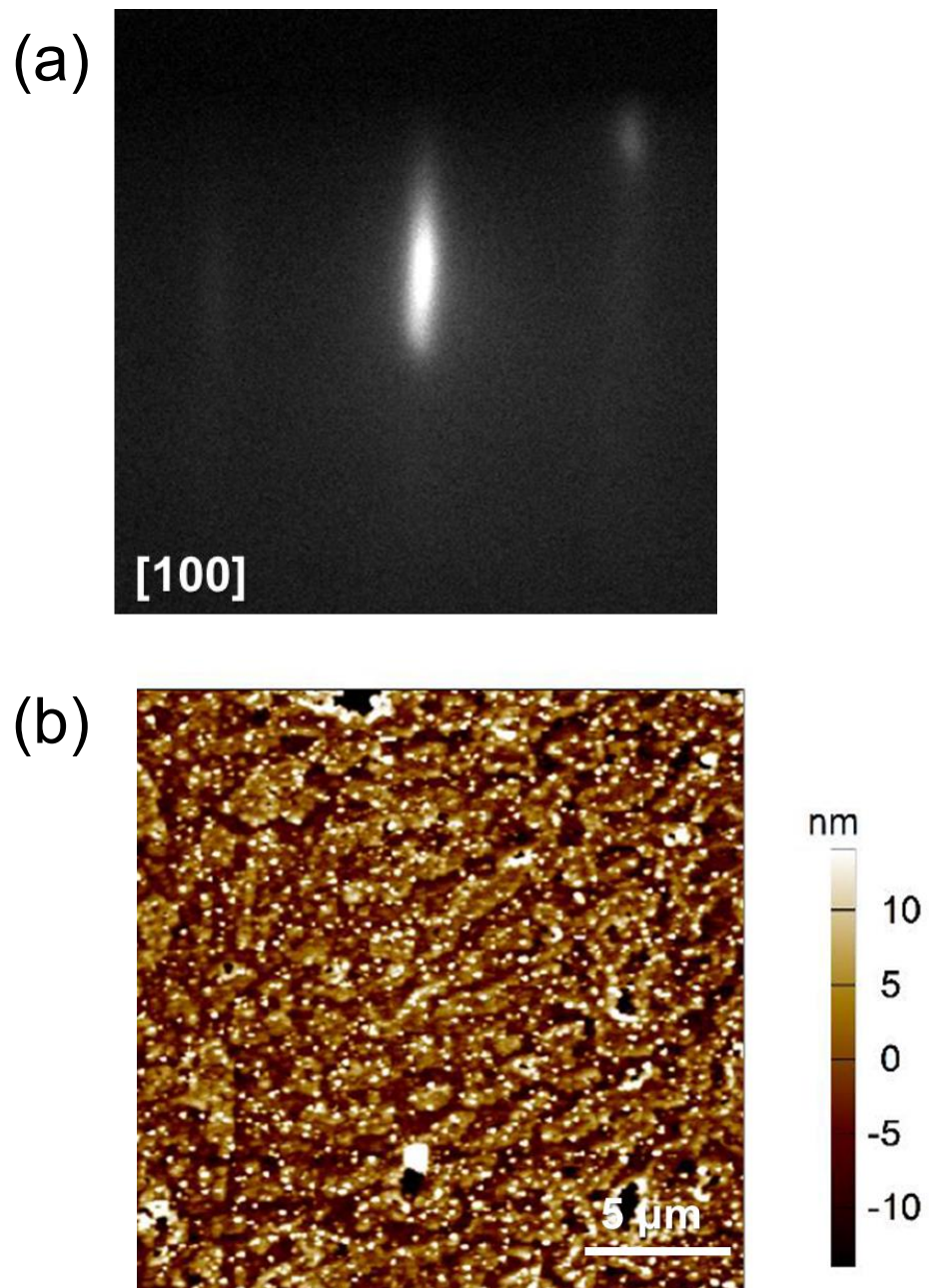
Figure 5-14: (a) RHEED and (b) AFM images of a BaSnO$_3$ thin film grown on BaSnO$_3$ substrate.
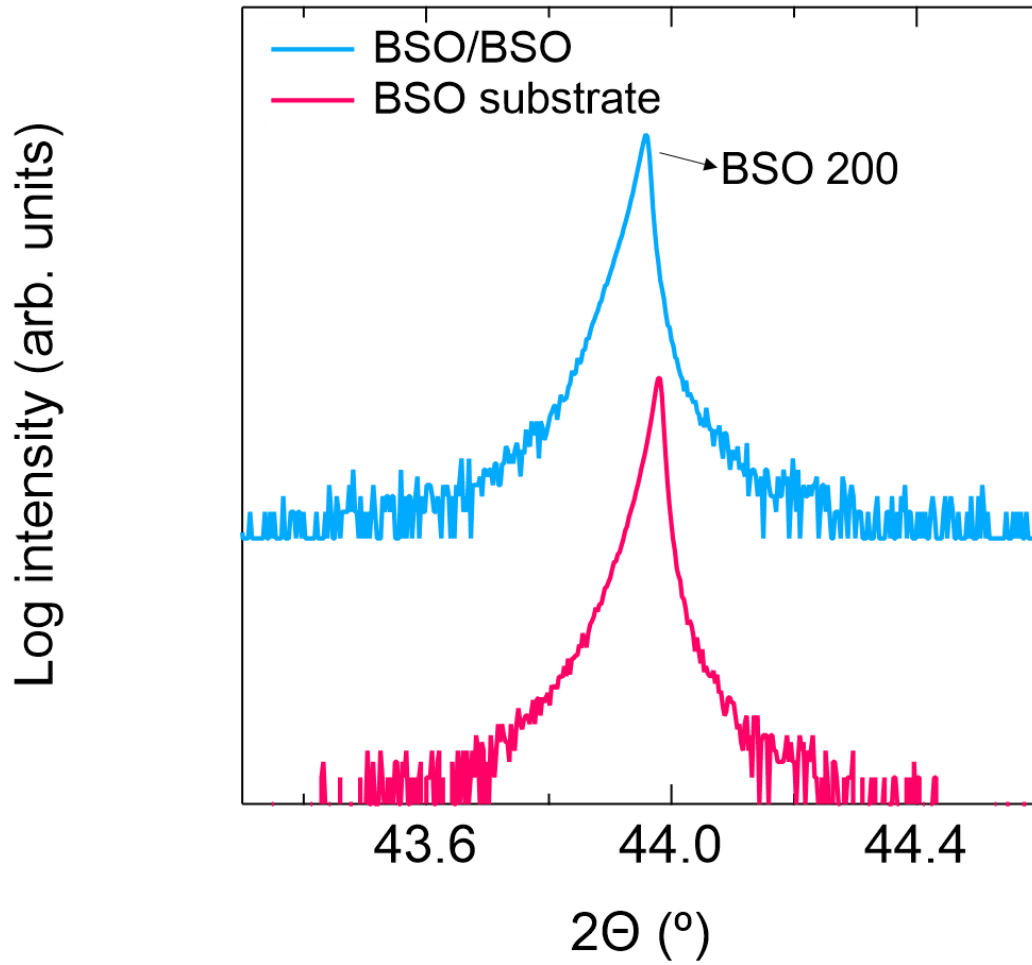
Figure 5-15: XRD 2θ-ω scans for a homoepitaxially grown BaSnO$_3$ thin film, and the bare BaSnO$_3$ substrate. The scans were performed near BaSnO$_3$ 200 peak.
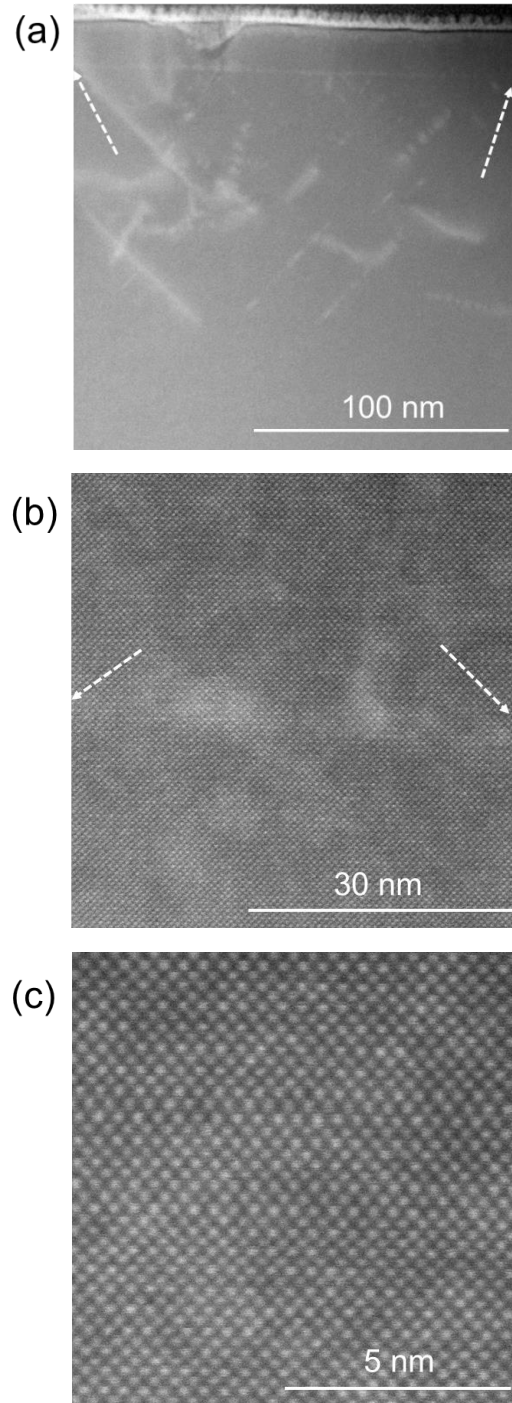
Figure 5-16: STEM images for a homoepitaxially grown BaSnO$_3$ thin film. The image magnification increases from (a) to (c). TEM courtesy of Honggyu Kim.

Chapter 6 Point defects in BaSnO$_3$

As discussed in Chapter 5, defects other than dislocations likely play a dominant role in limiting carrier mobility in BaSnO$_3$. Two- and three-dimensional defects are not observed in the transmission electron microscope images. Therefore, this Chapter turns to the exploration of point defects in BaSnO$_3$.

The first type of point defect discussed in Section 6.1 is carbon impurities. As introduced in Chapters 1 and 2, using pre-oxidized SnO$_2$ as the Sn source in molecular beam epitaxy (MBE) is necessary to improve the carrier mobility above 150 cm^{2}V^{-1}s^{-1} in BaSnO$_3$ thin films. However, SnO$_2$ can easily get chemisorbed with carbon when exposed to the atmosphere, and the following BaSnO$_3$ thin film growth may therefore incorporate carbon [87, 88]. In this Chapter, the quantitative secondary-ion mass spectrometry (SIMS) method introduced in Section 2.4 is used to measure carbon concentrations in BaSnO$_3$ thin films.

The second point defect is proposed to be Sn$_{Ba}$ antisite defect in Section 6.2 by analyzing the growth rate, x-ray diffraction (XRD) patterns, and lattice constant.

Figures 6-1, 6-2, and 6-3 are reproduced from Journal of Vacuum Science & Technology A. **38**, 043405 (2020), with permission from the American Vacuum Society. Figures 6-4, 6-5, and 6-6 are reprinted from Phys. Rev. Materials. **4**, 014604 (2020), with permission from the American Physical Society Copyright (2020).

6.1 Carbon concentrations in BaSnO$_3$ thin films grown using SnO$_2$ as source material

The BaSnO$_3$ thin films discussed in Chapter 5 and section 6.2 were all grown using a SnO$_2$ pellet source instead of powder to reduce the surface area and thus air exposure. However, in this section, a few films were intentionally grown using SnO$_2$ powder source (for a larger surface area) as a comparison to those grown with SnO$_2$ pellets. If the carbon concentration is

higher in the films grown with the powder, this may indicate that SnO_2 indeed introduces carbon contamination due to surface chemisorption.

Figure 6-1 (a) shows the carbon concentration depth profile for two $BaSnO_3$ films grown with the different SnO_2 sources (pellets and powder, respectively). The two films have similar carrier mobility (150 $cm^2V^{-1}s^{-1}$, and 140 $cm^2V^{-1}s^{-1}$, respectively) and concentrations (3.0×10^{19} cm^{-3} and 2.8×10^{19} cm^{-3}, respectively). As discussed in Chapter 1, these two carrier mobility values are essentially the same. The discussion here focuses on the interior of the $BaSnO_3$ film, where the calibration using standard samples is applied, and the interfacial transient is insignificant. The carbon concentrations in the two films are 2.6×10^{18} and 6.6×10^{18} cm^{-3}, respectively. As a comparison, $SrTiO_3$, a heavily studied oxide, can be grown with approximately ten times less carbon concentration at only mid-10^{17} atoms/cm^3 carbon despite being grown with a carbon-containing precursor [89]. The carbon density in the film grown using the SnO_2 powder source is about a factor of 2.5 higher than that of the film grown using the SnO_2 pellet source, indicating the carbon contamination is likely from the SnO_2 source. Since the nominal high purity (4N) of SnO_2 should not lead to such a high carbon impurity on the order of 10^{18} cm^{-3} inside the film, the origin of the carbon is likely from the surface absorbent during air exposure [87, 88]. This also explains why the film grown with SnO_2 pellets have lower carbon concentration. The carbon profiles on the other two samples grown with the same conditions but without a capping layer are shown in Figure 6-1 (b), where high carbon concentrations are also observed. This ensures that the carbon is not knocked from the amorphous silicon overlayer.

Figure 6-2 shows the carbon profile of a second series of films grown using the SnO_2 pellet source with and without an oxygen plasma, respectively. In general, oxygen plasma

cleaning at high temperatures can remove adsorbed carbon from surfaces. However, Figure 6-2 shows that the carbon concentrations are nearly identical in the interior of the two films. Therefore, the supplement of oxygen plasma cannot remove the high carbon impurity in $BaSnO_3$ films.

Figure 6-3 shows the carbon concentrations of the first and last grown $BaSnO_3$ film in the same growth series (~30 to 50 samples) using the SnO_2 pellet source. It is observed that the first and last loads of growth do not differ in the resulting carbon concentrations in the films, indicating that the carbon contamination on the surface of SnO_2 is not removed by cyclically heating the SnO_2 source. This is possible because when the materials on the top of the crucible evaporate, the material underneath is not outgassed and therefore still carbon chemisorbed.

6.2 Defects on Ba-site in BaSnO₃ films grown using SnO₂ as source material

This section shows that a Sn-rich growth condition is needed to achieve electron mobility above 150 $cm^2V^{-1}s^{-1}$ in $BaSnO_3$ films grown using SnO_2 as a source material due to the challenge of oxidizing Sn to a formal 4+ valence state in MBE. In principle, reductive conditions favor Sn^{2+}, and oxidative conditions select Sn^{4+} [90]. This dual valence allows Sn to occupy both A and B sites in the perovskite structure and form Sn_{Ba} antisite defect when it takes the Ba site in $BaSnO_3$ [91, 92]. The Sn-rich condition favors this substitution of Sn^{2+} with Ba^{2+} [91]. At less Sn-rich conditions, a charged defect, Ba vacancy, is likely to form and cause lattice expansion.

The film growth in this section followed the same methodology described in Chapter 2, except that different oxygen environments were supplied (i.e. the supply of no oxygen, molecular oxygen, or oxygen plasma). The SnO_2 source was in pellet form. The SnO_2/Ba flux

ratio was controlled by fixing the SnO_2 cell temperature and changing the Ba flux. The growth rate was Ba-limited (Figure 6-4), so was not changed by adding more SnO_x, indicating SnO_x was oversupplied. Accordingly, the length of growth time was adjusted so that each film was thicker than 35 nm. The film thicknesses were determined by XRD Laue fringes and confirmed by x-ray reflectivity (XRR). The thicknesses of a few films showing no Laue or XRR fringes due to the poor surface/interface were estimated from the growth rate shown in Figure 6-4.

Figure 6-5 shows XRD 2θ-ω and rocking curve scan around the $BaSnO_3$ 002 reflection for films grown with varied SnO_2/Ba flux ratios under three different oxygen environments (i.e. the supply of no oxygen, molecular oxygen, and oxygen plasma). All the films show the 002 $BaSnO_3$ reflection. A hump at the small angle side is observed in the no-oxygen sample with SnO_2/Ba flux ratio of 15, likely due to the presence of a Ruddlesden-Popper phase, Ba_2SnO_4 [93]. The rocking curves are used to evaluate the crystalline quality. For films grown without additional oxygen, the three samples with the highest SnO_2/Ba flux ratios have relatively narrower peaks, consistent with the appearances of Laue fringes, which indicate a smooth surface and interface. However, the rocking curve's lower intensity portion is different in these samples. As this portion is usually related to the diffuse scattering from point defects, the films with narrower widths should have higher mobility values. This is shown in Figure 6-6 (a). However, the carrier mobility and the width of the rocking curve relationship are inconsistent for films grown with additional oxidants. This is probably because oxygen reduces the adatom mobility when the flux arrives on the growing film surface [94] and therefore reduces crystalline perfection. Furthermore, the fact that $BaSnO_3$ can be successfully grown without any oxygen supply indicates that the oxygen needed in $BaSnO_3$ is mainly from the SnO_2 source. As introduced in Chapter 1, the main species evaporating from the SnO_2 cell are

~77% SnO, ~20% O, and other molecules. The films are thus grown under oxygen-poor conditions. Besides, SnO is the main species, so it is likely that the condition is also Sn-rich, which is consistent with the Ba-limited growth rate. This non-stoichiometric (O-poor and Sn-rich) growth condition will likely induce point defects in compounds without an MBE growth window.

Figure 6-6 shows the out-of-plane lattice parameter and electron mobility as a function of SnO_2/Ba flux ratios for three series ((a)-(c)) of $BaSnO_3$ films. The most pronounced observation is that most out-of-plane lattice constants are smaller than the stoichiometric value, 4.116 Å. This deviation indicates that there is a point defect contracting the lattice. Cation vacancies typically lead to lattice expansion due to the electrostatic effect [95, 96]. Oxygen vacancies may also have a moderate lattice expansion effect for $BaSnO_3$ [97]. An exception is that the incorporation of Sn^{2+} to the Ba site may cause lattice contraction due to the smaller size of Sn^{2+} than Ba^{2+} [98]. This size effect has also been reported in other Sn-containing perovskites [92, 99, 100]. Therefore, the small out-of-plane lattice constant might result from forming Sn_{Ba} antisite defects. This hypothesis is consistent with a density functional theory (DFT) calculation for $BaSnO_3$ under oxygen-poor and Sn-rich conditions, where Sn^{2+} ions are induced and favored to fill into the Ba site [91].

Figure 6-6 (a) also shows that the out-of-plane lattice constant approaches the stoichiometric value by decreasing the SnO_2/Ba flux ratio. However, the carrier mobility does not increase with this apparently improved stoichiometry. Instead, the films become more resistive at low SnO_2/Ba flux ratios. Therefore, the nominal stoichiometry is likely due to a defect-caused lattice expansion when the SnO_2/Ba flux ratio is lowered. The expansion compensates for the contraction effect from the Sn_{Ba} antisite defect, leading to the apparent

94

stoichiometric lattice constant. In addition, this point defect should have a strong scattering effect that contribute to the poor electron mobility. DFT calculation of $BaSnO_3$ under less Sn-rich condition [91] shows that Ba vacancies are a possible point defect. Since a Ba vacancy is a charged defect, it can cause lattice expansion and serve as a more robust scattering source (as an acceptor) compared to the charge-neutral Sn_{Ba} antisite defect. The formation of Ba vacancy also naturally understandable because when Sn-richness in the growth condition decreases, the number of Sn^{2+} that can be filled into the Ba site is also reduced.

Figure 6-6 also indicates that the supply of molecular oxygen and oxygen plasma will shift the growth condition of high-mobility $BaSnO_3$ thin films to less Sn-rich. This is because the extra oxygen reduces the need for SnO to supply oxygen. However, the small out-of-plane lattice constant still indicates the presence of Sn_{Ba} antisite defects inside these films. Therefore, even with an activated oxygen plasma, the environment is still not oxidative enough. This means that SnO must be oversupplied, making the growth condition Sn-rich. To achieve actual stoichiometric $BaSnO_3$ films, a more oxidizing growth environment is needed.

6.3 Conclusion

The point defects in La-doped $BaSnO_3$ films grown by MBE using Ba, La, and SnO_2 sources with and without additional oxidants have been discussed in this work. High carbon contaminations of low- to mid- 10^{18} atoms/cm^3 are detected in all the films. The possible cause has been attributed to the chemisorbed carbon on the surface of the SnO_2 source material due to the exposure to air. Neither oxygen plasma nor SnO_2 source outgassing is effective to reduce the carbon concentrations in the films. Using large SnO_2 crystals is probably an approach to lower the surface adsorbent. Except for carbon impurity, an analysis of the growth rate, XRD patterns, and lattice constant indicates that Sn-rich and O-poor growth conditions are present

during all the films' growths. It is because the growth environment is not sufficiently oxidative, so SnO needs to be oversupplied as the primary source of oxygen. The excess Sn ions with the valence state of 2+ are accommodated into the Ba site as an antisite defect. Less Sn-rich growth condition leads to the formation of Ba vacancies, which compensate the lattice contraction effect from Sn_{Ba} antisite defects. Ba vacancies are a charged defect and thus reduce the electron mobility in the films. To fully oxidize the films, a more oxidizing environment is needed. However, it is difficult to achieve this environment in MBE. Both carbon impurities and Sn_{Ba} antisite defects are of importance because they may bound thin film mobility. Future work should focus on reducing these defects. A possible method of using oxygen-contained metalorganics is proposed in Chapter 7.
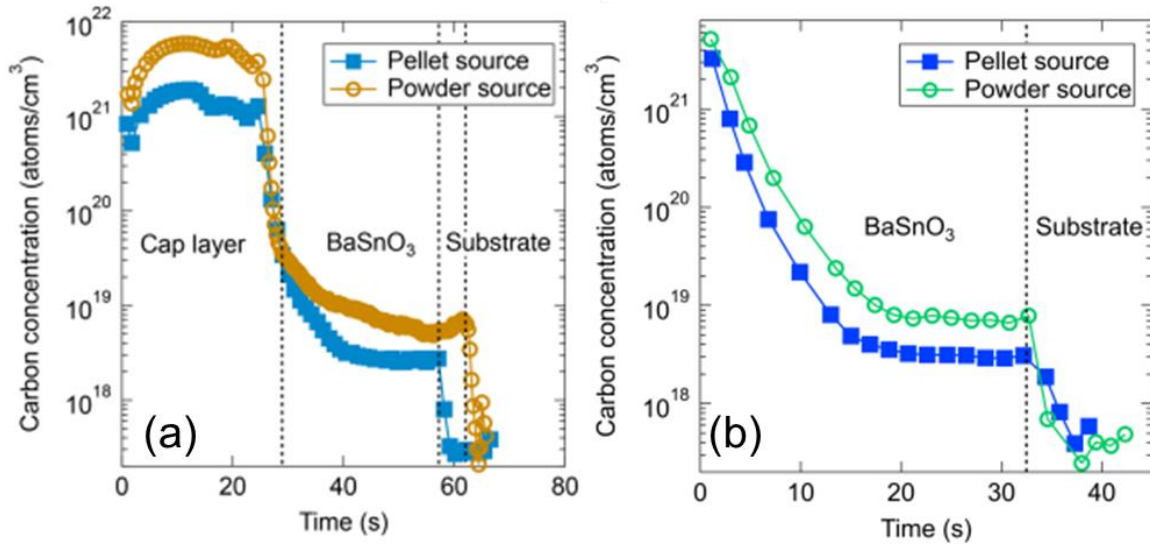
Figure 6-1: SIMS carbon impurity concentration as a function of etching time for BaSnO₃ films grown using pellet and powder SnO₂ sources, respectively. The line connecting data points is used as a guide for the eye. The quantitative concentration is valid only in the BaSnO₃ film interior, calibrated using standard samples. All films were grown with oxygen plasma. The films in (a) are capped with silicon. The films in (b) are uncapped. Figure reprinted from [101], with permission from the American Vacuum Society.
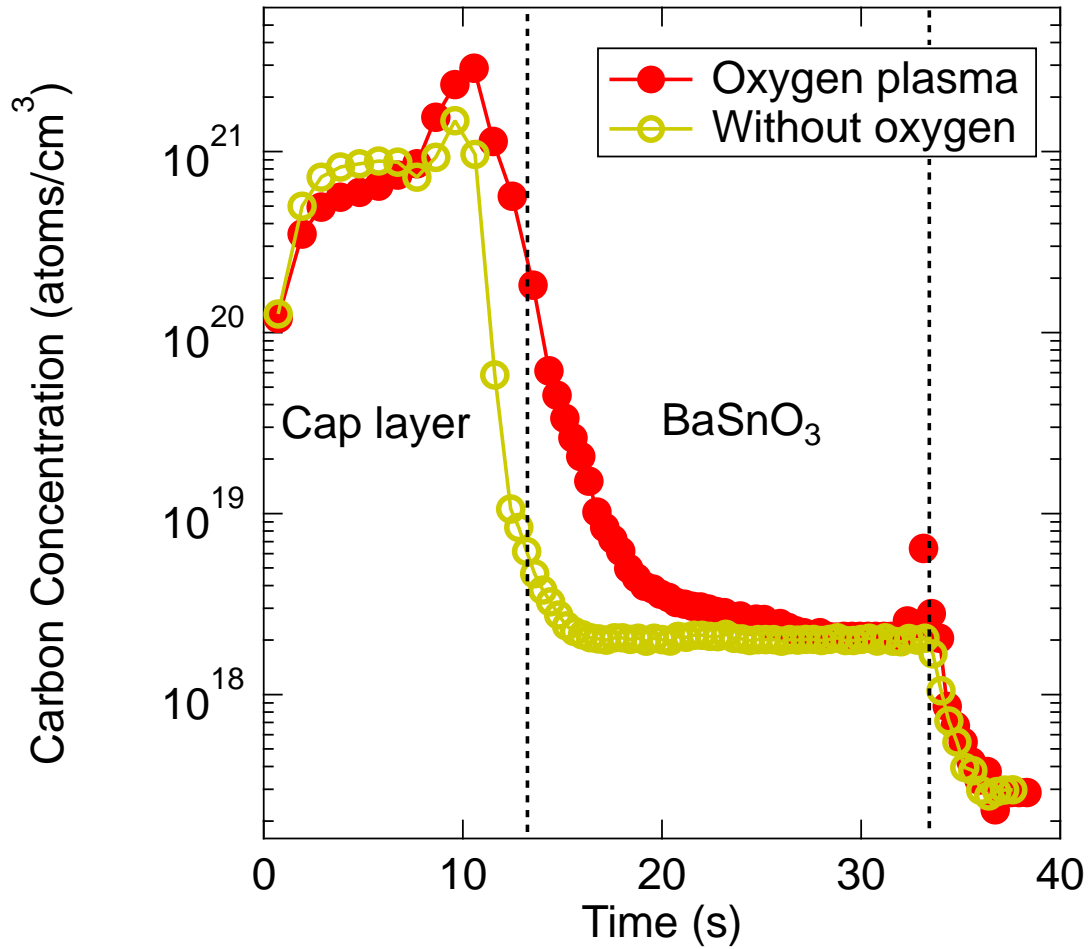
Figure 6-2: SIMS carbon impurity concentration as a function of etching time for two BaSnO$_3$ films grown using pellet SnO$_2$ sources, with and without oxygen plasma. The line connecting data points is used as a guide to the eye. The quantitative concentration is valid only in the BaSnO$_3$ film interior, calibrated using standard samples. Figure reprinted from [101], with permission from the American Vacuum Society.
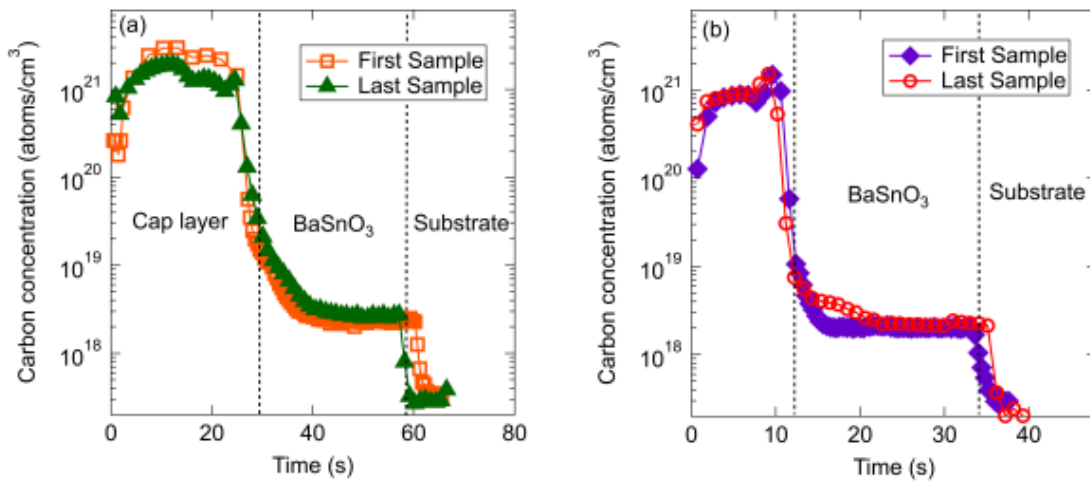
Figure 6-3: SIMS carbon impurity concentration as a function of etching time for BaSnO$_3$ films grown using pellet with (a) oxygen plasma assisted and (b) no oxygen assisted. The plots show the first and last samples in the growth series. The line connecting data points is used as a guide to the eye. The quantitative concentration is valid only in the BaSnO$_3$ film interior, calibrated using standard samples. Figure reprinted from [101], with permission from the American Vacuum Society.
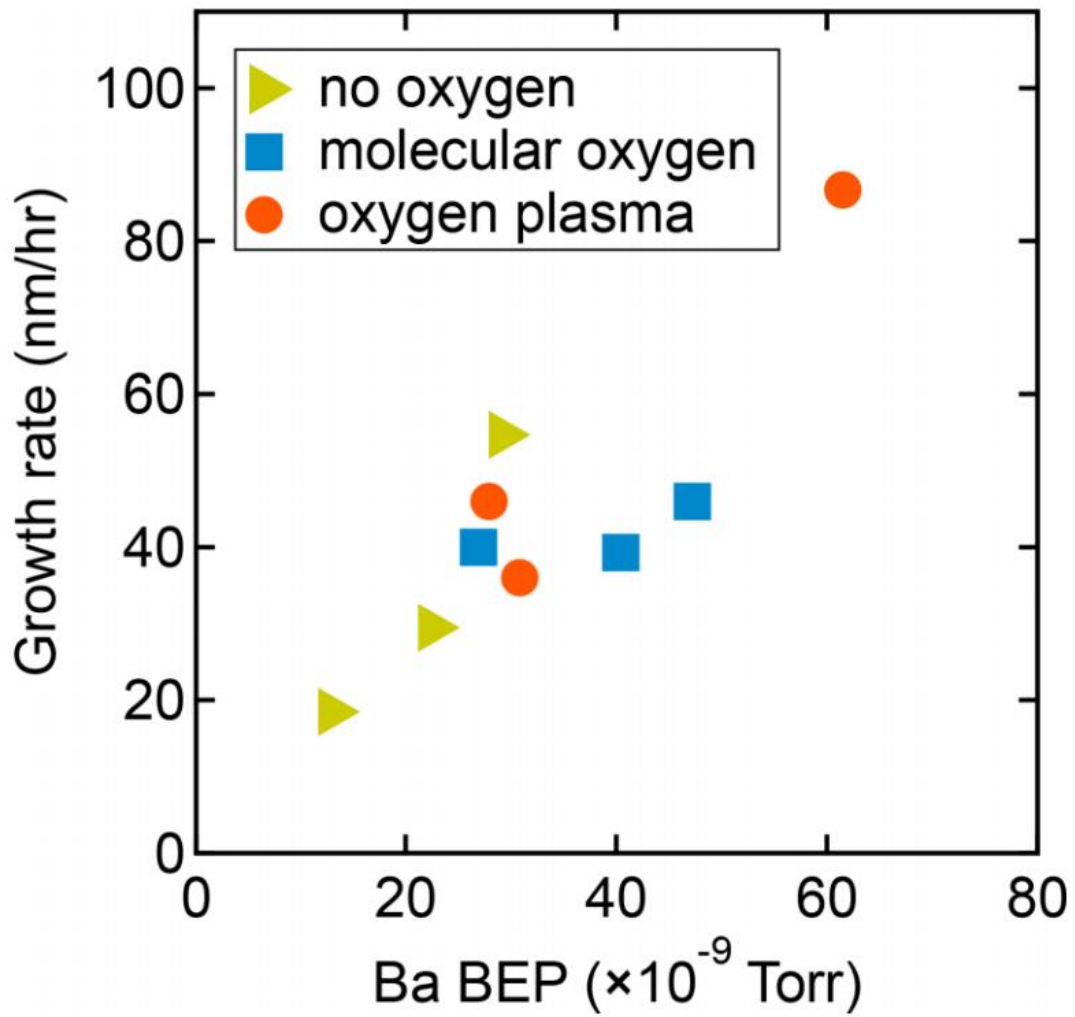
Figure 6-4: BaSnO$_3$ growth rate as a function of Ba beam equivalent pressure. Figure reprinted from [102], Copyright (2020) by the American Physical Society.
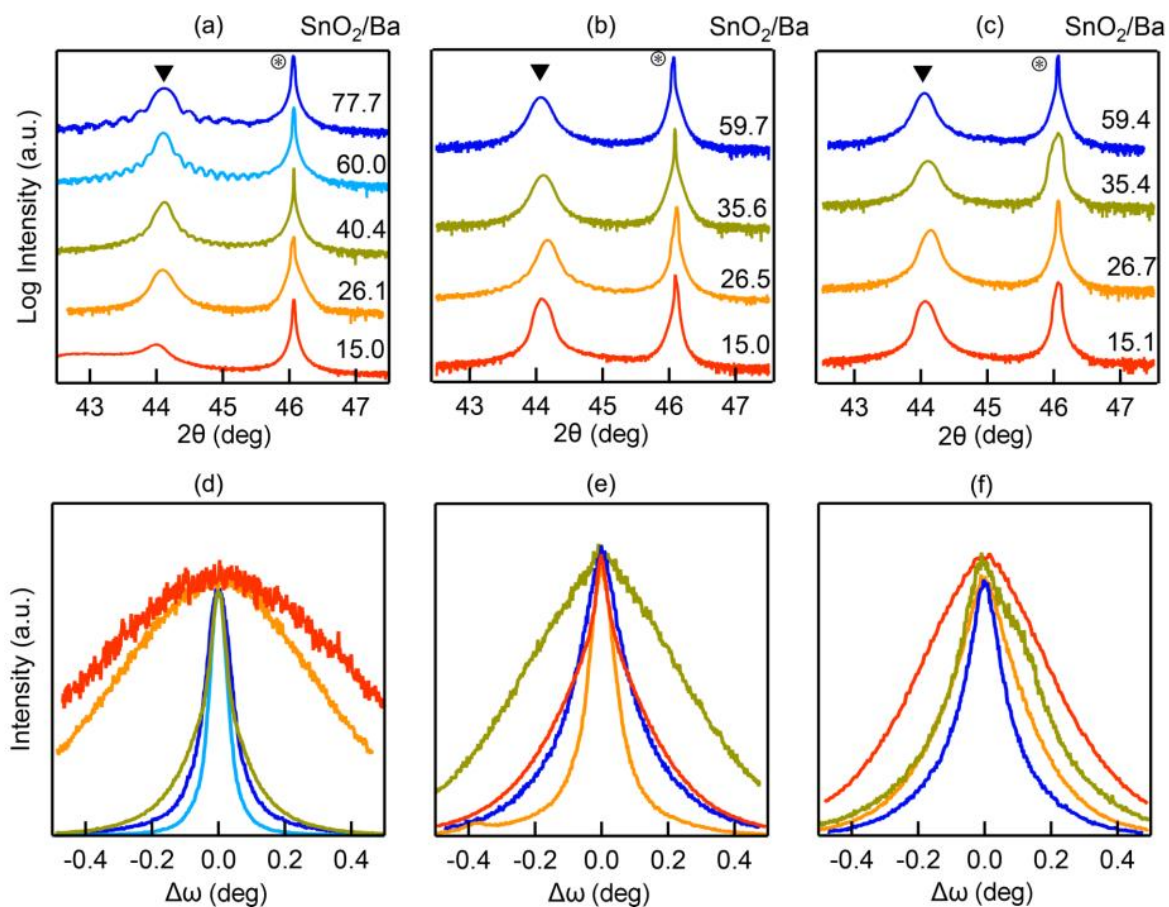
Figure 6-5: 2θ-ω scans for BaSnO$_3$ films grown with different SnO$_2$/Ba flux ratios. The measurements are performed around 002 reflection on the samples grown with (a) no oxygen, (b) molecular oxygen, and (c) oxygen plasma. (d)-(f) are the rocking curves for the samples in (a)-(c), respectively. Figure reprinted from [102], Copyright (2020) by the American Physical Society.
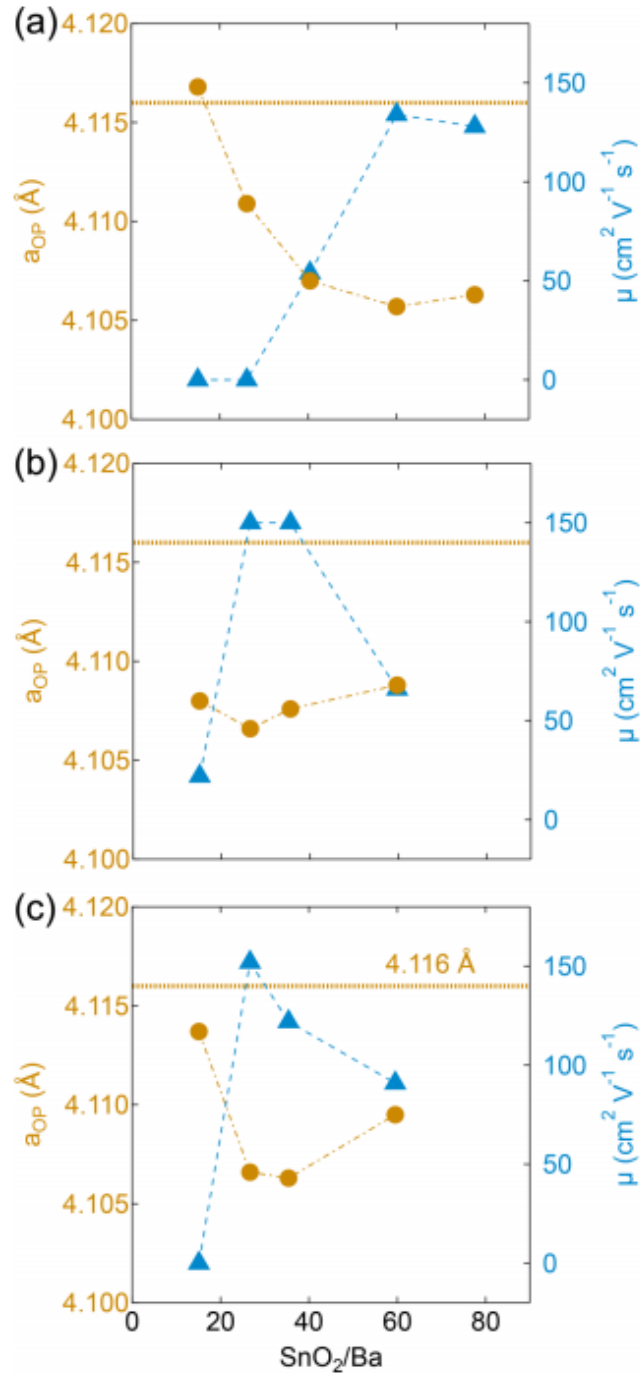
Figure 6-6: The out-of-plane lattice parameter and carrier mobility for BaSnO$_3$ films grown with different SnO$_2$/Ba flux ratios. The samples are grown with (a) no oxygen, (b) molecular oxygen, and (c) oxygen plasma. Figure reprinted from [102], Copyright (2020) by the American Physical Society.

Chapter 7 Summary and future directions

7.1 Summary of work

This thesis focused on exploring and understanding the structural and electrical properties of antiperovskite Sr_3SnO and perovskite $BaSnO_3$. Although both materials are stannates, their properties are very different. Sr_3SnO is of interest due to its topological band structure and the possible superconductivity observed in bulk $Sr_{3-x}SnO$ polycrystalline ceramics, while $BaSnO_3$ attracted attention as a transparent conducting oxide. In addition, the current challenges in the study of Sr_3SnO and $BaSnO_3$ are naturally different. For Sr_3SnO, the most challenging problem is that this material is highly air sensitive and therefore hard to design experiments for structural characterization and electrical measurements. For $BaSnO_3$, the carrier mobility has a bottleneck, and improvement was insufficient.

In this work, the use of molecular beam epitaxy (MBE), introduced in Chapters 2 and 3, enabled the growth of Sr_3SnO and $BaSnO_3$ thin films. This allowed for research regarding the materials property characterization and perfection. For Sr_3SnO antiperovskite, due to its extreme air sensitivity, a series of air-isolated methods were developed to characterize the phase purity and intrinsic transport properties. The characterization results showed that phase-pure conducting Sr_3SnO films could be grown by MBE, where the carriers were p-type likely from the Sr deficiency. However, broad-range tuning of carrier density by varying the stoichiometry was not permitted in phase-pure Sr_3SnO films because the deliberate creation of Sr vacancies introduced larger concentrations of Sn-rich secondary phases. As discussed in Chapter 4, a p-type dopant must be used to tune the carrier density while maintaining the phase purity of Sr_3SnO. The use of indium successfully increased the carrier density above 10^{21} cm^{-3}, where bulk $Sr_{3-x}SnO$ polycrystalline ceramics were found to be superconductive. However, the superconducting transition was not observed in the phase-pure indium-doped $Sr_{3-x}SnO$ film.

Therefore, the observed superconductivity in the bulk $Sr_{3-x}SnO$ crystals is likely extrinsic. Despite that, interesting phenomena were reported in Chapters 3 and 4, such as a weak-antilocalization behavior and a linear temperature dependence in sheet resistance at a high carrier density regime.

Aside from the the observation of weak antilocalization (see Chapter 3 and [49]) and planar Hall effect [50], more direct evidence of the topological nature of Sr_3SnO in transport are missing. Properties such as the giant linear magnetoresistance and quantum oscillations, which would allow for more insights into the bulk electronic structure and, possibly, surface or boundary states, can only be observed when the material has a much higher carrier mobility than what was observed here [103, 104]. The highest hole carrier mobility in the Sr_3SnO films discussed in this work is only 400 $cm^2V^{-1}s^{-1}$, a magnitude to magnitudes lower than the mobilities in typical topological semimetals. The low hole carrier mobilities in the Sr_3SnO films are possibly caused by the defects scattering and film degradation, as the degradation can only be reduced but not avoided. Therefore, thickness dependence study cannot be used to reveal (if there is) a conductive surface state because the degraded products can influence the overall transport behavior.

Another missing signature is the expected mixed n-type and p-type conductivity when the Fermi level gets close to the gapped Dirac node. This is possibly caused by a combined effect of relatively high hole carrier density of mid-10^{18} cm^{-3} (therefore the Fermi level is not very close to the Dirac node).

Experiments involving $BaSnO_3$ can be performed in the air, so the characterization techniques are more straightforward than that for Sr_3SnO. The main challenge for $BaSnO_3$ thin films is perfecting the materials structure so that the carrier mobility in thin films can be as

high as in bulk $BaSnO_3$ crystals. The well-known and recognized mobility-limiting defect is threading dislocation resulting from the lattice mismatch between $BaSnO_3$ films and widely available substrate. This extended defect in $BaSnO_3$ films is cleared using $SrZrO_3$ and $BaSnO_3$ substrates, as discussed in Chapter 5. However, the carrier mobility is still not improved, although the transmission electron microscopic images show that the films are dislocation free. More film growths experiments on these substrates to optimize the stoichiometry is desired, limited here by COVID and lack of supply of more substrates. Chapter 6 shows that carbon impurity and Sn_{Ba} antisite defects are found in $BaSnO_3$ thin films. These point defects are suspected to be the cause of the lower carrier mobility in $BaSnO_3$ thin films than in bulk crystals.

7.2 Directions for future work in Sr_3SnO

7.2.1 Indium dopant in bulk Sr_3SnO crystals

The understanding of the roles of the impurity phases in the superconductivity of bulk $Sr_{3-x}SnO$ crystals is poor. Before this work, *x*-ray diffraction (XRD) was the only method used to detect the impurity phases in the bulk and thin film Sr_3SnO, which is found to be insufficient, as introduced in Chapter 3. Microscopic images must be used as a supplement to make sure phase purity.

In this work, phase-pure indium doped Sr_3SnO thins films with carrier density above 10^{21} cm^{-3} are observed not to be superconductive, leading to the suggestion that the superconductivity observed in bulk Sr_3SnO crystals is impurity-caused. This hypothesis can be investigated by performing the same experiments in thin films to bulk crystals. Specifically, stoichiometric bulk Sr_3SnO crystals can be grown first, and the phase purity can be checked

by XRD and a scanning electron microscope equipped with a focused ion beam. These samples can then be doped with indium to increase the carrier density above 10^{21} cm^{-3}. This can double check the intrinsicality of the superconductivity.

7.2.2 The origin of the linear-in-temperature resistance of highly doped Sr$_3$SnO thin films

As introduced in Chapter 4, the temperature dependence (80 K < T < 200 K) of sheet resistance becomes more linear with the increase of carrier density. The origin of this trend is not well understood. Whether or not it is related to the position of the Fermi level in the band structure is still unknown. Therefore, further theoretical investigation could propose possible explanations and predict transport behavior as a function of the Fermi level position. Experimental work can then follow by validating the theories since indium has proven capable of precisely controlling carrier density (therefore, Fermi level).

7.3 Directions for future work in BaSnO$_3$

7.3.1 Improving the quality of lattice-matched substrates

As introduced in Chapter 5, BaSnO$_3$ films were grown on lattice-matched substrates and thus cleared from threading dislocations. However, the carrier mobility values were not improved. Therefore, we suspect that other defects may limit the mobility. This result is a speculation instead of a conclusion because the crystalline quality of the substrates is not as excellent as other commercially available substrates. The not-improved carrier mobility in BaSnO$_3$ films is possibly just due to the extended poor crystalline quality. Therefore, more work on improving the quality of the lattice-matched substrate is needed.

7.3.2 Using oxygen-contained Sn metalorganics for BaSnO$_3$ films

As discussed in Chapter 6, the formation of Sn$_{Ba}$ antisite defects is fundamentally due to the O-poor growth environment. Potentially, this issue can be solved by using a higher oxygen plasma flux or more active oxidants. However, this could lead to the surface oxidation of the metal source materials, decreasing the fluxes from the effusion cells.

An alternative approach to introducing more oxygen to the growth is incorporating it into a metalorganic precursor as source material. For example, titanium tetraisopropoxide can be used to grow stoichiometric SrTiO$_3$ without supplying additional oxygen. (CH$_3$)$_6$Sn$_2$ has been used to grow BaSnO$_3$ thin films in MBE [96]. However, (CH$_3$)$_6$Sn$_2$ contains no oxygen, so the resulting carrier mobility is not improved [96]. Tin tert-butoxide (TTB) that contains four oxygen atoms around a tin atom has been used for BaSnO$_3$ growth by Chris Freeze (former student in the Stemmer group at UCSB), while the conclusion is that the precursor decomposes in the supply lines at the temperatures sufficient to sustain enough vapor pressure [30].

No other oxygen-contained Sn metalorganic precursors have been tried to date. This is probably due to the high cost of testing a metalorganic precursor source in MBE. However, finding a proper precursor can be done in a simplified system that only includes a precursor source, a supply line, a space equipped with an ion gauge, and a pump (see Figure 7-1 as an example). The expensive and easy-to-block linear leak valve (introduced in Chapter 2) can be avoided because the system only needs to ensure enough flux (not precise control) of the precursor can pass through the supply line without decomposition like TTB. Such a system can be built without much cost. In addition, chemistry labs can also focus on synthesizing an oxygen-contained Sn metalorganic precursor based on the need for MBE use.
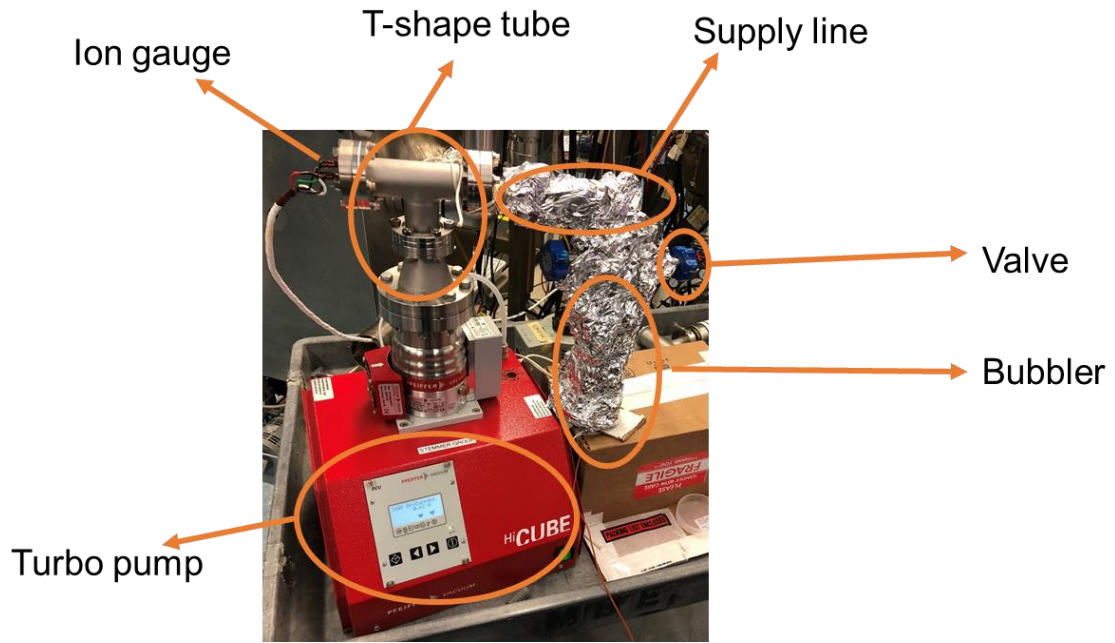
Figure 7-1: A system used to test the functionality of metalorganic precursors. The precursor is filled in a bubbler that valves can seal. A supply line connects the bubbler with a T-shape tube equipped with an ion gauge. The T-shape tube simulates the environment of a MBE growth chamber and is pumped by a turbo. The bubbler and the supply line are warped by heating tapes and Al foils to increase the temperature to achieve sufficient vapor pressure.

Bibliography

[1]   J. M. Edge, Y. Kedem, U. Aschauer, N. A. Spaldin, A. V. Balatsky, *Quantum critical origin of the superconducting dome in SrTiO$_3$*, *Phys. Rev. Lett.* **115**, 247002 (2015).

[2]   S. E. Rowley, L. J. Spalek, R. P. Smith, M. P. M. Dean, M. Itoh, J. F. Scott, G. G. Lonzarich, S. S. Saxena, *Ferroelectric quantum criticality*, *Nat. Phys.* **10**, 367–372 (2014).

[3]   S. E. Rowley, C. Enderlein, J. F. de Oliveira, D. A. Tompsett, E. B. Saitovitch, S. S. Saxena, G. G. Lonzarich, *Superconductivity in the vicinity of a ferroelectric quantum phase transition*, arXiv:1801.08121 [cond-mat.supr-con] (2018).

[4]   K. Dunnett, A. Narayan, N. A. Spaldin, A. V. Balatsky, *Strain and ferroelectric soft-mode induced superconductivity in strontium titanate*, *Phys. Rev. B* **97**, 144506 (2018).

[5]   H. J. Kim, U. Kim, H. M. Kim, T. H. Kim, H. S. Mun, B.-G. Jeon, K. T. Hong, W.-J. Lee, C. Ju, Kee Hoon Kim, and K. Char, *High mobility in a stable transparent perovskite oxide*, Appl. Phys. Expr. **5**, 061102 (2012).

[6]   H. J. Kim, U. Kim, T. H. Kim, J. Kim, H. M. Kim, B. G. Jeon, W. J. Lee, H. S. Mun, K. T. Hong, J. Yu, K. Char, and K. H. Kim, *Physical properties of transparent perovskite oxides (Ba,La)SnO$_3$ with high electrical mobility at room temperature*, Phys. Rev. B **86**, 165205 (2012).

[7]   X. Luo, Y. S. Oh, A. Sirenko, P. Gao, T. A. Tyson, K. Char, and S. W. Cheong, *High carrier mobility in transparent Ba$_{1-x}$La$_x$SnO$_3$ crystals with a wide band gap*, Appl. Phys. Lett. **100**, 172112 (2012)

[8]   H. Mizoguchi, H. W. Eng, and P. M. Woodward, *Probing the Electronic Structures of Ternary Perovskite and Pyrochlore Oxides Containing Sn^{4+} or Sb^{5+}*, Inorg. Chem. **43**, 1667 (2004).

[9]   S. Ismail-Beigi, F. J. Walker, S. W. Cheong, K. M. Rabe, and C. H. Ahn, *Alkaline earth stannates: The next silicon*, APL Mater. **3**, 062510 (2015).

[10]   Z. B. Xia, C. Y. Wang, N. K. Kalarickal, S. Stemmer, and S. Rajan, *Design of transistors using high-permittivity materials*, IEEE Trans. Electron Devices **66**, 896 (2019).

[11]   H. Chandrasekar, J. N. Cheng, T. S. Wang, Z. B. Xia, N. G. Combs, C. R. Freeze, P. B. Marshall, J. McGlone, A. Arehart, S. Ringel, A. Janotti, S. Stemmer, W. Lu, and S. Rajan, *Velocity saturation in La-doped $BaSnO_3$ thin films*, Appl. Phys. Lett. **115**, 092102 (2019).

[12]   T. Schumann, S. Raghavan, K. Ahadi, H. Kim, and S. Stemmer, *Structure and optical band gaps of $(Ba,Sr)SnO_3$ films grown by molecular beam epitaxy*, J. Vac. Sci. Technol. A **34**, 050601 (2016).

[13]   P. Singh, B. J. Brandenburg, C. P. Sebastian, P. Singh, S. Singh, D. Kumar, and O. Parkash, *Electronic Structure, Electrical and Dielectric Properties of $BaSnO_3$ below 300 K*, Jpn. J. Appl. Phys. 47, 3540 (2018)

[14]   S. James Allen, S. Raghavan, T. Schumann, K.-M. Law, and S. Stemmer, *Conduction band edge effective mass of La-doped $BaSnO_3$*, Appl. Phys. Lett.108, 252107 (2016).

[15]   I. A. Rauf, *Structure and properties of tin-doped indium oxide thin films prepared by reactive electron-beam evaporation with a zone-confining arrangement*, J. Appl. Phys. **79**, 4057 (1996).

[16]   F. O. Adurodija, H. Izumi, T. Ishihara, H. Yoshioka, M. Motoyama and K. Murai, *Pulsed laser deposition of crystalline indium tin oxide films at room temperature by substrate laser irradiation*, Jpn. J. Appl. Phys. **39**, L377 (2000).

[17]   A. Suzuki, T. Matshushita, T. Aoki, Y. Yoneyama and M, Okuda, *Pulsed Laser Deposition of Transparent Conducting Indium Tin Oxide Films in Magnetic Field Perpendicular to Plume*, Jpn. J. Appl. Phys. **40**, L401 (2001).

[18]   Y. Sawada, C. Kobayashi, S. Seki, and H. Funakubo. *Highly-Conducting Indium-Tin-Oxide Transparent Films Fabricated by Spray CVD Using Ethanol Solution of Indium (III) Chloride and Tin (II) Chloride*, Thin Solid Films **409**, 1, 16 (2002).

[19]   A. Suzuki, Tatsuhiko Matsushita, Takanori Aoki, Akihito Mori, and Masahiro Okuda, *Highly Conducting Transparent Indium Tin Oxide Films Prepared by Pulsed Laser Deposition*, Thin Solid Films **411**, 1, 23 (2002).

[20]   K. Ganguly, P. Ambwani, P. Xu, J. S. Jeong, K. A. Mkhoyan, C. Leighton, and B. Jalan, *Structure and transport in high pressure oxygen sputter-deposited $BaSnO_{3-d}$,* APL Mater. **3**, 062509 (2015).

[21]   S. Sallis, D. O. Scanlon, S. C. Chae, N. F. Quackenbush, D. A. Fischer, J. C. Woicik, J. H. Guo, S. W. Cheong, and L. F. J. Piper, *La-doped $BaSnO_3$—Degenerate perovskite*

transparent conducting oxide: Evidence from synchrotron x-ray spectroscopy, Appl. Phys. Lett. **103**, 042105 (2013).

[22]   P. V. Wadekar, J. Alaria, M. O'Sullivan, N. L. O. Flack, T. D. Manning, L. J. Phillips, K. Durose, O. Lozano, S. Lucas, J. B. Claridge, and M. J. Rosseinsky, *Improved electrical mobility in highly epitaxial La:BaSnO₃ films on SmScO₃(110) substrates*, Appl. Phys. Lett. **105**, 052104 (2014).

[23]   H. J. Kim, U. Kim, T. H. Kim, J. Kim, H. M. Kim, B. G. Jeon, W. J. Lee, H. S. Mun, K. T. Hong, J. Yu, K. Char, and K. H. Kim, *Physical properties of transparent perovskite oxides (Ba,La)SnO₃ with high electrical mobility at room temperature*, Phys. Rev. B. **86**, 165205 (2012).

[24]   H. Paik, Z. Chen, E. Lochocki, A. Seidner H., A. Verma, N. Tanen, J. Park, M. Uchida, S. Shang, B.-C. Zhou, M. Brützam, R. Uecker, Z.-K. Liu, D. Jena, K. M. Shen, D. A. Muller, and D. G. Schlom, *Adsorption-controlled growth of La-doped BaSnO₃ by molecular-beam epitaxy*, APL Mater, **5**, 116107 (2017).

[25]   S. Raghavan, T. Schumann, H. Kim, J. Y. Zhang, T. A. Cain, and S. Stemmer, *High-mobility BaSnO₃ grown by oxide molecular beam epitaxy*, APL Mater, 4, 016106, (2016).

[26]   R. H. Lamoreaux, D. L. Hildenbrand, and L. Brewer, *High-Temperature Vaporization Behavior of Oxides II. Oxides of Be, Mg, Ca, Sr, Ba, B, Al, Ga, In, Tl, Si, Ge, Sn, Pb, Zn, Cd, and Hg*, J. Phys. Chem. Ref. Data **16**, 419 (1987).

[27]   R. Colin, J. Drowart, and G. Verhaegen, *Mass-Spectrometric Study of the Vaporization of Tin Oxides*, Trans. Faraday Soc. **61**, 1364 (1965).

[28] E. Zimmermann, S. Königs, and D. Neuschütz, *Mass Spectrometric Determination of the Partial Pressures of SnO, Sn_2O_2 and O_2 in Equilibrium with Solid SnO_2*, Z. Phys. Chem. **209**, 271 (1999).

[29] L. Weston, L. Bjaalie, K. Krishnaswamy, and C. G. Van de Walle, *Origins of n-type doping difficulties in perovskite stannates*, Phys. Rev. B **97**, 054112 (2018)

[30] C. R. Freeze, *Molecular beam epitaxy of wide-band gap perovskite oxides: (Ba, Sr)TiO_3 and $BaSnO_3$ (PhD thesis)*, UCSB, 40-47.

[31] N. G. Combs, W. Wu, and S. Stemmer, *Stoichiometry control in molecular beam epitaxy of $BaSnO_3$*, Phys. Rev. Mater. **4**, 014604 (2020).

[32] Y. Obata, R. Yukawa, K. Horiba, H. Kumigashira, Y. Toda, S. Matsuishi, and H. Hosono, *ARPES studies of the inverse perovskite Ca_3PbO: Experimental confirmation of a candidate 3D Dirac fermion system*, Phys. Rev. B. **96**, 155109 (2017).

[33] T. Kariyado and M. Ogata, *Three-Dimensional Dirac Electrons at the Fermi Energy in Cubic Inverse Perovskites: Ca_3PbO and Its Family*, J. Phys. Soc. Japan **80**, 083704 (2011).

[34] T. H. Hsieh, J. W. Liu, and L. Fu, *Topological crystalline insulators and Dirac octets in antiperovskites*, Phys. Rev. B **90**, 081112 (2014).

[35] R. Arras, J. Gosteau, D. Huang, H. Nakamura, H. J. Zhao, C. Paillard, and L. Bellaiche, *Spin-polarized electronic states and atomic reconstructions at antiperovskite $Sr_3SnO(001)$ polar surfaces*, Phys. Rev. B **104**, 045411 (2021).

[36] T. Kariyado and M. Ogata, *Low-Energy Effective Hamiltonian and the Surface States of Ca_3PbO*, J. Phys. Soc. Jap. **81**, 064701 (2012).

[37]   A. Ikeda, T. Fukumoto, M. Oudah, J. N. Hausmann, S. Yonezawa, S. Kobayashi, M. Sato, C. Tassel, F. Takeiri, H. Takatsu, H. Kageyama, and Y. Maeno, *Theoretical band structure of the superconducting antiperovskite $Sr_{3-x}SnO$*, Physica B **536**, 752-756 (2018).

[38]   T. Kawakami, T. Okamura, S. Kobayashi, and M. Sato, *Topological Crystalline Materials of J=3/2 Electrons: Antiperovskites, Dirac Points, and High Winding Topological Superconductivity*, Phys. Rev. X **8**, 041026 (2018).

[39]   Y. Fang and J. Cano, *Higher-order topological insulators in antiperovskites*, Phys. Rev. B **101**, 245110 (2020).

[40]   C. K. Chiu, Y. H. Chan, X. Li, Y. Nohara, and A. P. Schnyder, *Type-II Dirac surface states in topological crystalline insulators*, Phys. Rev. B **95**, 035151 (2017).

[41]   T. Kariyado, M. Ogata, *Three-Dimensional Dirac Electrons at the Fermi Energy in Cubic Inverse Perovskites: Ca_3PbO and Its Family*, J. Phys. Soc. Jpn. **80**, 083704 (2011).

[42]   M. Klintenberg, J.T. Haraldsen, A.V. Balatsky, *Computational Search for Strong Topological Insulators: An Exercise in Data Mining and Electronic Structure,* Appl. Phys. Res. **6**, 31 (2014).

[43]   M. Oudah, A. Ikeda, J. N. Hausmann, S. Yonezawa, T. Fukumoto, S. Kobayashi, M. Sato and Y. Maeno, *Superconductivity in the antiperovskite Dirac-metal oxide $Sr_{3-x}SnO$*, Nat. Commun. **7**, 13617 (2016).

[44]   J. N. Hausmann, M. Oudah, A. Ikeda, S. Yonezawa and Y. Maeno, *Controlled synthesis of the antiperovskite oxide superconductor $Sr_{3-x}SnO$*, Sci. Technol. **31**, 055012 (2018).

[45]   M. Oudah, J. N. Hausmann, S. Kitao, A. Ikeda, S. Yonezawa, M. Seto and Y. Maeno, *Evolution of Superconductivity with Sr-Deficiency in Antiperovskite Oxide $Sr_{3-x}SnO$*, Sci. Rep. **9**, 1831 (2019).

[46]   A. Ikeda, Z. Guguchia, M. Oudah, S. Koibuchi, S. Yonezawa, D. Das, T. Shiroka, H.Luetkens, and Y. Maeno, *Penetration depth and gap structure in the antiperovskite oxide superconductor $Sr_{3-x}SnO$ revealed by μ SR*, Phys. Rev. B **101**, 174503 (2020).

[47]   Y. J. Ma, A. Edgeton, H. Paik, B. D. Faeth, C. T. Parzyck, B. Pamuk, S. L. Shang, Z. K. Liu, K. M. Shen, D. G. Schlom, and C. B. Eom, *Realization of Epitaxial Thin Films of the Topological Crystalline Insulator Sr_3SnO*, Adv. Mater. **32**, 2000809 (2020).

[48]   D. Samal, H. Nakamura, and H. Takagi, *Molecular beam epitaxy of three-dimensional Dirac material Sr_3PbO*, APL Mater. **4**, 076101 (2016).

[49]   H. Nakamura, D. Huang, J. Merz, E. Khalaf, P. Ostrovsky, A. Yaresko, D. Samal, and H. Takagi, *Robust weak antilocalization due to spin-orbital entanglement in Dirac material Sr_3SnO*, Nat. Comm. **11**, 1161 (2020).

[50]   D. Huang, H. Nakamura and H. Takagi, *Planar Hall effect with sixfold oscillations in a Dirac antiperovskite*, Phys. Rev. Research. **3**, 013268 (2021).

[51]   A. Widera, H. Schafer, *Ubergangsformen zwischen Zintlphasen und echten Salzen: Die Verbindungen A_3BO (MIT A = Ca, Sr, Ba und B = Sn, Pb)*, Mater. Res. Bull **15**, 1805 (1980).

[52]   J. Nuss, C. Muhle, K. Hayama, V. Abdolazimi, and H. Takagi, *Tilting structures in inverse perovskites, M_3TtO (M = Ca, Sr, Ba, Eu; Tt = Si, Ge, Sn, Pb)*, Acta Cryst. B **71**, 300-312 (2015).

[53]   R. Arras, J. Gosteau, D. Huang, H. Nakamura, H. J. Zhao, C. Paillard, and L. Bellaiche, *Spin-polarized electronic states and atomic reconstructions at antiperovskite Sr₃SnO (001) polar surfaces*, Phys. Rev. B. **104**, 045411 (2021).

[54]   R. F. C. Farrow, *Molecular Beam Epitaxy: Applications to Key Materials*, published by Noyes, Park Ridge, (1995).

[55]   M. A. Herman and H. Sitter, *Molecular Beam Epitaxy: Fundamentals and Current Status, 2nd edition*, published by Springer-Verlag, Berlin, (1996).

[56]   J. J. Cuomo, D. L. Pappas, J. Bruley, J. P. Doyle, and K. L. Saenger, *Vapor deposition processes for amorphous carbon films with sp3 fractions approaching diamond*, J. Appl. Phys. **70**, 1706 (1991).

[57]   A. Ichimiya and P. I. Cohen, *Reflection High Energy Electron Diffraction*, published by Cambridge University Press (2004).

[58]   A. Ahtee, M. Ahtee, A. M. Glazer and A. W. Hewat, *The structure of orthorhombic SrZrO₃ by neutron powder diffraction*, Acta Cryst. B **32**, 3243 (1976).

[59]   P. Williams, *Secondary ion mass spectrometry*, Ann. Rev. Mater. Sci. **15**, 517 (1985).

[60]   L. Liu and W. A. Bassett, J. Geophys, *Changes of the crystal structure and the lattice parameter of SrO at high pressure*, Res. **78**, 8470 (1973).

[61]   S. Hikami, A. I. Larkin, and Y. Nagaoka, *Spin-Orbit Interaction and Magnetoresistance in the Two-Dimensional Random System*, Prog. Theor. Phys. **63**, 707 (1980).

[62]   H. Z. Lu, J. R. Shi, and S. Q. Shen, *Competition between weak localization and antilocalization in topological surface states*, Phys. Rev. Lett. **107**, 076801 (2011).

[63]   H. Z. Lu and S. Q. Shen, *Finite-temperature conductivity and magnetoconductivity of topological insulators*, Phys. Rev. Lett. **112**, 146601 (2014).

[64]   B. L. Altshuler and A. G. Aronov, *Zero bias anomaly in tunnel resistance and electron-electron interaction*, Solid State Commun. **30**, 115–117 (1979).

[65]   J. G. Checkelsky, Y. S. Hor, M. H. Liu, D. X. Qu, R. J. Cava, and N. P. Ong, *Quantum interference in macroscopic crystals of nonmetallic Bi_2Se_3*, Phys. Rev. Lett. **103**, 246601 (2009).

[66]   H. L. Peng, K. J. Lai, D. S. Kong, S. Meister, Y. L. Chen, X. L. Qi, S. C. Zhang, Z. X. Shen, and Y. Cui, *Aharonov-Bohm interference in topological insulator nanoribbons*, Nat. Mater. **9**, 225 (2010).

[67]   J. Chen, H. J. Qin, F. Yang, J. Liu, T. Guan, F. M. Qu, G. H. Zhang, J. R. Shi, X. C. Xie, C. L. Yang, K. H. Wu, Y. Q. Li, and L. Lu, *Gate-voltage control of chemical potential and weak antilocalization*, Phys. Rev. Lett. **105**, 176602 (2010).

[68]   J. G. Checkelsky, Y. S. Hor, R. J. Cava, and N. P. Ong, *Bulk Band Gap and Surface State Conduction Observed in Voltage-Tuned Crystals of the Topological Insulator Bi_2Se_3*, Phys. Rev. Lett. **106**, 196801 (2011).

[69]   N. Bansal, Y. S. Kim, M. Brahlek, E. Edrey, and S. Oh, *Thickness-Independent Transport Channels in Topological Insulator Bi_2Se_3 Thin Films*, Phys. Rev. Lett. **109**, 116804 (2012).

[70] H. T. He, G. Wang, T. Zhang, I. K. Sou, G. K. L. Wong, J. N. Wang, H. Z. Lu, S. Q. Shen, and F. C. Zhang, *Impurity Effect on Weak Antilocalization in the Topological Insulator Bi$_2$Te$_3$*, Phys. Rev. Lett. **106**, 166805 (2011).

[71] M. Liu, C. Z. Chang, Z. Zhang, Y. Zhang, W. Ruan, K. He, L. L. Wang, X. Chen, J. F. Jia, S. C. Zhang, Q. K. Xue, X. C. Ma, and Y. Wang, *Electron interaction-driven insulating ground state in Bi$_2$Se$_3$ topological insulators in the two-dimensional limit*, Phys. Rev. B. **83**, 165440 (2011).

[72] J. Chen, X. Y. He, K. H. Wu, Z. Q. Ji, L. Lu, J. R. Shi, J. H. Smet, and Y. Q. Li, *Tunable surface conductivity in Bi$_2$Se$_3$ revealed in diffusive electron transport*, Phys. Rev. B. **83**, 241304 (R) (2011).

[73] Y. Takagaki, B. Jenichen, U. Jahn, M. Ramsteiner, and K. J. Friedland, *Weak antilocalization and electron-electron interaction effects in Cu-doped Bi$_2$Se$_3$ films*, Phys. Rev. B. **85**, 115314 (2012).

[74] S. P. Chiu and J. J. Lin, *Weak antilocalization in topological insulator Bi$_2$Te$_3$ microflakes*, Phys. Rev. B. **87**, 035122 (2013).

[75] J. Wang, A. M. DaSilva, C. Z. Chang, K. He, J. K. Jain, N. Samarth, X. C. Ma, Q. K. Xue, and M. H. W. Chan, *Evidence for electron-electron interaction in topological insulator thin films*, Phys. Rev. B. **83**, 245438 (2011).

[76] G. Bergmann, *WEAK LOCALIZATION IN THIN-FILMS - A TIME-OF-FLIGHT EXPERIMENT WITH CONDUCTION ELECTRONS*, Phys. Rep. **107**, 1-58 (1984).

[77] J. M. Ziman, *Electrons and Phonons*, published by Oxford Press (1979).

[78] E. Haque and M. A. Hossain, *First-principles study of mechanical, thermodynamic, transport and superconducting properties of Sr_3SnO* , Journal of Alloys and Compounds. **730**, 5, 279 (2018).

[79] G. Kastle, H. G. Boyen, A Schroder, A. Plettl, and O. Ziemann, *Size effect of the resistivity of thin epitaxial gold films*, Phys. Rev. B. **70**, 165414 (2004).

[80] W. Ma, X. Zhang, and K. Takahashi, *Electrical properties and reduced Debye temperature of polycrystalline thin gold films*, J. Phys. D: Appl. Phys. **43**, 465301 (2010).

[81] A Bid, A. Bora, A.K. Raychaudhuri, *Temperature dependence of the resistance of metallic nanowires of diameter ≥ 15 nm: Applicability of Bloch-Grüneisen theorem*, Phys. Rev. B. **74**, 035426 (2006).

[82] R. Arras, J. Gosteau, D. Huang, H. Nakamura, H. J. Zhao, C. Paillard, and L. Bellaiche, *Spin-polarized electronic states and atomic reconstructions at antiperovskite Sr_3SnO (001) polar surfaces*, Phys. Rev. B. **104**, 045411 (2021).

[83] M. E. Barber, A. S. Gibbs, Y. Maeno, A. P. Mackenzie, and C. W. Hicks, *Resistivity in the Vicinity of a van Hove Singularity: Sr_2RuO_4 under Uniaxial Pressure*, Phys. Rev. Lett. **120**, 076602 (2018).

[84] D. M. Newns, C.C. Tsuei, R. P. Huebener, P.J.M. van Bentum, P.C. Pattnaik, and C.C. Chi, *Quasiclassical Transport at a van Hove Singularity in Cuprate Superconductors*, Phys. Rev. Lett. **73**, 1695 (1994).

[85] B. Guo, A. C. Lygo, T. N. Pardue, and S. Stemmer, *Hall bar measurements of topological surface states of (001) cadmium arsenide thin films interfaced with superconductors*, Phys. Rev. Mater. **6**, 034203 (2022).

[86] R. J. Terry, N. Combs, C. D. McMillen, S. Stemmer, and J. W. Kolis, *Hydrothermal growth of BaSnO₃ single crystals for wide bandgap applications,* Journal of Crystal Growth. **536**, 125529 (2020).

[87] E. W. Thornton and P. G. Harrison, J. Chem, *Tin oxide surfaces. Part 1.- Surface hydroxyl groups and the chemisorption of carbon dioxide and carbo monoxide on tin (IV) oxide*, Soc. Faraday Trans. I. **71**, 461 (1975).

[88] T. Minaai, M. Kumagai, A. Nara, and S. Tanemura, *Study of outgassing behavior of SnO₂:F films on glass in vacuum under external energy excitation*, Mater. Sci. Eng. B. **119**, 252 (2005).

[89] B. Jalan, J. Cagnon, T. E. Mates, and S. Stemmer, *Analysis of carbon in SrTiO₃ grown by hybrid molecular beam epitaxy*, J. Vac. Sci. Technol. A. **27**, 1365 (2009).

[90] M. Batzill and U. Diebold, *The surface and materials science of tin oxide*, Prog. Surf. Sci. **79**, 47 (2005).

[91] D. O. Scanlon, *Defect engineering of BaSnO₃ for high-performance transparent conducting oxide applications*, Phys. Rev. B. **87**, 161201 (R) (2013).

[92] T. Q. Wang, K. C. Pitike, Y. K. Yuan, S. M. Nakhmanson, *V. Gopalan, and B. Jalan, Chemistry, growth kinetics, and epitaxial stabilization of Sn^{2+} in Sn-doped SrTiO₃ using $(CH_3)_6Sn_2$ tin precursor*, APL Mater. **4**, 126111 (2016).

[93] U. Kumar and S. Upadhyay, *Structural, Optical and Electrical Properties of Ruddlesden Popper Oxide Ba$_2$SnO$_4$*, J. Electron. Mater. **48**, 5279 (2019)

[94] E. J. Tarsa, E. A. Hachfeld, F. T. Quinlan, J. S. Speck, and M. Eddy, *Growth-related stress and surface morphology in homoepitaxial SrTiO$_3$ films*, Appl. Phys. Lett. **68**, 490 (1995).

[95] A. Prakash, J. Dewey, H. Yun, J. S. Jeong, K. A. Mkhoyan, and B. Jalan, *Hybrid molecular beam epitaxy for the growth of stoichiometric BaSnO$_3$*, J. Vac. Sci. Technol. A. **33**, 060608 (2015).

[96] B. Jalan, P. Moetakef, and S. Stemmer, *Molecular beam epitaxy of SrTiO$_3$ with a growth window*, Appl. Phys. Lett. **95**, 032906 (2009).

[97] K. Ganguly, P. Ambwani, P. Xu, J. S. Jeong, K. A. Mkhoyan, C. Leighton, and B. Jalan, *Structure and transport in high pressure oxygen sputter-deposited BaSnO$_{3-\delta}$*, APL Mater. **3**, 062509 (2015).

[98] A. Prakash, P. Xu, X. W. Wu, G. Haugstad, X. J. Wang, and B. Jalan, *Adsorption-controlled growth and the influence of stoichiometry on electronic transport in hybrid molecular beam epitaxy-grown BaSnO$_3$ films*, J. Mater. Chem. C **5**, 5730 (2017).

[99] S. Suzuki, T. Takeda, A. Ando, T. Oyama, N. Wada, H. Niimi, and H. Takagi, *Effect of Sn^{2+} Ion Substitution on Dielectric Properties of (Ba,Ca)TiO$_3$ Ferroelectric Ceramics*, Jpn. J. Appl. Phys. **49**, 09MC04 (2010).

[100] S. Suzuki, T. Takeda, A. Ando, and H. Takagi, *Ferroelectric phase transition in Sn^{2+} ions doped (Ba,Ca)TiO$_3$ ceramics*, Appl. Phys. Lett. **96**, 132903 (2010).

[101] W. Wu, N. G. Combs, T. E. Mates, and S. Stemmer, *Carbon impurity concentrations in BaSnO₃ films grown by molecular beam epitaxy using a tin oxide source*, Journal of Vacuum Science & Technology A. **38**, 043405 (2020).

[102] N. G. Combs, W. Wu, S. Stemmer, *Stoichiometry control in molecular beam epitaxy of BaSnO₃*, Phys. Rev. Mat. **4**, 014604 (2020).

[103] J. Hu, S. Xu, N. Ni, and Z. Mao, *Transport of topological semimetals*, Annu. Rev. Mater. Res. **49**, 207 (2019).

[104] S. Wang, B. Lin, A. Wang, D. Yu and Z. Liao, *Quantum transport in Dirac and Weyl semimetals: a review*, Adv. Phys. X. **2**, 518 (2017).